Master's Programme in Mechanical Engineering

Multi-scale simulation of low-speed impact loads on Carbon Fibre Reinforced Polymer (CFRP) panels

An application to a thin rigid aerospace panel

Ovidio Colmenero Díaz

Aalto University

MASTER'S THESIS

Aalto University
MASTER'S THESIS 2021

Multi-scale simulation of low-speed impact loads on Carbon Fibre Reinforced Polymer (CFRP) panels

An application to a thin rigid aerospace panel

Ovidio Colmenero Díaz

Thesis submitted in partial fulfillment of the requirements for the degree of Master of Science in Technology.
Otaniemi, 31 March 2021

Supervisor: Professor Jani Romanoff
Advisors: Associate Professor Mikko Kanerva
& M.Sc. Oscar Rodera García

Aalto University
School of Engineering
Master's Programme in Mechanical Engineering

Author
Ovidio Colmenero Díaz

Title
Multi-scale simulation of low-speed impact loads on Carbon Fibre Reinforced Polymer (CFRP) panels

School School of Engineering

Master's programme Mechanical Engineering

Major Solid Mechanics **Code** ENG25

Supervisor Professor Jani Romanoff

Advisors Associate Professor Mikko Kanerva & M.Sc. Oscar Rodera García

Level Master's thesis **Date** 31 March 2021 **Pages** 87 **Language** English

Abstract

In the field of advanced composites for high-technology applications, such as aerospace, the multi-scale modelling approach is of great importance. The novelty of this technique relies on the fact that it allows to study the macroscopic behaviour of the composite considering its microscopic characteristics. This is achieved by considering the composite as an interconnection of different length scales. The separation of length scales results into computational time-savings, as the macro-model does not need to include detail of the microstructure. Such method is used in the current thesis to model a CFRP panel and numerically simulate low-speed impact loads acting upon it. The multi-scale modelling tool used is the Multiscale Designer (MD) by Altair. This software computes homogenized material models using as inputs the material properties of the micro-constituents (fibre, matrix and interphase). The objective of the thesis is to understand the multiscale method that has been implemented in the MD software. Computational models are never completely accurate and they mismatch with experiments. The key is to understand why they do not give the same results, the reasons behind and how big or severe the deviations are. To do so, in this work different MD material models are generated for 1 ply and for the complete laminate. These are employed in two different FE macro-simulations corresponding to an indentation test and an impact test. Additionally, a manual material model based on laminate experimental constants is also used. The effects of the different material models on the indentation and impact FE-simulations are studied. The FE-results are compared to digital image correlation (DIC) data measured at the Laboratory of Materials Science of Tampere University, Finland. Eventually, the effect of the interphase on the macro-scale behaviour is evaluated. Finally, the results obtained through multi-scale are assessed to define the feasibility and applicability of the multi-scale approach in the composites modelling.

Keywords Multi-scale modelling, Simulation, FEA, Composites, CFRP, Impact loads, Aerospace

urn https://aaltodoc.aalto.fi/handle/123456789/18

Acknowledgement

First of all, I would like thank my advisor Associate Professor Mikko Kanerva for giving me the opportunity to perform this thesis in the field that I was interested in the most. He kindly accepted to offer me this interesting topic despite of not being his student (neither student from Tampere University), as well as he gave me his trust from the very beginning. Thanks to Mikko this collaboration with Aalto University was arranged and the realization of this project came true. Thank you very much to my supervisor Professor Jani Romanoff for accepting to supervise this thesis and for his guidance during the whole process. Also, without Jani's approval it would not have been possible the realization of this project at Tampere University by an Aalto University student. Special thank you my advisors Associate Prof. Mikko Kanerva and M.Sc. Oscar Rodera García for their help, support and patience throughout this entire project. Thank you Oscar for your kindness in having tens of "Teams Meetings", always willing to help me and support my learning. Thanks for trying to follow my work as close and up-to-date as possible, even when your own schedule was too full.

Secondly, I would like to thank Unna for her entire and endless emotional support throughout this difficult year, always offering her help despite of not being technically able to do so. You have encouraged me to keep fighthing even in the darkest and most challenging moments, when things simply seemed impossible to be sorted out.

Thirdly, I am very thankful to Arttu and Sirpa for having always welcomed me in their home, both during my first months in Finland, but also during the exceptional Covid-19 pandemic months. Thanks to them, among other things, I managed to work on this thesis during the difficult Spring 2020 and take advantage of the 'lockdown' months.

More than anything in this world, I thank my parents Julia and Francisco, who have strongly supported me in all my life decisions, included when I decided to move to Finland and pursue my Master's Degree in here. Despite of being separated by more than 3000 km and have spent a lot of months without seeing each other during the pandemic, they have walked with me along this journey in achieving my Master of Science in Engineering. Without them it would not have been possible to get up to this point.

Last but not least, I would not like to forget about my grandparents, who have always encouraged me to study hard and reach as highest education level as possible since I was a child. Unfortunately they have not managed to see how far I have reached in my studies. However, I am sure that they would be very proud and happy of seeing their grandson reaching the level of M.Sc. in Engineering, which is by far one of the greatest accomplishments that humble people like them could have ever imagined.

To all of them, thank you.

Helsinki, 31.3.2021
Ovidio Colmenero Díaz

Contents

Nomenclature

Symbols & Variables

E	$[Pa]$	Young's Modulus
E_0	$[Pa]$	Undamage Young's Modulus
G	$[Pa]$	Shear Modulus
ν	$[-]$	Poisson's Ratio
S	$[-]$	Maximun Allowable Stress
N	$[-]$	Number of Loading Cycles
D	$[-]$	Damage Accumulation
K_{IC}	$[Pa\sqrt{m}]$	Fracture Toughness
G_{IC}	$[J/m^2]$	Strain Energy Release Rate
G_C	$[J/m^2]$	Critical Energy Release Rate
a	$[m]$	Crack Length
U	$[J]$	Elastic Energy
P	$[N]$	Constant Load
u	$[m]$	Displacement
V_f	$[-]$	Fibre Volume Fraction
V_v	$[\%]$	Voids Content
$\mathbf{F_M}$	$[-]$	Macroscopic Deformation Gradient Tensor
${}^3\mathbf{G_M}$	$[-]$	Gradient of the Macroscopic Deformation Gradient Tensor
$\mathbf{P_M}$	$[-]$	First Piola-Kirchhoff Stress Tensor
${}^3\mathbf{Q_M}$	$[-]$	Work Conjugate of the ${}^3\mathbf{G_M}$

w	$[-]$	Kink Band's width
Φ	$[m]$	Inclination Angle of Kink Band
β	$[-]$	Kink Band Boundary Orientation
K_n	$[N/m]$	Contact Stiffness

Abbreviations

CFRP	Carbon Fibre Reinforced Polymer
XWB	Extra Wide Body
FE / FEM	Finite Element / Finite Element Method
FEA	Finite Element Analysis
GFRP	Glass Fibre Reinforced Polymer
FML	Fibre Metal Laminate
MB	Microbond Test
AFRP	Aramid Fibre Reinforced Polymer
TAU	Tampere University
UB	University at Buffalo
ACM	Advanced Composites, Advanced Composite Material
Pre-preg	Pre-impregnated fabric
UD	Unidirectional Laminate
RTM	Resin Transfer Moulding
ILSS	Interlaminar Shear Strength
RoM	Rule of Mixtures
SEM	Scanning Electron Microscope
FRP	Fibre Reinforced Polymer
H-T	Halpin-Tsai
CLT	Classical Lamination Theory
FSDT	First-order Shear Deformation Theory
TSDT	Third-order Shear Deformation Theory
ESL	Equivalent Single Layer Theories
MM	Multi-scale Modelling
RVE	Representative Volume Element
BC	Boundary Conditions
BVP	Boundary Value Problem
GUI	Graphical User Interface
MD	Multiscale Designer™
PDF	Probability Distribution Function
ROM	Reduced Order Model
ERR	Energy Released Rate
CZM	Cohesive Zone Model
DIC	Digital Image Correlation
SPC	Single Point Constraint

1. Introduction

Composite materials are widely used for lightweight structural applications in many fields of engineering. Carbon-fibre reinforced polymers (CFRP) have become one of the main materials in modern aircraft structures, as they comprise around 50% of Boeing's 787 Dreamliner and 52% of Airbus A350-XWB. Airframe structures are likely to suffer impact-type loads during their operational lifetime, which makes it crucial for engineers to ensure that the structural integrity of the CFRP structures will not be endangered. For more than 40 years advanced composites have been thoroughly studied and a large knowledge in the subject is already available. In the early times the research was based on experimental and destructive testing, which had high costs. Computer-based numerical simulations allowed to speed up the analysis and to reduce the costs, as it was not anymore necessary to manufacture the material samples and to test all of them. Instead, the material could be virtually tested by solving a mathematical model. As the complexity of the models increased in order to improve the accuracy of the results, computational resources started to limit work. This involves limitations when modelling the microstructure of the composite, as trying to solve a Finite Element (FE) model accounting for all the fiber filaments and/or the fibre-matrix interface effect is unfeasible. Multi-scale modelling is a technique that allows to study the macroscopic behaviour of a composite considering its microscopic behaviour. The strategy followed is to separate the composite in different length scales, which are studied individually. However, all scales are interconnected by passing the information from the previous scale to the next one. Thus, high-fidelity numerical simulations of the mechanical behavior of composite are achieved.

The multi-scale modelling approach has already been used for more than

a decade to study composite structures [1] and recent publications still rely on it [2]. Previous studies in impact loads on laminated composite aircraft structures have been performed to predict the damage evolution. The damage modelling approach has been employed at high-velocity impact on CFRP and glass fibre reinforced polymer (GFRP) composite plates, [3] and [4]. Low-velocity impact damage in fibre metal laminates (FMLs) has been studied in [5]. Interface failures such as delamination and debonding have been investigated using numerical fracture analysis methods in order to understand the crack nucleation and propagation on bonded joints [6]. To better understand composites adhesion several studies have focused on the fibre-matrix interface. The Microbond Test (MB) has been employed to characterize the adhesion for single fiber-matrix interface, [7], [8] and [9]. Alike, FE models have been validated against experimental results on GFRP and aramid fibre reinforced plastic (AFRP) composites. Moreover, MB methods to observe the aging behaviour of GFRP in terms of the fibre reinforcements and the interphase are presented in [10]. The quantification of the effect of fibre aging on stiffness degradation of GFRP composites has been done following a multi-scale modelling approach in [11].

This thesis aims to simulate a low-speed impact load on thin rigid panel made of a CFRP material widely used in aerospace structures by using a multiscale method for the modelling. The simulation is based on the Finite Element Method (FEM) and the focus is a commercial modelling environment by Altair (Troy, Michigan, United States), called Multiscale Designer. The ultimate goal of this work is to understand the multiscale method that has been implemented in Altair software, by understanding the reasons for the results deviations with respect to experimental data, and to evaluate how severe these deviations are. Experiments on this study case had been previously performed at the Laboratory of Materials Science of Tampere University (TAU), in Finland. In addition, this work is related to experimental and modelling activities of TAU and University at Buffalo (UB), in the USA.

The current report starts by introducing to the subject, explaining the current state of the art and reasoning the relevance of the topic. Secondly, the theoretical background in advanced composites and modelling is provided, as well as an overview of the software used. The third part contains all information concerning the actual modelling and computations

performed. Then, in the fourth part, the results of the simulations are presented and analysed, especially focusing on the differences between models and deviations from experiments. Also the discussion is given based on the results, comparison with experimental data and findings. Finally, the conclusions of the work are presented.

2. Theoretical Background

2.1 Advanced composites and their micro-defects

A composite material can be defined as a combination of two or more constituent materials, which are physically and chemically different, and result in better properties than those of the individual components used alone [12]. Advanced composite materials (ACMs) are characterized by a high specific strength and stiffness compared to other composite materials. They present high strength fibers, which cover a large volume fraction. In combination with automatic manufacturing processes, ACMs make it possible to fabricate composite structures with high levels of weight and cost efficiency. The replacement of metal alloys by composite materials, in general, reduces the structure's mass by 20–30% [13]. Advanced composite materials were primarily developed for aerospace to enhance the performance of commercial and military aircraft [14]. As stated in recent technology reviews [15], high performance as well as reducing weight and cost are the key factors for material selection in aerospace industries, which motivate the usage of advanced composites.

Fibre-reinforced plastics (FRP), also known as Polymer Matrix Composites (PMC), are formed of strong fibers and plastic matrix material [16]. The load carrying component typically consists of thin fibres that can be made of glass, carbon or aramid. Depending on the fibre type, FRP can be classified into CFRP, GFRP or AFRP. In this work, the focus is on CFRP consisting of carbon fibres and epoxy matrix.

Continuous-fibre composites are laminated materials, which are manufactured as an assembly of thin layers joined together to form a laminate,

as shown in Fig. 2.1. Each layer is referred to as a lamina or ply. By orienting the reinforcement direction of each ply, the properties and behavior of the resulting laminate can be controlled [17].

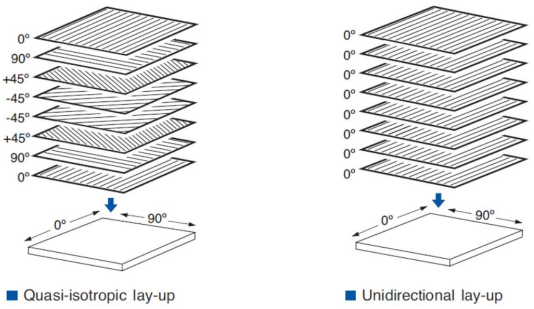

Figure 2.1. Unidirecciontal and quasi-isotropic laminate lay-ups. [Source: HexPly®]

Unidirectional (UD) laminates (0°) are extremely strong and stiff in the $0°$ direction, Fig. 2.1. However, they are weak in the perpendicular direction (90°) since the load must be withstood by the polymeric matrix and interfaces. The longitudinal tensile loads are carried by the fibers, while the matrix distributes the loads between the fibers, and stabilizes and prevents the fibers from buckling in compression. The matrix is also the primary load carrier for interlaminar shear and transverse tensile load. As fibre orientation affects the mechanical properties, the orientation of the layers should balance the load-carrying capability in different directions [18]. A quasi-isotropic laminate (Fig. 2.1) can be formed by balancing the orientations of the plies such that the extensional stiffness of the laminate is constant in all in-plane directions, i.e. equal loads are carried in all four directions $[0/90/45/\text{-}45]_s$.

A preimpregnated (pre-preg) fabric is a pre-made lamina, in which the fibres are impregnated with the resin that is partially cured. To produce the laminated composite panel, several pre-pregs are placed on top of each other in a mould. The mould is placed in an oven or autoclave (a heated pressured vessel) at an elevated temperature, which causes the partially cured resin to transform into a form with a lower viscosity. When the temperature is further raised, the resin solidifies [19]. An autoclave offers the advantage that high pressures can be reached resulting in better compaction between pre-pregs, higher fibre volume percentages, as well as less voids and porosity. Autoclave curing is the most widely used manufacturing process for high-performance composites in aerospace industry [18].

According to recent studies [20], several issues affect the manufacturing quality of complex-shaped laminates using pre-pregs. The most critical issues are ply/fibre wrinkling and misalignment, thickness uniformity, resin distribution and void content. These contribute to reduce the mechanical properties and life span of the composite. The defects occuring have been found to be substantially affected by various factors, such as mould selection, material characteristics and bagging configuration. The correlation between the processing parameters and the related defects has been thoroughly investigated in [20].

Another manufacturing process used for aerospace applications is Resin Transfer Moulding (RTM) in hydraulic closed molds, [21]. The mould has a cavity that is the shape of the part to be manufactured. The fibre preform is shaped by draping the fabric plies on the surface of the mould. Then, the mould is closed and clamped. The resin is injected into the mold cavity under positive pressure, and heated to a temperature where the vicosity is sufficiently low that it will fill the preform. The resin is left to cure and after the part is sufficiently hardened, the mold is opened and the part demolded. The part's manufacturing quality using RTM varies due to the effects of inherent variations in the materials and process paramaters, [21]. The main issues influencing in RTM manufacturing are: racetracking channels, deformation of fiber structure during draping, macrovoid and microvoid formation.

Manufacturing defects introduced in FRPs result in a loss in mechanical properties. Voids are particularly detrimental to the compressive strength and matrix-dominated properties, such as interlaminar shear strength (ILSS). Thus, the effect of voids should be determined. In cured pre-preg laminates there are various sources of porosity, [22]. The most common form of porosity is located between plies. These voids can be originated due to absorbed or dissolved water and gases in the pre-preg, the entrapment of air between plies during the autoclave process, or residual gases produced by the curing reaction. Porosity within the ply is not that common. However, it can be caused by an incomplete wetting of the fibre bundles. In the RTM process voids are mainly formed due to the mechanical entrapment of air during resin flow. When resin impregnates the dry preform there are two main directions at the flow front that the resin can travel, between the fibre bundles and within the fibre bundles. An irregular flow front can

lead to the trapping of air pockets in the preform. Another form of voids in RTM is gas created by reactions occuring within the resin. Besides, voids can also be introduced into the laminate in the form of bubbles, when the resin is insufficiently degassed before the injection. The formation of voids can affect the mechanical properties of the material in different ways. For that, their analysis requires also to consider morphology aspects, such as size, shape and concentration [22]. Fig. 2.2 shows a comparison between the effect of porosity on ILSS in prepeg and RTM laminates, which belongs to the experimental results presented in conference paper [22]. Each point on Fig. 2.2 represents one single test. In the prepreg case, when the voids content (V_v) increases by 1%, the ILSS reduction is 12%. The scattered ILSS results for RTM laminates is due to the difference in voids shapes and sizes. The voids of prepreg laminates had higher aspect ratios, which would justify the bigger strength reduction compared to RTM laminates. However, the results of RTM laminates with only asymmetric voids appear to be similar to the prepeg results, although with lower drop in ILSS. A comparison between the spherical and asymmetric porosity effects can be seen in the region between 0% and 2% of V_v. Up to a 2% V_v the effect of bubble porosity on ILSS is low. The scatter in results in the region between 2% to 5% of V_v is due to the size and content of the voids.

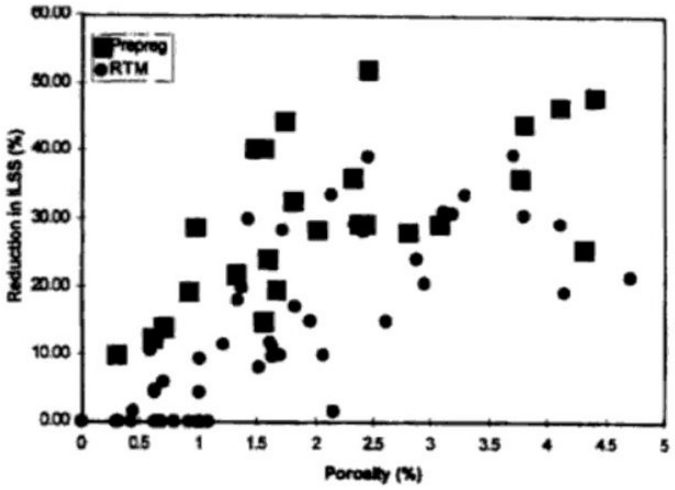

Figure 2.2. Comparison between the porosity effect on prepreg and RTM laminates. The graph shows the resduction in ILSS with respect to void content (V_v). [Source: [22]]

A new method to produce CFRP components has been recently developed by the company Corebon AB. The innovative method allows denser fibre packing and less residual internal stresses in the final CFRP laminate. This is achieved by induction heating of the CFRP laminate with an ex-

ternal inductor during production. When packing the fibres very densely, it is difficult to get the resin in the right place. This problem is solved by heating the laminate from the inside with a frequency inverter, as carbon fibre is a semiconductor. In addition, the method reduces the high processing and production costs of CFRP components.

2.1.1 Micromechanics: Fibre-matrix level

The fibre-matrix level is commonly the lowest level considered when applying a multi-scale approach to composite panels studies. Due to the different properties of the fibre and matrix as well as their interaction, a third phase is usually defined in composite materials. The so-called interface is a region or layer found in-between the fibre and matrix, whose properties result from the fibre-matrix interaction. The fibre-matrix interface plays an important role in the mechanical and physical properties of the composite. Due to the large differences between the elastic properties of the matrix and the fibres the interface acts as transfer medium, which means that the stresses acting on the matrix are transmitted to the fibre across the interface. For the fibre to perform properly in terms of high strength and stiffness, also a strong bonding to the matrix is needed. Coupling chemical agents are often added to improve the bonding between fibers and matrix material and to increase toughness. The interface is a dominant factor in the fracture toughness of composites. "Weak interfaces cause relatively low strength and stiffness but high resistance to fracture, whereas strong interfaces have high strength and stiffness but are very brittle. This effect is related to the ease of debonding and fibre pull-out from the matrix during crack propagation" [23].

Elastic properties are needed in the evaluation of the fibre-matrix behaviour, as well as the volume fractions of each constituent. This evaluation is usually covered by micromechanical models. The initial assumption of micromechanics is the linear elastic behaviour of the constituents. Moreover, the fibers are assumed to be planar isotropic, the matrix is assumed to be isotropic and the composite to be non-porous. In the real world, these assumptions do not hold since carbon fibres are orthotropic, not even axisymmetric and porosity is present within the composite. In reality, carbon fibres are transverse isotropic since the Young's modulus is a function of the basal planes orientation, as shown by X-ray diffraction in a scientific article [24]. A carbon fibre consists of graphite crystallites with their basal

planes having a preferred orientation of within 10° to the fibre axis. The elastic constant parallel to the graphite planes is two orders of magnitude higher than the Young's modulus in the C axis direction (perpendicular axis to the graphite lattice planes). This is due to the anisotropic layer lattice of the graphite crystal. It is to remark that the study performed in the work [24] focuses on an specific type of carbon fibre, tows of polyacrylonitrile (PAN) fibres of varying Young's Modulus and processed by simple RAE manufacturing process. RAE is a process for producing carbon fibres from a PAN precursor. A method to increase the strength and Young's modulus is proposed by the paper [24]. The fibre is stretched by 4 to 8 times at an elevated temperature to align and to order the molecule chains along the fibre axis. By doing so, the interchain adhesion is highly increased with an important rise in the strength (one order of magnitude) and Young's modulus in the direction of the fibre axis. This proves the anisotropy and the elastic constants dependency on the graphite crystal planes orientation. Moreover, the mean strength of carbon fibres is limited by defects as discovered in research [24]. Some of these defects are due to inclusions or manufacturing defects in the parent fibre carried over into the carbon fibre. After finding several visible flaws in the parent fibre, it is concluded that an improvement in fibre cleanliness increases the carbon fibre strength.

The effective elastic properties of a composite can be estimated based on the individual elastic values of the constituents (fibre, matrix and interphase). The effective elastic properties defining a composite are the longitudinal, transversal and orthogonal Young´s modulus E_1, E_2 and E_3, the longitudinal, transversal and out-of-plane shear modulus G_{12}, G_{23} and G_{31}, the Poisson´s ratios ν_{12}, ν_{23} and ν_{31} and the fibre volume fraction V_f. Note that direction 1 corresponds to the fiber firection, direction 2 to the transversal direction and direction 3 to the orthogonal direction to the plane 1-2, as illustrated in Fig. 2.3.

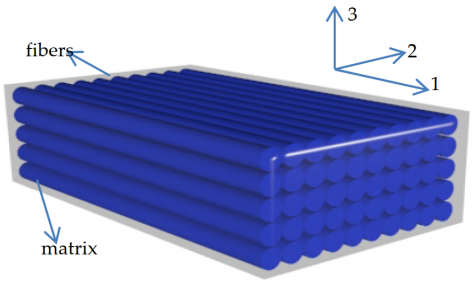

Figure 2.3. Fibres and matrix forming a UD composite. [Source: [25]]

Various analytical micromechanical models have been proposed to evaluate the elastic properties of UD long-fibre composites and the most known ones have been reviewed in [25]. The well-known Rule of Mixture (RoM) consists of the Voigt and Reuss models, as presented by [25] and [26]. The axial and transverse Young´s modulus can be predicted using a simple slab model, in which the fibre and matrix are represented by parallel slabs with thicknesses in proportion to their volume fractions, see Fig. 2.4. In the Voigt model, both micro-constituents are assumed to have the same strain when the slabs are subjected to a load in the fibre direction. Whereas the Reuss model applies a perpendicular load to the fibres by assuming the same stress in the slabs. The Voigt model, known as the RoM, can be used to predict the longitudinal stiffness of a composite. This corresponds to the upper bound of the composite stiffnes, as shown in Fig. 2.5. The Reuss model, known as the Inverse Rule of Mixtures, gives only a prediction for the transverse stiffness. It is a series model and does not account for the regions acting in parallel, neither for the distortions around circular fibres, where stress concentrations with a factor of 3 appear in circular holes loaded in uniaxial direction [26]. Therefore, the Reuss model is a simplification and does not provide with a lower bound for transverse stiffness.

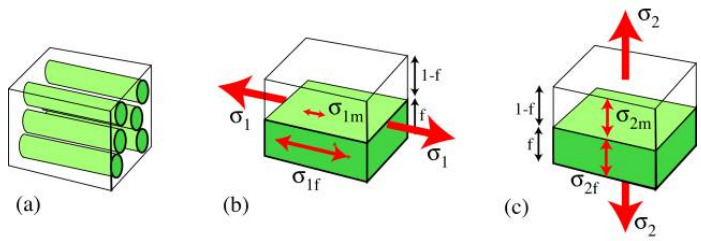

Figure 2.4. RoM slab models. (a) Fibre and matrix, (b) Voigt model (Axial loading) and (c) Reuss model (Transverse loading). [Source: University of Cambridge, [26]]

Semi-empirical models have emerged to correct RoM models by introducing correcting factors. The Halpin-Tsai (H-T) model gives a better prediction for the transverse stiffness, see Fig. 2.5. It tends to correct the transversal Young´s modulus and longitudinal shear modulus. Unlike the Reuss model, the Halpin-Tsai does provide with a lower bound for the transverse stiffness. Halpin-Tsai formulations is presented in the Appendix A of article [11], as well as in the conference paper [27]. The H-T equations were developed in the late sixties with the aim of providing a simple but effective way of calculating the elastic properties of a fibre reinforced lamina, since previous developments had led to complicated equations difficult to use. Their success is based both on their simplicity

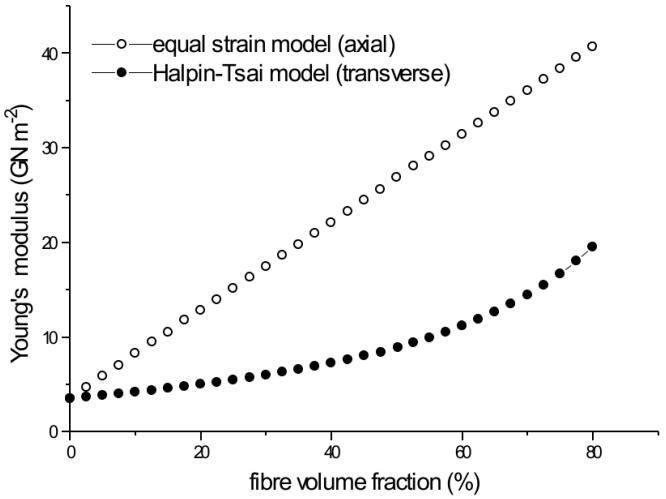

Figure 2.5. Young´s modulus vs fibre volume fraction. The upper bound for the axial stiffness is provided by the Voigt model and the lower bound for the transverse stiffness is provided by Halpin-Tsai. [Source: Aalto University, [26]]

and on the generalization of previous micromechanics results heavy to use, as well as the relatively accurate estimations that they provide. Neither the RoM nor the H-T formulations consider possible manufacturing defects (e.g. voids) within the composite. However, the H-T accounts for the interfaces and interphases around the fibres, which affect the transverse load transfer through the matrix. This is done by means of two parameters η and ξ, where ξ is an adjustable parameter. The second Halpin-Tsai equation presented in paper [28] defines η as a function of the fibre and matrix Young's Modulus and the parameter ξ. According to [28], ξ is a geometry factor that may be expressed in terms of combinations of engineering elastic constants and differences in Poisson´s ratios. The only assumption made when assigning values for this geometrical factor is that the engineering stiffness expressions of the composite ply are insensitive to the difference in Poisson ratios of the composite constituents. ξ is also known as the reinforcement factor and it varies with the geometry of the reinforcement, its distribution and the volume fraction. The originally proposed value by Halpin-Tsai [28] is $\xi = 2$. However, more recent studies [27] have concluded that a value of $\xi = 1.5$ is a better estimation for the usual volume fractions found in practice for UD plies of FRP.

2.1.2 Micromechanics: Fibre-bundle level

Fibre filaments are not usually placed individually inside the matrix, but they are grouped into bundles. Each of these bundles contain several hundreds of individual fibre filaments, reaching up to thousands in some

cases (see Fig. 2.6). The fibre grouping in bundles is particularly useful for the manufacturing of woven composites, which offer advantages for certain applications. These follow textile-like geometries by weaving the fibre bundles into a cloth before the incorporation of the resin (matrix). Scanning electron microscope (SEM) images clearly show the fibre bundles of a woven laminate before infiltration of the resin, see Fig. 2.7 (a). Fig. 2.7 (b) shows a cross-sectional view of the woven laminate, where parallel fibre bundles can be seen in 0° and 90° directions.

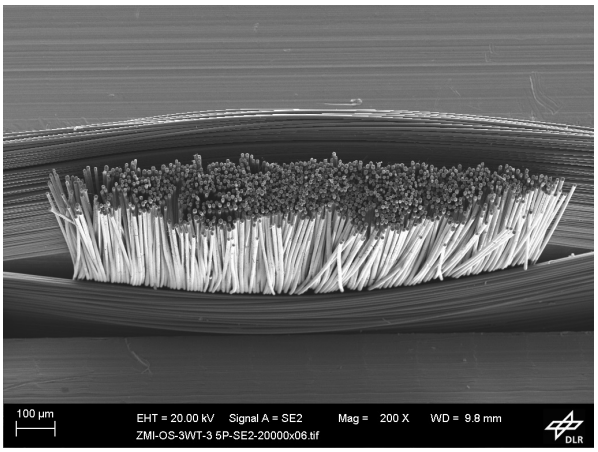

Figure 2.6. Carbon fiber filaments inside the fiber bundle before infiltration. [Source: DLR, [29]]

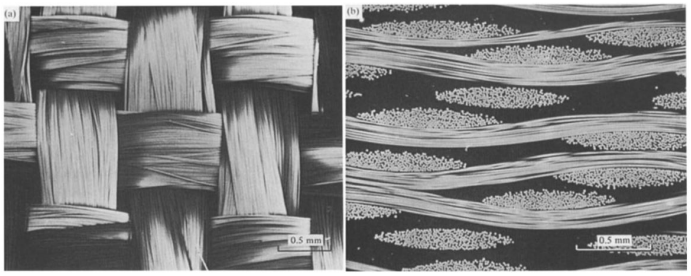

Figure 2.7. SEM images of woven rovings before infiltration. (a) Top view and (b) cross-sectional view. [Source: [23]]

The fibre-bundle level in multi-scale modelling brings some challenges. One reason is the amount of filaments to be included in a FE model, which would result in a high computational cost, as explained in the thesis [29]. Modelling a tow structure inside a ply using a few elements is difficult, sometimes even unfeasible. Computationally unreasonable models are easy to get when trying to model fibre bundles, as proved in the thesis [29]. However, fibre-bundle models have been developed and they are used as theoretical approaches to investigate the fracture and breakdown of advanced composites, [30]. The damage development of a plain woven fabric GFRP composite subjected to on-axis uniaxial tensile load is predicted in a scientific article [31]. The microscopic damage propagation is simulated by

FEA using an anisotropic damage model based on damage mechanics. A 3D modelling of the fibre-bundle level is necessary since the plane stress and plane strain conditions are not fulfilled when dealing with woven composites. Fig. 2.8 shows the fibre-bundle level model used. Typical classical failure criteria such as Hoffman's failure criterion cannot indicate the type of damage mode. Nevertheless, FEA allows to describe the failure mode by looking at the maximun stress-to-strength ratio. As shown in a scientific article [31], modelling and simulation of the fibre-bundle level is often used to evaluate the damage mechanism in composites.

Other studies performed on the fibre-bundle focus on investigating the adhesion properties on aramid fibres after applying surface treatment methods, [32]. The effect of surface treatment on aramid fibres within rubber matrix composites is studied in the article [32] using a modified fibre bundle pull-out test. The surface treatment uses microwave energy to induce nanoscale deposits onto the aramid fibre surface. After the carburizing process, the fibre bundles are covered with carbon deposits. After fibre bundle pull-out test, the fibre bundles are extracted from the rubber matrix and the aramid fibres are imaged through a stereomicroscope. The results of the bundle pull-out test conclude that the microwave assisted surface treatment does increase the adhesion. The pull-out force is increased by 102-124% (compared to the untreated fibres) depending on the microwave irradation time of the fibres. The fibre bundle pull-out test indicates a 102–259% increase in adhesion strength gained using this method. The pull-out tests also show that carbon nano-deposits appear strongly attached to the fibre surface, which guarantees the handling of the fibres without compromising the improved properties.

Studies on the influence of the fibre distribution when determining the transverse flow permeability have also been performed at the fibre-bundle level, [33]. The reason is that during the production process of continuous fibre reinforced composites, the fibre bundles are arranged in a certain way. This can be either forming a textile, or a layered structure where all fibre bundles are located parallel to each other. Depending on the case, the study on the permeability of the resin is different. The flow into individual fibre bundles is characterized by the microscopic permeability, whereas for the flow through fibre bundles the macroscopic permeability is of interest. The UD fibre architecture of the fibre bundles is examined in a scientific

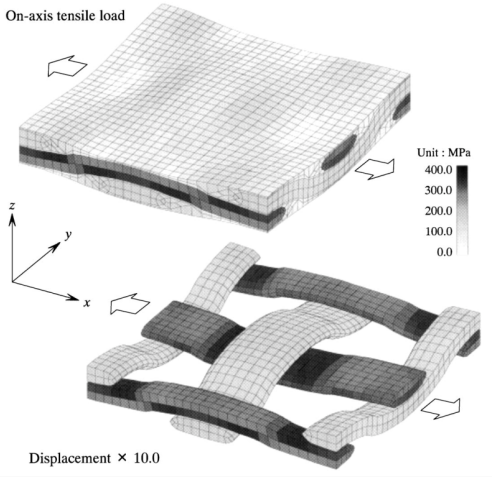

Figure 2.8. Fibre-bundle level model of a woven GFRP composite. [Source: [31]]

article [33]. Microscope imaging of glass fibres show that the bundles have elliptical shapes and they are characterized by their semi-axis. In reality the fibre bundles cross over with each other and the resin flow channels do not remain constant, as it is usually assumed in models. Hence, the fibre distribution inside the fibre bundles needs to be determined. For that the evaluation of regions with 25 and 100 fibres in a bundle containing about 400 filaments is performed in the article [33]. The results show that 100 fibres is enough to represent the fibre distribution within a fibre bundle. Additional studies on the fibre distribution inside the fibre bundle have been performed since the distribution appears to be non-uniform with a systematic variation, [34]. Modelling the fibre-bundle level in UD pre-preg laminates is usually skipped since the fibres do not follow any weaving.

2.1.3 Macromechanics: Ply and textile level

A lamina or ply is the typical sheet of the reinforced material that represents a building block of fibres embedded in the resin matrix. The stacking sequence of these individual structures forms the composition of a laminate. The set of plies that are not connected are named laminae, or laminate [35]. This connection refers to the joint between plies. In other words, the laminate is the collection of laminae stacked to achieve the desired stiffness and thickness [35]. The sequence of the plies orientations in a laminate is termed lamination scheme or lay-up. A commonly used scheme is $[0/45/-45/90]_S$, which corresponds to a quasi-isotropic laminate.

Macromechanical models can be used to model composites at the ply level. They allow to evaluate both the behaviour of a single lamina and

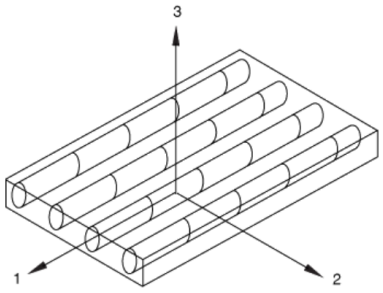

Figure 2.9. Orthotropic UD lamina, its principal directions (1, 2 and 3) and main planes (12, 13 and 23). [Source: Abaqus-MIT docs]

a laminate. The behavior of a single laminae with reinforced fibres can be defined as orthotropic. The mechanical behaviour of a linear elastic orthotropic layer is completely determined by its elastic values in the global coordinate system, see Fig. 2.9. There exist a total of nine elastic values: 3 elastic modulus (E_1, E_2, E_3), 3 Poisson's ratios (ν_1 , ν_2 and ν_3) and 3 shear modulus (G_{12}, G_{13} and G_{23}), [16]. If the behaviour and design (orientation) of the layers is known, the Classical Lamination Theory (CLT) can be used as a mechanical model for the laminate, [16]. As shown in Fig. 2.10, the CLT models the laminate as a composition of several single layers, where each layer corresponds to a lamina or ply. CLT is based on several assumptions, [35]:

- The plies forming the laminate are macroscopically homogeneous.
- The plies are perfectly bonded together.
- Each ply behaves linearly elastically and has three planes of symmetry (orthotropic).
- Each ply is of uniform thickness.
- The laminate is in plane stress.
- The laminate is in accordance with the classical beam theory (normal planes with respect to the geometric mid-plane remain planes after deformation).
- The strains and displacements are small.

CLT describes the mechanical behaviour of a laminate based on its stiffness matrices: Membrane stiffness (A-matrix), Bending stiffness (D-matrix) and Membrane-bending-coupling stiffness (B-matrix). CLT derives that the stress-resultants of a laminated plate (normal forces and bending moments) are coupled by the extension-bending stiffness matrix (B-matrix). This allows to classify laminates on the properties of the stiffness matrices into symmetrical ([B]=0) and asymmetric ([B^1]=0).

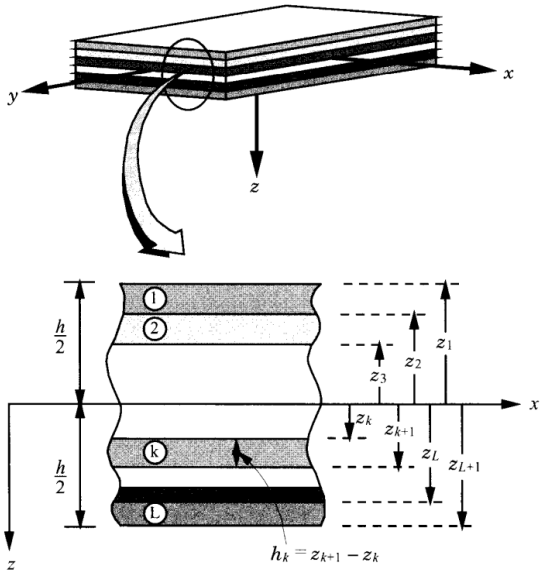

Figure 2.10. Representation of a laminate composite panel by means of CLT. The laminate is modelled as a series of layers with different thicknesses and properties stacked upon each other, having as reference plane the so-called geometric mid-plane. [Source: [35]]

CTL is the simplest possible approach to model composite laminates and it describes accurately the behaviour of a continuous laminate as long as the assumptions mentioned above are valid. The theory describes the behaviour of relatively thick laminates well. Along with CTL, first and third order shear deformation theories (FSDT and TSDT) are the most common structural theories used to assess the response of laminates, [35]. These are the so-called Equivalent Single Layer Theories (ESL) and they are defined as "Those in which a heterogeneous laminated plate is treated as a statistically equivalent single layer having a complex constitutive behaviour" by [35]. Moreover, there exist higher order equivalent single layer theories that use higher order polynomials in the expansion of the displacement field through the laminate thickness. These introduce additional unknowns with difficult physical meaning. ESL theories are derived from 3D elasticity theory by making suitable assumptions concerning the kinematics of deformation and/or the stress state. Such assumptions allow to reduce a 3D problem to a 2D problem. According to [35], ESL theories are developed by assuming the form of the displacement field or stress field as a linear combination of unknown functions and the thickness coordinate. Nowadays, ESL are available in commercial FE codes, which makes them computationally inexpensive in terms of the number of degrees of freedom used, although they have certain problems [36]. FE models of the CLT require that the transverse displacement field is continuous, which means that the function and its derivatives must be continuous through the lam-

inate thickness. This makes it difficult to develop conforming elements and to use them with common FE. In the FSDT, the shear rotations of the transverse normals are independent of the transverse displacement. Thus, it does not present the same problem as the CLT. In contrast, it can experience a false transverse shear stiffness as the laminate becomes thinner, also known a locking. This effect can be reduced using higher order elements.

2.1.4 Failure modes at different scales

Failure in composites is not due to one single event, but to multiple damages occuring mostly in a sequential order, [37]. In general, these damages occur at the micro-level and they are named as local damages. Thus, the final matrix failure generally happens after a series of local damages. This stepwise failure process is known as damage growth. There exist different types of damage mechanisms in composites, as shown in Fig. 2.11. These can be classified in three main categories depending on the scale at which they take place: micro-level, macro-level and coupled micro-macro-level, [37].

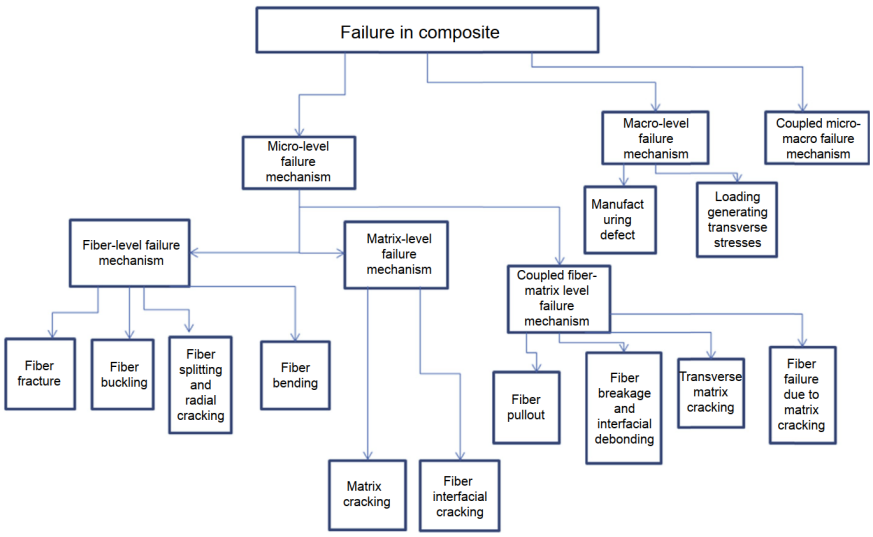

Figure 2.11. Classification of failure mechanisms at different composite levels. [Source: [37]]

In the current text three important terms are often used and their meanings need to be distinguished. Damage refers to the actual loss of material due to mechanical action. Failure is the term used define the lack of functioning of a material compared to its intended requirements. To understand the failure mechanism, first the responsible cause of failure needs to be understood. Fracture is the physical separation of a material into

two or more pieces, under the action of an applied or induced stress. As a summary, it could be said that damage leads to failure and failure leads to the material fracture. It is to remark that the current subsection 2.1.4 is based on the chapter 3 of book [37].

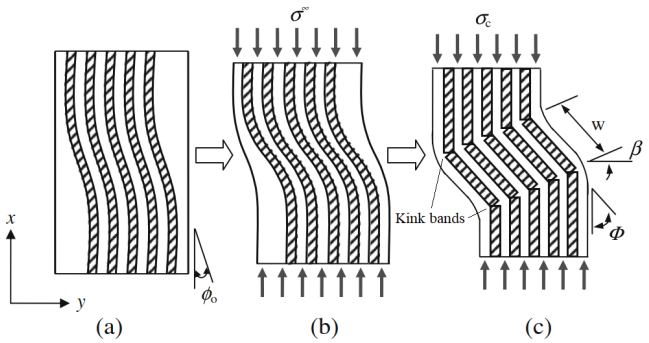

Figure 2.12. Schematic representation of fibre buckling mechanism. (a) 0° fibres with initial misalignment Φ_0. (b) Composite starts to buckle under compression loading. (c) Fibre buckle and formation of kink bands in the UD laminate. [Source: [38]]

Within the micro-level three subcategories can be distinguished: fibre-level, matrix-level and coupled fibre-matrix (also known as interphase). The most catastrophic failures are usually originated at the micro-level. These are usually caused by the fibre failure since it is the main load-carrying constituent in the composite. The major fibre damages are classified in a book [37] as: fibre fracture, fibre buckling, fibre bending, fibre splitting and radial cracking. Fibre fracture occurs when the stress or strain acting along the fibre axis direction exceeds the fibre's axial ultimate strength. Consequently, the fibre breaks down into two or more smaller fibre segments. "This is the most destructive rupture that can occur in a fibre-reinforced composite" [37]. Fibre buckling occurs when a layer of fibre tends to buckle under the action of a compresive load. Buckling, also known as kinking, is mainly due to compressive stress applied in the fibre axial direction, Fig. 2.12 (b). Fibre buckling occurs in the region of the composite where there are fibre misalignments or local defects, Fig. 2.12 (a). These are known as kink bands and they appear inclined at a certain angle Φ with respect to the fibre direction, Fig. 2.12 (c). The kink band geomtry can be defined by some parameters as shown in Fig. 2.12 (c), where w is the kink band's width, β the kink band boundary orientation and Φ is the inclination angle. The inclination angle Φ can be expressed in terms of the initial misalignment angle Φ_0 and β as follows: $\Phi = \Phi_0 + \beta$. Buckling is particularly dangerous since it works as a potential activator of other damage mechanisms (e.g. delamination, Fig. 2.14), thus leading to catastrophic failure. In bending, the fibres on the outer layers of the

laminate are subjected to tensile stresses while the inner layers experience compressive stresses, i.e. the bending radius is smaller in the inner layers of the laminate. The bending radius can be interpreted as a measured of the layers' curvature. The difference in bending radius between the outer and innter layers originate a strain gradient. Thus, the fibres in the outer layer will reach their ultimate strength earlier than those in the inner layer, and they will start cracking. On the other hand, fibre splitting and radial cracking occur due to exceeding hoop stresses, also known as circumferential stresses.

At the matrix-level, two main damage mechanisms are found: matrix cracking and fibre interfacial cracking. The cracking of the matrix occurs when the maximun allowable stress is reached, Fig. 2.13. In a UD lamina (0°), the cracks can develop either perpendicular (90°) or parallel (0°) to the fibre direction. Perpendicular cracks appear when pure tensile stress is applied to the fibre axial direction. If in-plane transverse stress is also applied, parallel cracks start to develop. Fibre interfacial cracking takes places when the in-plane transverse stress is pure tensile. This causes the fracture of the fibre-matrix interface, Fig. 2.13. The failure initiates in the matrix region and it propagates along the fibre length direction. Subsequently, leading to transverse fibre-matrix debonding.

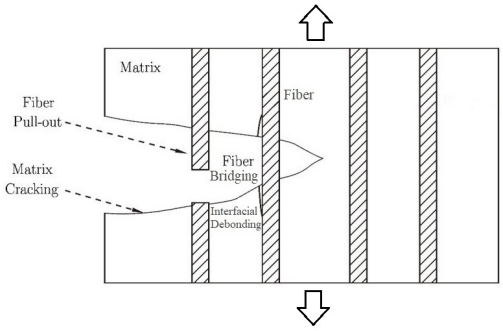

Figure 2.13. Schematic representation of different composite damage mechanisms, such as matrix cracking, fibre pull-out, fibre bridging and interfacial debonding. [Source: [39]]

In many cases, fibre-level damage leads to matrix-level damage. This is known as coupled fibre-matrix-level and typical example mechanisms are: fibre pull-out, fibre breakage (fibre fracture) and interfacial debonding, transverse matrix cracking, and fibre failure due to matrix cracking. Fibre pull-out can be apparently invisible at bare eye, Fig. 2.13. However, patches are created within the composite containing various cracks. In these cases, the fibre-matrix interface starts a fibre bridging process that

prevents the crack formation, Fig. 2.13. Thus avoiding a major loss in the matrix. After the composite failure has occured, excessive fibre sliding and pull-out can be found inside the patches. Fibre fracture and interfacial debonding occurs when the area joining the two faces of a fibre breaks because of a defect near the tip of the broken fibre. In this area, the stress concentration reaches its peak, leading to failure and fracturing the fibre interfacial bondings. Transverse matrix cracking takes place when the transverse tensile stress overcomes the maximun limiting stress in the matrix. The crack formed is likely to separate at the interface. If the stress value at the crack tip is higher than the fibre fracture stress, fibre failure due to matrix cracking will happen.

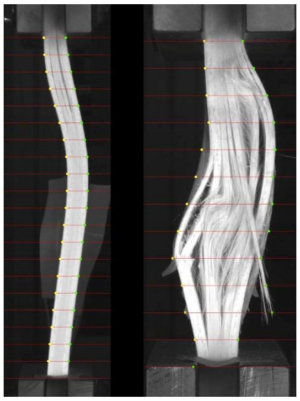

Figure 2.14. Typical GFRP delamination scenarios originated by fibre buckling mechanism. (Left) Delamination initiation. (Right) Complete delamination. [Source: [40]]

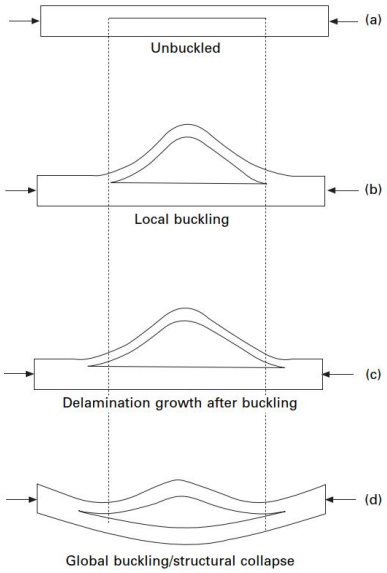

Figure 2.15. Schematic representation of a delamination example in composites originated by compressive buckling. [Source: [41]]

Macro-level damages in composites occur mainly in the form of delamination, which reduces the life of the structure. It is also the major failure

before which the ultimate failure becomes unavoidable, see Fig 2.14 and Fig. 2.15. Delamination is caused by the separation of thin composite layers bonded together (with resin). Apart from joining the composite layers together, the resin also helps distributing displacements and stress throughout the composite. The damage in the resin is due to its weakness as well as debonding from reinforcement, which hinders the stress transfer and distribution of the loading. Manufacturing defects are the major factors causing delamination since irregular and unsystematic ply arrangements, as well as mishandling during curing can weaken the bonding, [37]. In addition, formation of air bubbles or inclusions due to impurities are also potential candidates for causing failure. Transverse stresses are also responsible for the failure of the resin layer. The interface can fail during compressive or tensile loading. Nevertheless, the most common interface failure is due to tensile loads acting perpendicular to the plane axes. Compressive stresses usually tend to lead to buckling after delamination.

The transverse matrix cracking of the lamina is a combined failure mechanism, the result of micro- and macro-levels coupling damage mechanisms. "It takes places when the transverse crack propagates to magnify the damage; when a crack is formed between the adjacent layers or when partial delamination occurs" [37].

2.1.5 Cyclic loading and dynamic effects on failure

In some applications composites are subjected to cycling loading. If a material is subjected to a large number of load cycles, internal or surface flaws may appear and grow, which causes damage and material property degration in a cumulative manner. The cumulative damage is important to evaluate accurately to ensure a high reliability during the structure operation. The analysis must be done so, that the maintenance or replacement of damage components can be scheduled before a catastrophic failure happens. Fatigue analysis is used to predict the life of the structure, provided its loading history. In composites, fatigue analysis and life prediction become challenging because of the large difference among constituents properties. Traditionally the fatigue life of a material has been predicted based on $S-N$ curves, which providew with the maximun allowable stress (S) as a function of the number of loading cycles (N).

In homogeneous materials with isotropic properties (e.g. metals), the

damage is accumulated at low growth rate in the beginning of the failure process and usually one single crack propagates perpedicular to the loading axis direction. In composites, especially in laminates with multiple plies, the fracture behaviour is charaterized by several cracks originated through multiple damage modes, such as crazing and cracking of the matrix, fibre/matrix debonding, fibre fracture, ply cracking, delamination, void growth and multidirectional cracking. These mechanisms and the damage caused depend on the properties of the constituents, their geometrical configuration and the loading type. Moreover, they appear relatively early in composites fatigue life.

Unlike for homogenenous materials, the crack initiation and growth mechanisms are quite complex for composites. An UD composite loaded under tensile stress in fibre direction, can experience cracks initiation at different locations, different directions and simultaneously (e.g. in the matrix perpendicular to load direction, in the fibre-matrix interface...). Models such as the Paris Law are used to describe fatigue crack propagation of composites, although it is limited to UD laminates. Traditional fracture mechanics (e.g. LEFM) are not usually valid for composites fatigue analysis, thus advanced fracture mechanics methods are required.

$$D = 1 - \frac{E}{E_0} \tag{2.1}$$

The concept of damage accumulation D is a good approach used to predict fatigue life in composites. This quantity is evaluated in terms of the composite stiffnesses, both of the damaged material (E) and undamaged material (E_0), as shown in Eq. 2.1. The accumulated damage takes values in the range from 0 to 1, where 0 indicates no damage and 1 complete failure. Fig. 2.16 shows a comparison between the damage accumulation in composites and homogeneous materials as a function of the fatigue cycle ratio. As mentioned earlier, Fig. 2.16 proves that fatigue damage in composites appear earlier than in homogeneous materials.

The complexity of composites leads to the presence of several damage modes. As explained in [42], the usual fatigue process is as follows: Damage modes appear at the early stages of fatigue life. The damage accumulates quickly during the first few cycles. Microcracks initiate in multiple locations in the matrix. Debonding takes places at the weak fibre-matrix interfaces and some fibres may start to break during this stage. On the

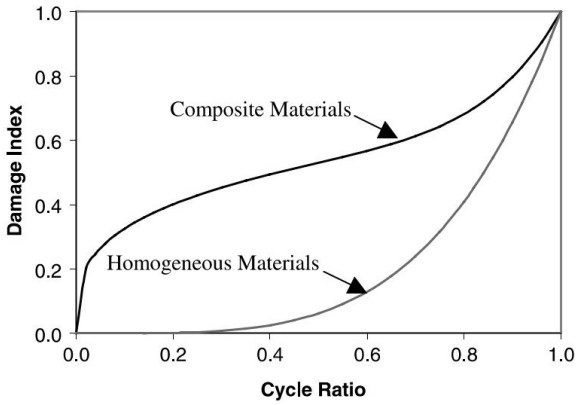

Figure 2.16. Fatigue damage accumulation comparison between composites and homoegeneous materials. [Source: [42]]

second stage, a slow and steady damage growth rate occurs. Eventually, during the last stage the damage grows rapidly before fracturing. However, this process only applies when the fatigue loading repeats some certain load profile as a function of time. Sometimes the fatigue loading can have a spectrum where no specific profiles are repeated.

The strain rate is defined by [43] as the change in strain (deformation) of a material with respect to time. High-strain rates are events occuring during a short time frame, which tend to increase the elastic properties values. Conversely, low strain rates occur over longer periods of time, making the viscous and relaxation effects to gain importance in the material behavior. Composites are highly strain-rate dependent materials, as their mechanical properties are affected by strain-rate effects, [44]. Properties such as tensile and compressive Young's modulus experience changes if the strain rates are high. Both [43] and [45] have proven that the intralaminar fracture toughness of laminates is very sensitive to strain-rate effects, indicating that fracture toughness K_{IC} and strain energy release rate G_{IC} are linearly dependent on the strain rate.

The strain-rate effect on the energy absorption and failure modes of polymer composites can be determined through two main test methods: the quasi-static and the impact test. The quasi-static test describes the energy absorption capability of the composite under crushed axial loading. Impact test reproduce the structure behaviour during the real crash since it includes the change in crushing speed, as the specimen absorbs the impact energy.

In high-speed impact applications the strain-rate is usually high, whereas for low-speed impact cases the mechanical properties can be assumed to be the same as in a static case, [46]. High-strain rates tend to increase stiffness, tensile strength and ultimate strain, as shown in [43]. A significant increase in the strain energy release rate and fracture toughness with increasing values of strain rate is shown in the results from [47]. Thus, it is concluded that a toughness enhancement is achieved with strain rate increase, under compressive loading in the dynamic regime. Reliable data on the dynamic properties of composites are limited due to the experimental difficulties for their determination, as mentioned in [46]. Failure modes also experience different behaviours depending on the strain-rate, e.g. fibres undergo brittle failure at high strain-rates, while ductile failure is present at low strain-rates.

Composites can heat up internally because of fatigue cyclic loading and high-rate loading. This heat cannot be easily dissipated due to the low thermal conductivity of polymer composites. How much the composite is heated up, it depends on the test rate and deformation range per cycle. According to [48], internal heating becomes important above 20 Hz. The faster the heat is dissipated, the better fatigue resistance the composite will present. Carbon fibres have higher thermal conductivity than glass fibres, which is one of the reasons why CFRP show better fatigue resistance characteristics than GFRP, as observed in article [49]. Internally generated heat can lead to creep, which is an irreversible strain produced by constant loading and under the presence of temperature. Unlike homogeneous materials, the rate of creep in composites does not always increase with increasing temperature due to their complex nature. Thermal effects can also generate internal stresses within laminates, as explained in chapter 10 in a book [50]. Such stresses are mainly generated due to differences in the coefficient of thermal expansion along the different main axes of the composite. Generated residual streses can lead to interlaminar weakness and warpage. Thermal stresses are more critical in laminates consisting of 0° and 90° plies since the thermal expasion undergoes a greater mismatch between those directions. For this purpose, $\pm 45°$ layer orientations are recommended, especially in composites subjected to thermal gradients [48].

2.2 Multi-scale modelling

Multi-scale modelling (MM) is defined as "the field of solving physical problems, which have important features at multiple scales (spatial or temporal)", [17]. ACMs are multiphased materials that present relevant levels of scale for their analysis. Typical MM comprises of three scales: micro, meso and macro scales. The micro scale corresponds to the constituent level (fibre, matrix and interphase). The mesoscale can represent the laminate, textile, bundles or stiffened-panel level. The macro scale belongs to global level or the real structure (aircraft wing, fuselage panel, etc.). To move from one scale to another, in general two main techniques are used. Moving from a lower to a higher scale is done by means of upscaling (also known as homogenization), whereas descending from a higher to a lower scale is done through downscaling (also known as localization). The terminology used depends on each author. In this work the terms used follow the book by Aboudi [17]. A homogenization method predicts the behaviour of the material at macro-scale by means of the elastic properties of the micro-constituents. Conversely, localization provides with the elastic properties of the micro-constituents given the behaviour of the material at macro-scale. Several homogenization techniques exist to determine the effective properties given the constituents. These vary from analytical approximations, i.e. Voigt/Reuss or Halpin-Tsai, to accurate numerical methods, i.e. FEM. Homogenization uses micromechanical models, while macromechanics are used for localization. In macromechanics, the composite is considered to have anisotropic material behaviour. Hence it requires of multiple experimental parameters at the macroscopic level. These parameters are usually measured from standarized testing. Fig. 2.17 illustrates the different levels in multi-scale modelling of composites, as well as the ascending and descending directions of homogenization and localization techniques, respectively.

MM of ACMs has been attempted in the past using a global-to-local approach (macromechanical) according to a scientific article [51]. This strategy is useful from the structural engineering point of view. However, the nature of composite models limits the capability to extend the results to design optimized lay-up configurations or to perform simulations on components that present different damage mechanisms simultaneously. Instead, a micro-to-global procedure (micromechanical) is often selected.

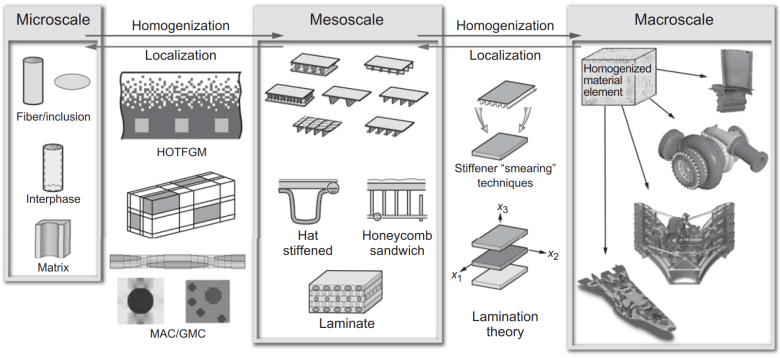

Figure 2.17. Different levels in composites multi-scale modelling. [Source: [17]]

A typical MM takes advantage of the natural separation of length scales between different entities (constituents, plies, laminate and structure) and utilizes the transfer of information between these different length scales, rather than by coupling different simulation techniques.

In the framework of multi-scale simulation of ACM, micro-scale approaches are applied to predict effective stiffness and strength properties of transversely isotropic constitutive properties of composites. For the modelling of the fibre-matrix level a typical approach is using micromechanics. The purpose of micromechanics is "to consider a material's heterogeneous microstructure and to let it be treated as an effective continuum at a higher length scale", as described by the book [17]. For that, micromechanics employs a representative volume element (RVE) at the fibre-matrix scale.

Different authors provide with slightly different definitions of an RVE. In the book [17], an RVE is defined as a volume of material whose effective behaviour is representative of that of the material as a whole, such that the physical and geometrical properties of the microstructure are identified within the RVE. On the other hand, a PhD dissertation [52] states that an RVE is a model of a material microstructure to be used to obtain the response of the corresponding homogenized macroscopic continuum in a macroscopic material point. Other definition found in a work [53] requires the RVE to be a statistically representative sample of the microstructure. This means to include a sampling of all possible microstructural configurations found in the composite, which in the case of non-regular and non-uniform microstructures it would lead to large RVE´s sizes. Conversely, if the RVE is characterized as the smallest microstructural volume that sufficiently accurately represents the overall macroscopic properties of the composite, it would lead to much smaller RVE sizes. Moreover, the

minimun RVE size does not always lead to adequate distribution of the microfields within the RVE, [52]. Hence, the RVE must contain a large enough volume capturing the essence of the fibre-matrix interaction from a statistical point of view. That is to say, it should be large enough to represent the microstructure without introducing non-existing properties such as undesired anistropy. At the same time it should also be small enough to allow efficient computational modelling. This is well-reflected in the research [54], which claims that an RVE is well-defined if it reflects the material microstructure and if the responses under uniform displacement and traction boundary conditions coincide. By the aformentioned, it can be understood that an appropiate RVE for each study case must be selected and the RVE choice is a delicate task.

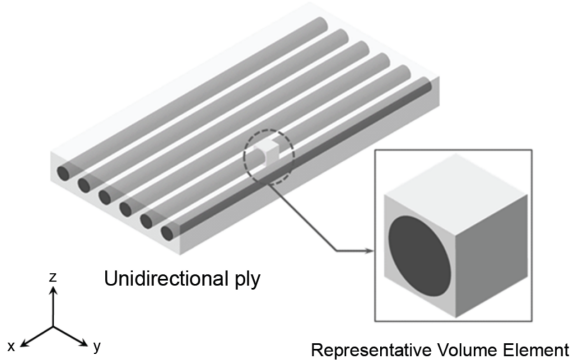

Figure 2.18. RVE (Square configuration) in a unidirectional continuous fibre composite ply. [Source: EMBRAER, [55]]

The homogenized model is subjected to loads or displacements through 6 different boundaries conditions (BCs) along the spatial directions in order to determinate the stress and strain field that would simulate the local behaviour of the composite structure [17]. The RVE is often used as first level of the multi-scale modelling, where simulations are performed to predict the fibre-matrix response. The obtained response will be used as input data for the upcoming level. A typical RVE geometry in continuous fibre composites consists of a representative sample of the fibres contained inside a cubic volume of matrix material, as shown in Fig. 2.18. There exist several options to define a RVE that depend on the fibre array selected from the composite cross-section. Fig. 2.19 shows two commonly used RVE options. Additionally, some RVE designs account for the fibre-matrix interface, which is usually included as a thin circumferential region in-between the fibre and the matrix. In terms of modelling, adding the interface is equivalent to including a third phase in the RVE configuration.

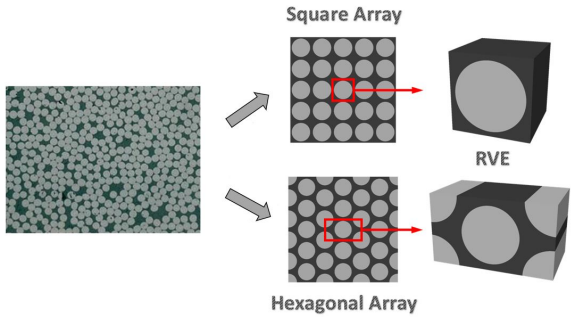

Figure 2.19. Cross-sectional view of a continuous fibre composite, fibre array options and their corresponding RVE (square and honeycomb).

Optical microscope observations have revealed that the fibre in continuous long-fibre reinforced composites is randomly distributed through the matrix and it does not follow as ordered patterns as theory states, [56]. The randomness of the fibres distribution does not always allows to define clear patterns for the RVE design. New algorithms have been developed for generating statistically equivalent RVEs of fibre-reinforced composites, [57]. The proposed methods have demonstrated significant advantages in capturing the realistic fibre distribution and have presented a good match with experimental results. However, FE models developed with the random RVEs have also shown that the fibre distribution randomness has relatively low effect on the effective elastic properties determination, as concluded in article [58]. For such applications periodic RVEs models are more suitable.

In composites' computational analysis periodic RVE models are often employed. A deterministic and ordered fibre distribution on the composite is considered in periodic models. Real composites do not fully comply with this assumption since they present random fibre distributions. To model composites with random fibre distribution is computationally more expensive than assuming it to be periodic. The article [56] investigates if it is worthwhile to use the random distribution model by performing a comparison between periodic and random models of UD CFRPs. This is done by comparing and quantifying the differences in the stress and strain microfields obtained with two RVEs, one based on a periodic model and another on a random fibre distribution model. Statistical tests for the mean and variance of the strain components are perfomed and the histograms for differen failure variables are analyzed. The results of the investigation conclude that periodic models are useful in simulations aiming to determine the effective properties of the composite, as suggested by

the work [58]. On the other hand, random models are particulary helpful when local and damage phenomena need to be modelled, such as matrix cracking, fibre-matrix debonding or failure. These are usually responsible for the macroscopic damage and failure of composites. The authors of work [56] claim: "For any statistical analysis only random models should be used, as the use of periodic models could lead to underestimation of matrix cracking and damage initiation". In addition, the use of random models provides with information for realibility analysis, which cannot be obtained from deterministic models.

The RVE (micro-scale) is used to predict the ply properties from the thermo-mechanical properties of the constituents, along with the volume fraction and spatial distribution of the fibres within the ply. Once the response of the ply microstructure is known, it is transfered to the meso-scale, which uses FEM to determine the mechanical response of laminates. The virtual laminate is built by stacking plies with different fibre orientation, and the geometrical model includes each ply and the interfaces between plies.

Meso-scale models are limited to small geometries, as extending them to structural components would be computationally expensive. Therefore the response obtained from the meso-scale is transferred to the macro-scale, which consists of the real composite structure. This large scale involves experimental tests such as impact, loading, deformation, etc. that are simulated by means of the corresponding numerical methods. In this scale, the laminate is modelled either with shell or solid elements and the different plies of the laminate are usually not modelled independently. The goal is to include, at least, as many integration points through the laminate thickness as the number of layers forming the laminate. An integration point, i.e. Gauss point, is the point within an element at which integrals are evaluated numerically. These points are chosen in such a way that the results for a particular numerical integration scheme are the most accurate. Depending on the integration scheme selected, the location of these points will vary.

The ultimate goal of MM is to integrate all scales to perform virtual mechanical testing of composites, as accurate as possible. This is a discipline called integrated computational materials engineering [51], which aims

to improve the efficiency and effectivity of materials development, design, process optimization and manufacturing. Current commercial software packages, such as Altair Multiscale Designer™ [59], provide with tools to perform composites MM, as well as simulation of composite manufacturing processes (i.e. injection molding).

One of the key issues in MM is the homogenization process used to predict the macroscopic behaviour of heterogeneous materials given their material constituents. There exist many homogenization tehniques in the literature, which show different degrees of complexity. The simplest method may be the well-known Rule of Mixtures (RoM), which is meant to homogenize the elastic properties of a heterogeneous material based on the volume-fractions average of the constituents properties. More sophisticated methods were developed in the late 50s and early 60s, such as the effective medium approximation [60] and its extension [61]. However, they still did not work for phases with high differences in properties, neither they managed to describe the behaviour of clustered structures. Variational boundary methods improved the estimation of advanced composite properties, [62]. Approaches based on mathematical asymptotic homogenization theory were developed during the late 80s and 90s, [63]. This type of homogenization provides with effective overall properties, and local stress and strain values. Even so, their application is still limited to simple microscopic geometries, material models and small strains, [52]. During the 90s the unit cell methods gained a lot of importance thanks to the development of computational methods. They provide with good results for local microstructural fields and effective material properties, although they start to have problems when the constitutive behaviour is non-linear. Hence, "most of the known homogenization techniques are not suitable for large deformations nor complex loading paths", [52]. In the end of the 20th century and during the beginning of the 21st century, the so-called multi-scale computational homogenization approach was developed, whose fundamental principles were already presented in [64] back in 1985. These micro-macro modelling procedures allow their use and implementation on FEM, [65] and [52]. Nowadays, the computational homogenization techniques are the most efficient and the most widely used methods. The most commonly used computational homogenization technique is the first-order scheme. Higher-order methods such second-order schemes also exist, e.g. the one proposed in the thesis [52]. Each approach has its own limitations

and therefore, their applicability is restricted. In terms of computational efficiency, lower-order methods will be always preferred since computational power and time will be reduced. However, to account for certain effects in complex problems higher-order schemes may be necessary. Therefore, a balance between quality of results and computational costs needs to be found.

2.2.1 Homogenization computational methods

Computational homogenization is a multi-scale technique based on the derivation of the local macroscopic constitutive response from the material microstructure through an adequate construction and solution of a microstructural boundary value problem (BVP), [52]. The computational homogenization technique has proven to be useful in retrieving the macroscopic mechanical response of non-linear multi-phase materials, despite the high computational efforts involved in the fully coupled multi-scale analysis.

The principles of the classical first-order homogenization scheme are:

- The definition of a RVE, whose individual constituents behaviour is assumed to be known.
- The formulation of the microscopic boundary conditions (BCs) from the macroscopic input variables and their application on the RVE.
- The calculation of the macroscopic output variables from the analysis of the deformed RVE.
- Obtaining the numerical relation between the macroscopic input and output variables.

Following the principle of separation of scales, the microscopic length scale should be much smaller than the characteristic size of the macroscopic sample or the wave length of the macroscopic loading. Most homogenization approaches assume global periodicity of the microstructure, which means that the whole macroscopic specimen consists of spatially repeated unit cells. However, in the computational homogenization approach a local periodicty assumption is proposed, which is more realistic. The microstructure may have different morphologies at different macroscopic points, while it would repeat itself in a small vicinity of each individual macroscopic point. The local periodicity assumption allows to model the effects of non-uniform microstructure distributions, as it occurs in com-

posites. The concept of local and global periodicity is illustrated in Fig. 2.20.

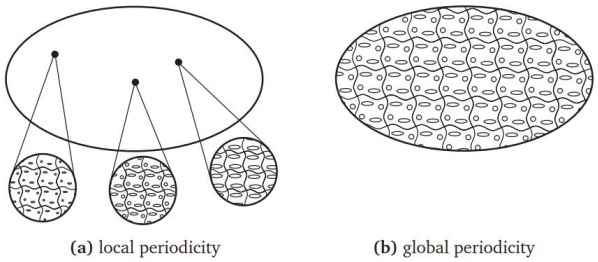

Figure 2.20. Schematic representation of a macrostructure with local (a) and global (b) periodic microstructures. [Source: [52]]

In first-order computational homogenization schemes a macroscopic deformation (gradient) tensor $\mathbf{F}_{\mathrm{M}}$ is calculated for every material point of the macrostructure. This would correspond to the integration points of the macroscopic mesh within FEM. Then, $\mathbf{F}_{\mathrm{M}}$ is used to formulate the kinematic BCs to be imposed on the microstructural RVE that is assigned to this point. Once the solution of the microstructural BVP is obtained, the macroscopic stress tensor $\mathbf{P}_{\mathrm{M}}$ is calculated by averaging the resulting microstructural RVE stress field over the volume of the microstructural cell (RVE). The result is a numerical stress-strain relationship at every macroscopic point. Besides, the local macroscopic consistent tangent is derived from the microstructural stiffness. The outlined scheme process is shown in Fig. 2.21.

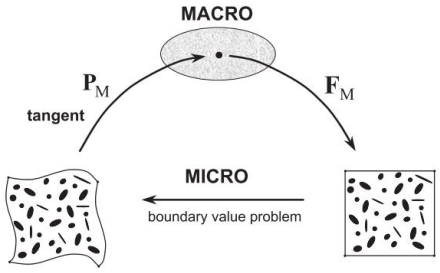

Figure 2.21. Schematic representation of the first-order computational homogenization scheme. [Source: [52]]

The micro-macro procedure described above is said to be "deformation driven", as given the macroscopic deformation gradient tensor $\mathbf{F}_{\mathrm{M}}$, the stress $\mathbf{P}_{\mathrm{M}}$ and the constitutive tangent are determined based on the response of the microstructure. It is also possible to follow a "stress-based" procedure, but it is not often used because it does not match with the standard displacement-based FEM used to find the BVP macroscopic solution. The macro-to-micro transition is performed by imposing the macroscopic

gradient tensor $\mathbf{F}_M$ on the microstructural RVE through a specific approach. Simple procedures such as the Voigt or Reuss assumptions do not require a detailed microstructural modelling, but they provide very rough estimation of the overall material properties and are not suitable for non-linear regimes. Therefore, more accurate averaging strategies need to be used, which require the solution of the detailed microstructural BVP. The transfer of the macroscopic variables to the microstructural RVE is done through the BCs. Typically three main types of RVE boundary conditions are used: prescribed displacements, prescribed tractions and prescribed periodicity. Additional types of RVE BCs are possible, as far as they are consistent with the so-called averaging theorems. BCs and averaging theorem will be covered in section 2.2.3.

In a PhD disseration [52] a first-order computational homogenization method is developed and its actual implementation is based on the solution of two nested BVPs, one for each scale (microscopic and macroscopic).

First-order computational homogenization has several advantages. First, it is not required to specify the homogenized macroscopic constitutive behaviour, which is generally a difficult task in the case of large deformations and complex microstructures. Instead, the constitutive behaviour at the macroscopic integration points is determined by averaging the results of a detailed microstructure modelling. This allows the method application to geometrically and physically non-linear problems. Second, the macroscopic constitutive tangent operator is derived from the total microscopic stiffness matrix. Third, the consistency is preserved through the scale transition and the method deals with large strains and large rotations in a trivial way. Moreover, the RVE problem is a classical BVP, for which any appropiate solution strategy can be used.

As mentioned in section 2.2, some limitations restrict the applicability of the first-order computational homogenization scheme. These originate from the fundamental assumption that the microstructural length scale is negligible in comparison with the macrostructural characteristic length. Based on the concept of separation of scales, it is justified to assume macroscopic uniformity of the deformation field over the RVE. However, this implies that only simple first-order deformation modes of the microstructure are found, such as tension, compression, shear or combinations thereof.

The bending mode cannot be properly captured. As the size of the microstructure is considered irrelevant, i.e. the results are insensitive, the microstructural and geometrical size effects cannot be predicted. Moreover, the approach is not applicable in regions with large gradients of the deformation field since the uniformity assumption of the macroscopic defomation over a RVE is not valid anymore. These are regions where the characteristic wave length of the macroscopic deformation field is of the order of the microstructure´s size. Besides, if softening occurs at a macroscopic material point, the solution from a first-order homogenization scheme becomes mesh dependent.

The limitations of the first-order homogenization method give rise to the development of the second-order computational homogenization approaches, such as the one proposed in a PhD thesis [52]. This method aims to obtain the constitutive response of a second gradient continuum, based on the behaviour of the underlying microstructure. It extends the classical computational homogenization technique to a full-gradient geometrically non-linear approach. The macroscopic deformation gradient tensor $\mathbf{F}_\mathrm{M}$ and its gradient ${}^3\mathbf{G}_\mathrm{M} = \nabla_{\mathbf{0}_M}\mathbf{F}_\mathrm{M}$ are imposed as BCs on the microstructural RVE. For the RVE, the periodic BCs are generalized since the classical periodic boundary conditions cannot be applied in the case where an RVE is subjected to a non-zero gradient of deformation. All microstructural constituents are treated as classical continuum, described by standard first-order equilibrium and constitutive equations. Hence, the microstructural BVP remains classical. After the BVP solution of the RVE is obtained, a macroscopic stress tensor (the first Piola-Kirchhoff stress tensor $\mathbf{P}_\mathrm{M}$) and a higher-order stress tensor ${}^3\mathbf{Q}_\mathrm{M}$ are derived using the Hill-Mandel energy condition. The first Piola-Kirchhoff stress tensor $\mathbf{P}_\mathrm{M}$ describes the material behaviour of each microstructural constituent by means of its constitutive law, specifying a time and a history dependent stress-strain relationship. The ${}^3\mathbf{Q}_\mathrm{M}$ is a third order tensor, which is defined as the work conjugate of the gradient ${}^3\mathbf{G}_\mathrm{M}$ of the deformation gradient tensor. The ${}^3\mathbf{Q}_\mathrm{M}$ can be interpreted as the first moment with respect to the RVE center of the microscopic first Piola-Kirhhoff stress tensor $\mathbf{P}_\mathrm{M}$ over the initial RVE volume V_0. The microstructural problem remains classical, whereas macroscopically a full gradient second-order equilibrium problem appears. This provides the microstructurally based constitutive response of the higher-order macrocontinuum without making

any additional assumptions. The outlined scheme process is illustrated in Fig. 2.22.

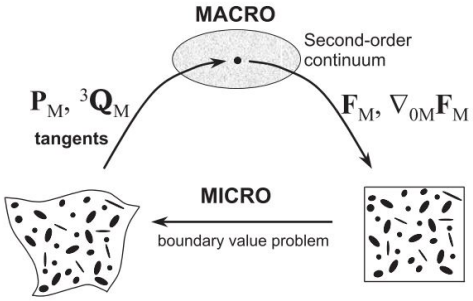

Figure 2.22. Schematic representation of the second-order computational homogenization scheme. [Source: [52]]

The actual FEM implementation of a second-order computational homogenization method is presented in the PhD disseration [52]. As for the first-order homogenization case, the implementation is based on the solution of two nested BVPs, one for each scale (microscopic and macroscopic). The proposed implementation is built on the basis of parallel computation, as the multi-scale algorithm developed is parallel. This means that all RVE calculations for one macroscopic iteration are performed at the same time without any exchange of data among them. The use of parallel processors for the RVE analyses is meant to reduce the total micro-macro calculation times.

The second-order homogenization has also some limitations. The RVE is required to be statistically representative as in the case of the first-order homogenization. However, in this case there is a restriction on the maximun size of the the RVE because the second-order method models the macrostructure as a higher-order continuum, while the first-order method dealt with an ordinary local continuum on the macroscopic level. The continuum in the first-order case does not present a material length scale, thus the RVE size did not play a role. Conversely, the continuum length scale in the second-order method is related to the size of the microstructural cell. Another important issue is the assumption that the macroscopic deformation field varies linearly over the RVE. If this assumption does not apply, for example if the macroscopic fields vary too strongly on the micro-constituents scale, the homogenization scheme cannot provide accurate results, as the concept of separation of scales does not apply anymore.

2.2.2 Data flow between modelling scales

A key aspect of Multiscale Modelling (MM) is the data flow and transfer between modelling scales. To perform an analysis on the next length scale from the local scale, it is needed to link the state variables predicted on the microscale and properly transfer them into the macroscale. One typical way is to link the microscale to the macroscale through the use of mean fields, as explained in section 11.4.2 of the paper [66], where the mathematical expansion for the stress in the macroscale is expressed in terms of the microscale stress. This derivation uses the volume averaged stress (mean stress) at the microscale. Thus, the macroscale analysis is performed in terms of the mean stress. If there is localization due to damage or large strain gradients, the higher-order terms cannot be neglected. In this case the mean field theory does not apply anymore and a non-local approximation, or a full field analysis is required to be perfomed in all scales simultaneously in order to obtain accurate results.

Multiscale algorithms have been developed to simultaneously obtain approximate solutions to problems at different lenght scales. One general formulation of a time-stepping algorithm is proposed in a scientific article [66]. The schematic flow chart of the computational algorithm is illustrated in Fig. 2.23. The algorithm starts by calculating the global solution for a small time step assuming some initial state. Then, the global solution for the first step is used to compute solutions for each integration point at the local scale by using the state variables obtained as output from the global analysis. The results obtained in each integration point are homogenized to generate the global constitutive equations for the next time step at the global scale. The process described and illustrated in Fig. 2.23 is an operator splitting technique, which considers one-way coupling between the two-length scales. The accuracy of the method is improved if smaller times steps are used until convergence is reached. The procedure described in here (see Fig. 2.23) contains only two scales. However, the same procedure can be used with more scales, as long as the limits of continuum scales (10^{-10} m $< l < 10^{3}$ m) are kept and the separation between length scales is good enough. The author in the work [66] suggests that probably five or six length scales are physically possible, which allows to solve almost any multiscale problem since most of the current technological problems only require a maximun of three scales.

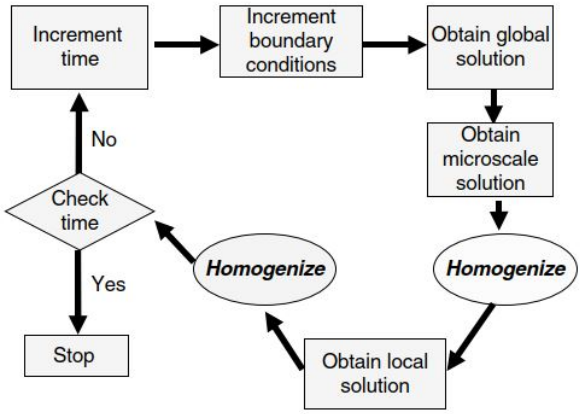

Figure 2.23. Flowchart illustrating a multiscale computational algorithm. [Source: [66]]

2.2.3 Boundary conditions

As previously mentioned in section 2.2.1, there are three main types of RVE boundary conditions: affine (or prescribed) displacements, uniform (or prescribed) tractions and prescribed periodicity, [52]. To introduce them in this work a 2-dimensional anisotropic RVE will be considered for simplification reasons, as the one shown in Fig. 2.24. In Fig. 2.24 the numbers 1 to 4 correspond to the corner points of the RVE, Γ denotes the RVE boundaries and $\vec{N}$ are the normal vectors to the RVE boundaries. The initial position vector of any point in the RVE reference domain V_0 is denoted by $\vec{X}$ and the actual position vector in the current (deformed) domain V is denoted by $\vec{x}$.

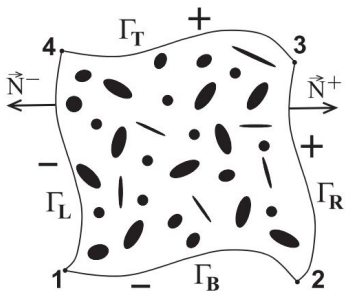

Figure 2.24. Schematic representation of a 2-dimensional RVE. [Source: [52]]

The affine displacement BCs can be expressed through the linear mapping condition of the RVE boundary, as follows in Eq.2.2.

$$\vec{x} = \mathbf{F_M} \cdot \vec{X} \quad \text{with} \quad \vec{X} \quad \text{on} \quad \Gamma_0 \tag{2.2}$$

In Eq. 2.2 $\vec{x}$ is the position vector of a point on the RVE boundary in the deformed shape and Γ_0 is the undeformed boundary of the RVE with domain V_0. The tensor $\mathbf{F_M}$ is the macroscopic deformation gradient.

The uniform traction BCs can be defined in terms of the normal vectors to the deformed (Γ) or undeformed (Γ_0) RVE boundaries. These vectors are denoted by $\vec{n}$ and $\vec{N}$ respectively. The traction BCs are given by Eq. 2.3.

$$\vec{t} = \vec{n} \cdot \sigma_{\mathbf{M}} \quad \text{on} \quad \Gamma \quad \text{or} \quad \vec{p} = \vec{N} \cdot \mathbf{P_M} \quad \text{on} \quad \Gamma_0 \tag{2.3}$$

In Eq. 2.3, σ_M is the Cauchy stress tensor and $\mathbf{P_M}$ the first Piola-Kirchhoff stress tensor.

Periodic BCs are based on the periodic microstructure assumptions presented in section 2.2.1. These BCs represent the periodic (Eq. 2.4) and antiperiodic (Eq. 2.5) deformations of the RVE boundaries.

$$\vec{x}^{+} - \vec{x}^{-} = \mathbf{F_M} \cdot (\vec{X}^{+} - \vec{X}^{-}) \tag{2.4}$$

$$\vec{p}^{+} = -\vec{p}^{-} \tag{2.5}$$

The estimation of the material properties obtained when using periodic BCs is better than when prescribed displacements or tractions BCs are used. If the general periodic BCs definitions from Eq. 2.4 and Eq. 2.5 are applied to the RVE example in Fig. 2.24, they will adopt the form in Eq. 2.6 and Eq. 2.7. In there, the subindexes L, R, B and T of the position vectors denote the left, right, bottom and top boundaries of the RVE, whereas the numbers 1 to 4 correspond to the corner points of the deformed RVE.

$$\vec{x}_R = \vec{x}_L + \vec{x}_2 - \vec{x}_1 \tag{2.6}$$

$$\vec{x}_T = \vec{x}_L + \vec{x}_4 - \vec{x}_1 \tag{2.7}$$

Periodicity BCs are applied on the RVE from a published paper [67] in order to keep a periodic microstructure and to model the fibre-matrix interface fracture of a C/PEEK composite. The RVE undergoes transverse compression and longitudinal shear. The periodic BCs are applied to the RVE sides following a zigzag-like shape and they are formulated based on the displacement vectors that relate opposite faces of the RVE. The BCs repetition forces the cracks to form, so that the repetition prevails in the RVE. This is due to the fact that the RVE sides are symmetric. Therefore, it can be withdrawn from the paper [67] that the simulation results in this

case are governed by the prescribed periodic BCs in the RVE, which to be accurate it should not occur in reality.

As already mentioned in section 2.2.1, other types of RVE BCs may be formulated as long as they are consistent with the averaging theorems. The averaging theorems were first proposed by the work [54] and they are essential for the coupling and the consistency between the micro and macro scales in multiscale FE procedures, [68]. These theorems are the strain averaging theorem, the stress averaging theorem and the energy averaging theorem (also known as Hill-Mandel principle of macrohomogeneity). The strain and stress averaing theorems are also known as Hill's theorems. Both Hill's theorems and the Hill-Mandel principle of macrohomogeneity state that "*the average strain and stress over the RVE are appropiate macroscopic quantities with which to describe the homogenized constitutive behaviour, both in the linear and finite kinematic setting*", [68]. These relations and their extensions to include surface discontinuities, body forces or inertial terms do rely on the application of the divergence theorem on the strong form of the equilibrium equation. In case of the stress field being discontinuous across elements, these relations still hold although the divergence theorem is no longer applicable to prove them. This is shown in a scientific publication [68], where discrete averaging results are derived for the three typical BCs types (previously presented). The analytical proofs are confirmed by a simple numerical FE simulation on an irregular RVE undergoing large deformations. In addition, the proofs are extended to include body forces and inertia effects, showing a good match with the results in the smooth continuum configuration.

2.2.4 Contact formulations

A contact is a boundary non-linearity, which takes places at the boundaries of two or more bodies that are in contact. In composites modelling, contact problems often appear in the fibre-matrix interface contact region, as well as in-between laminate plies. From the FEM point of view contact problems are complicated because the contact boundary is a priori unknown, they originate abrupt changes in the force profile that cannot be determined from the displacements field and, unlike in a continuum, the contact boundaries vary from node to node in a discretized domain, [69].

The slave-master concept is important for FE contact implementation.

As a rule of thumb, the nodes on the slave boundary cannot penetrate the surface elements on the master boundary. This is known as the concept of impenetrability, where a body 1 cannot penetrate a body 2, when both bodies may be considered to be close enough to be in contact with each other. The non-linearity arises from the fact that the contact boundary and stress are a priori unknown, [69]. Therefore, in a contact problem a candidate boundary is always given beforehand. When the contact occurs, the contact force cannot be directly determined from the displacement's field and an extremely discontinuous force profile appears. In a continuum, the contact force varies smoothly, whereas in a discrete FE model the contact boundary varies from node to node. Because of the unknown nature of the contact boundary, contact points need to be found either by direct search or by a non-linear constraint equation. Both methods required an iterative process to determine the contact boundary and force. A smooth non-linear contact function is used to alleviate the abrupt change in the contact condition.

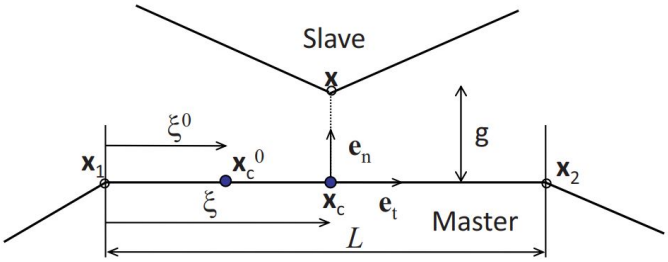

Figure 2.25. Schematic representation of a generic FE contact formulation problem. [Source: [69]]

In a slave-master contact problem, the rigid body (typically the master) has a fixed or prescribed displacement. A point x of the flexible body (typically the slave) is projected onto the piecewise linear segments of the rigid body, x_c point (see Fig. 2.25). The distance between the points (gap) is calculated. If the gap > 0 the contact condition is not fulfilled, whereas if the gap < 0 the contact occurs.

The distinction between slave and master is only made for numerical convenience. As stated earlier, the contact condition is said to be: "the slave body cannot penetrate into the master body". Thus, the master body can penetrate in the slave body, which is physically not possible, but numerically it is not checked, [69]. In practice, the rigid surface is usually chosen to be the master, while convex and fine mesh surfaces are preferred to act as the slave.

For the contact search in a FE code (also known as contact discretization), the user can specify which slave node will contact with which master segment. This works only for limited cases when the deformation is small and no relative motion exists in the contact surface. In these cases, the slave and master nodes are located in the same position and connected by a compression-only spring. This is known as node-to-node contact. In general, the user cannot specify exactly which slave node will contact with each master node, but he/she needs to specify candidate nodes. Then, the contact algorithm will search for a contacting master segment for each node. However, this is a time consuming process because it needs to be performed for each iteration. Two main contact discretization approaches can be distinguised, node-to-surface (N2S) and surface-to-surface (S2S), see Fig. 2.26. Most of FE softwares use N2S by default, which is preferred for finer mesh cases. S2S is usually more computationally expensive than N2S in both space and time, but it can produce a smoother contact force, [70].

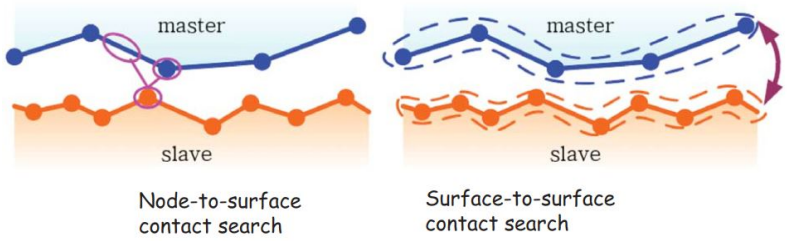

Figure 2.26. Schematic representation of the two main contact search types. [Source: [69]]

A general FE contact discretization algorithm works in a two-step procedure. First, it searches for nodes and segments that are candidates for a contact, as well as for those violating the contact condition. Once these are classified, a contact force is applied to the violated nodes. The contact tolerance is key in the detection of candidate nodes, as it specifies the minimun distance to search for a contact among all nodes. For each slave node a respective master segment will be searched, which contains the normal projection of the slave and it is within the contact tolerance value, see Fig. 2.26. If no master within the normal projection is found, then the nearest segment is picked, which is within (30 degrees relative to) the normal of the master segment. Once a feasible master is found, the contact element is created, [70].

Those contacting pairs penetrating the master body need to be corrected

by applying a contact force (opposite to the penetration direction). For this, a penalty parameter (also konwn as, contact stiffness K_n) is used. The contact stiffness depends on the material stiffness of the bodies in contact. A large contact stiffness reduces the penetration, but it can lead to convergence problems. Two main methods are used to calculate the contact force: the penalty method and the Lagrange multiplier method. In the first one the contact force is a function of the deformation, whereas in the second the contact force is a Lagrange multiplier that imposes the impenetrability condition. The contact force is applied normal to the contact boundary and it is path-independent. Instead, a path-dependent friction force can also be used. In this case, the force is applied parallel to the boundary direction and the Coulomb friction model is often used. However, in this model the friction force is indeterminate when two bodies are stuck. Therefore, improved friction models involving the tangential stiffness are also used.

There exist many types of contact formulations, which are covered in the field of computational contact mechanics. One of the most common formulations employed in composites FEA is the cohesive zone model (CZM), as presented in section 2.2 from a PhD thesis [6]. An example of contact problem is found in the discretization of the RVE used in the work [67]. The contact problem occurs in a uniform pressure situation, which is readily alleviated by using modified quadratic elements containing three extra internal DoFs corresponding to one extra internal node. The authors from the paper [67] claim that this solution has proved to increase the accuracy, by better modelling the strain gradient between fibres in the matrix.

2.2.5 Damage onset and propagation

In high-technology composites, where the matrix resin is brittle, the linear behavior ends due to micro damage. This consists of mainly micro cracks in the matrix and micro debonds at the fibre-matrix interfaces. Thus, it is important in this thesis to briefly introduce the field of fracture mechanics.

Two main issues are still unresolved in the field of damage crack propagation. One single model that may predict crack growth in inelastic media has not yet been agreed by the scientific community, neither the prediction of multiple cracks occuring simultaneously in the same material has been fully accomplished yet, [66].

The first theory of fracture mechanics was developed by Griffith based on the fundamental concepts of thermodynamics, back in 1920. Giffith's criterion states that a crack would extent in an elastic body as long as the energy released per unit area of the crack G is greater or equal to the critical energy release rate (G_c). G_c is considered as a material constant. Giffith's criterion allows to make accurate predictions of crack growth for brittle materials. However, for ductile materials the predictions are not valid because the energy dissipation does not only occur due to crack extension, but also due to the plastic zone that develops at the crack tip. Besides, the crack growth in ductile materials depends on the history of the loading too. Irwin realized that the plasticity plays a significant role in the fracture of ductile materials and he developed a modified version of Griffith´s energy citerion, which splits the energy into two parts: the stored elastic strain energy released during the crack growth and the dissipated energy due to the plasticity effects.

Irwin found out that if the size of the plastic zone around the crack is small compared to the crack size, the energy required for the crack to grow does not depend on the plastic zone at the crack tip. This means that an elastic solution can be used to calculate the energy needed for the fracture in this case. Thus, the energy release rate (ERR) was defined as the change in elastic strain energy per unit area of crack growth, as stated in Eq. 2.8, where the U is the elastic energy and a is the crack length. Eq. 2.8 can be written either under constant load P or under constant displacement u.

$$G = \left[\frac{\partial U}{\partial a}\right]_P = -\left[\frac{\partial U}{\partial a}\right]_u \tag{2.8}$$

3. Modelling, Computations and Experiments

The current chapter describes firstly the Multiscale Designer tool (MD) by Altair used in this work. Secondly, the multiscale modelling process to model the fibre-matrix interface is explained. Thirdly, the multiscale routines for impact FE-simulations are presented. These include two models: indentation (in OptiStruct) and impact (in RADIOSS). Then, the characteristics and material properties of the composite material employed are given. Finally, the experimental tests performed at the Laboratory of Materials Science of TAU are described.

3.1 Multiscale Designer tool (MD) by Altair

In the framework of Multiscale Modelling (MM) there are currently commercial software packages available, which provide with the tools to perform MM on composite materials. Such tools are usually in the form of additional modules that complement an already well-known commercial FEA software. For instance, for the case of ANSYS Workbench (Canonsburg, Pennsylvania, United States) there exists SwiftComp™ Graphical User Interface (GUI), which is an extension of ANSYS that provides an efficient and accurate approach for modeling composite materials and structures. It can be used either independently as a tool for virtual testing of composites or as a plugin to power conventional FE codes with efficient high-fidelity multiscale modeling for composites. SwiftComp™ implements a true multiscale theory to capture both anisotropy and heterogeneity of composites at the microscopic scale, or any other scale of user's interest. Another example is the Multiscale Designer™ module developed by Altair, which is the one used in the present work.

Multiscale Designer™ (MD) is a tool for development of multiscale and

single scale materials models and simulation of parts manufactured from either hetereogeneous or homogeneous materials, [59]. This includes continuous and chopped fibre composites, honeycomb structures, lattice structures, bones, etc. It allows MM for design, ultimate failure assessment, statistical-based material allowables, creep, fracture and impact simulations. In addition, it provides user material plugins to import the material model designed into commercial FEA solvers, such as Optistruct, Abaqus (implicit/explicit), ANSYS, RADIOSS, LS-DYNA and Nastran. MD GUI has a well-defined methodology for the development of multiscale materials models. The deterministic approach follows a three-step process: Unit Cell Model Definition, Linear Material Characterization and Non-linear Material Characterization. Additionally, the material models generated can easily be included in one of the macro model simulations on standard specimens offered within MD (unnotched, notched, shear and bending). Instead of implementing a pure direct homogenization (accurate but computationally inefficienct) or other classical homogenization methods (computationally efficient but inaccurate), MD uses 3D FEA Unit Cells with a Reduced Order Model (ROM) technique that allows for both predictive accuracy and computational efficiency [71]. This ROM stores all heterogeneous material behaviour from the elastic and inelastic regime into a material database by performing only a one-time solution of the unit cell. In the macro model simulations, each macro element calls into the database via the user material plugins to perform matrix algebraic calculation for the homogenized stiffness and dehomogenized phase stress and strains. Furthermore, MD implements advanced damage and plasticity laws to account for the fundamental physical behaviour of various materials (phases, constituents). One non-linear material law is assigned to each phase of the FEA unit cell. The available non-linear material laws include damage models for brittle materials, plasticity models for ductile materials, and advanced hybrid damage and plasticity models for materials exhibiting both brittle and ductile behaviour. Alternatively, MD offers a stochastic simulation approach which computes a Probabilistic Distribution Function (PDF) for the homogenized macro-scale properties given the variability of the micro-scale geometry and constitutive properties, [59].

The Altair's MD separates the composite in three different scales. Scale 1 corresponds to the fibre and matrix constituents, scale 2 represents the lamina (UD or weave) and scale 3 describes the composite laminate formed

upon stacking of several laminaes, [72]. This scale separation is illustrated in Fig. 3.1. The stress at any scale is the volume average stress of the immediate scale below. The microscopic scale of the constituents (referred as scale 0 in Fig. 3.1) is not accounted in the current versions of MD, yet.

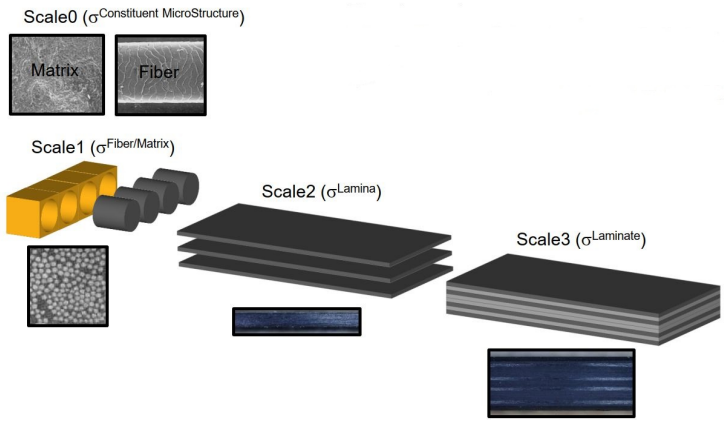

Figure 3.1. Schematic representation of the separation of scales in Altair Multiscale Designer™ for an UD composite laminate. [Source: [72]]

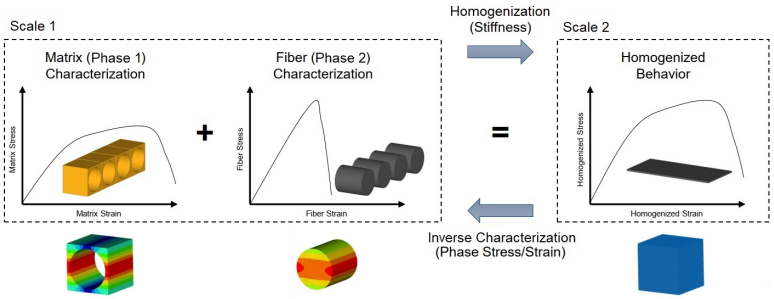

Figure 3.2. Schematic representation of homogenization and inverse characterization processes linking scale 1 and 2 in Altair Multiscale Designer™. [Source: [72]]

A key aspect of the separation of scales is the homogenization process that links them through either upscaling or downscaling. These are referred as forward homogenization and inverse characterization in MD, respectively, see Fig. 3.2. For the forward homogenization problem, the homogeneous micro-phase material properties are user-defined and the corresponding macro homogeneous properties of the heterogeneous unit cell are calculated. That is to say, given the matrix and fibre linear elastic properties (E_m, ν_m, G_m, E_f, ν_f, G_f..., respectively) the homogenized properties of linear elasticity (E_1, E_2, G_{12}...) are calculated. This is done by applying 6 different strain BCs on the defined RVE (Unit Cell in Altair nomenclature) within the linear elastic regime. Thus, the 21 independent engineering constants that define the anisotropic stiffness matrix $[C]$ are determined. The stiffness matrix $[C]$ is obtained applying the 6 BCs on the Hooke's law equation (Eq. 3.1). Eq. 3.1 is shown in Fig. 3.3 in terms

of the 21 independent engineering constants of matrix $[C]$. Finally, the anisotropic compliance matrix $[S]$ is determined by calculating the inverse of $[C]$, according to Eq. 3.2.

$$\{\sigma\}_1 = [C]_1\{\varepsilon\}_1 \tag{3.1}$$

$$\begin{Bmatrix} \sigma_1 \\ \sigma_2 \\ \sigma_3 \\ \tau_{12} \\ \tau_{23} \\ \tau_{13} \end{Bmatrix} = \begin{bmatrix} C_{11} & C_{12} & C_{13} & C_{14} & C_{15} & C_{16} \\ C_{21} & C_{22} & C_{23} & C_{24} & C_{25} & C_{26} \\ C_{31} & C_{32} & C_{33} & C_{34} & C_{35} & C_{36} \\ C_{41} & C_{42} & C_{43} & C_{44} & C_{45} & C_{46} \\ C_{51} & C_{52} & C_{53} & C_{54} & C_{55} & C_{56} \\ C_{61} & C_{62} & C_{63} & C_{64} & C_{65} & C_{66} \end{bmatrix} \begin{Bmatrix} \varepsilon_1 \\ \varepsilon_2 \\ \varepsilon_3 \\ \gamma_{12} \\ \gamma_{23} \\ \gamma_{13} \end{Bmatrix}$$

Figure 3.3. Hooke's law equation in terms of the anisotropic stiffness matrix C containing the 21 independent engineering constant to be determined. [Source: [72]]

$$\{\varepsilon\}_1 = [S]_1\{\sigma\}_1 \tag{3.2}$$

The aformentioned 6 strain boundary conditions apply a strain in one of the 6 directions, while the other 5 are constraint. This is done for all 6 directions, as stated below. Fig. 3.4 illustrates all strain components in the 3D orthogonal space and it graphically shows BCs 1, 2 and 3 applied upon the unit cell.

$$\text{BC1: } \varepsilon_1 = 1\ \varepsilon_2 = \varepsilon_3 = \gamma_{12} = \gamma_{23} = \gamma_{13} = 0$$
$$\text{BC2: } \varepsilon_2 = 1\ \varepsilon_1 = \varepsilon_3 = \gamma_{12} = \gamma_{23} = \gamma_{13} = 0$$
$$\text{BC3: } \varepsilon_3 = 1\ \varepsilon_1 = \varepsilon_2 = \gamma_{12} = \gamma_{23} = \gamma_{13} = 0$$
$$\text{BC4: } \gamma_{12} = 1\ \varepsilon_1 = \varepsilon_2 = \varepsilon_3 = \gamma_{23} = \gamma_{13} = 0$$
$$\text{BC5: } \gamma_{23} = 1\ \varepsilon_1 = \varepsilon_2 = \varepsilon_3 = \gamma_{12} = \gamma_{13} = 0$$
$$\text{BC6: } \gamma_{13} = 1\ \varepsilon_1 = \varepsilon_2 = \varepsilon_3 = \gamma_{12} = \gamma_{23} = 0$$

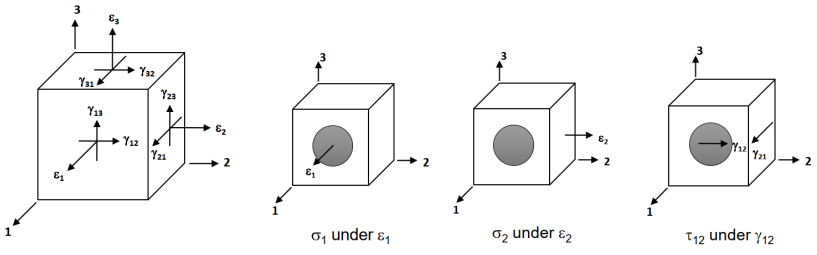

Figure 3.4. 3D strain components on the orthogonal space (left) and graphical illustration of BCs 1, 2 and 3 over the unit cell. [Source: [72]]

Once the unit cell is homogenized (still within the linear regime), MD calculates the macro homogeneous properties of the lamina or the lami-

nate. Each lamina (scale 2) is considered as a layer of unit cells (RVEs) of given orientations. A laminate (scale 3) consists of a stack of laminas with pre-defined orientations. The macro homogeneous linear material properties are calculated by solving the forward homogenization problem presented in the paper [73]. The same procedure is applied for the non-linear characterization. For the micro-macro homogenization of the non-linear part the Reduced Order Model (ROM) is used. After both the linear and non-linear forward characterizations have been computed, the stress field of the heterogeneous material is obtained. With the obtained strain and stress fields, the rest of variables are derived.

The so-called ROM aims to reduce the computational costs of the non-linear characterization of the unit cell model, as presented in a scientific article [71]. MD creates a reduced order unit cell model for the heterogeneus material system. The ROM is performed after the macro homogeneous linear material properties have been obtained, and before calculating the macro homogeneous non-linear material properties. The technique is used to reduce the total number of degrees-of-freedom (DoFs) in the unit cell problem. This involves the solution of a series of influence function problems and the resulting coefficient tensors serve as a material database of the reduced order unit cell. In the direct homogenization macro solver iteration process, for each integration point first the homogeneous strains $\{\varepsilon\}$ are solved. These strains $\{\varepsilon\}$ are applied as BCs to the micro unit cell and the non-linear problem is solved, obtaining the phase strains $\{\varepsilon\}^f$ and $\{\varepsilon\}^m$. This process is performed iteratively for each integration point of the macro-scale, which makes it very accurate. However, the process requires to go back to the micro-scale (unit cell) for each iteration, thus making the whole computation very inefficient. When using the ROM two steps can be skipped since they are unnecesary. Hence, the phase strains can be directly calculated from the homogeneous strain, without having to solve the non-linear problem of BCs on the micro unit cell.

The whole art of how MD works is seen in the reduction in computational time achieved by the ROM, especially in the non-linear characterization part. MD uses the ROM created in the linear characterization stage, so that there is no need to run the unit cell FE model again. All the relevant information of the unit cell level simulations is included in the ROM and the system only needs to perform "simple" arithmetics beyond that.

3.2 Modelling of Fibre-Matrix Interface

This work aims to obtain and use a material model of the composite where the macroscopic mechanical behaviour is based on the properties of the micro-constituents. Thus, the properties at the microstructure level would be considered in the macroscopic response. This would let study the influence of the micro-constituents properties in the macro-response of the material. For this purpose, MD turns out to be a useful tool since it allows to create a material model based on the micro-parameters of the real composite used in the experiments. A priori, this would be thought to produce a 'more realistic' material model to be used in the FE simulations of the real experiment.

For the generation of the material model, MD separates the multiscale process in three steps, as earlier explained in section 3.1: Unit Cell Model Definition, Linear Material Characterization and Nonlinear Material Characterization.

In the Unit Cell Model Definition step, a parametric model of the RVE is to be created. The model selected is 'fibrous' and the RVE configuration is a 'Honeycomb'. As input data, the 'Manufacturing data' option is chosen where the parameters CPT, Fiber Density and FAW are as stated in Table 3.5. A two-phase parametric unit cell is generated with 6019 tetrahedral elements (C3D10), where a 59.86% corresponds to fibre volume and 40.14% to matrix, see Fig. 3.5. MD offers the possibility to defined a third phase (the interphase). However, this is not modelled in the current RVE since the interphase always depends on the fibre surface treatment, exact resin composition, and also on manufacturing process. Therefore, only interphase data specifically for this fibre-resin combination as in the laminate could be used. This exactly data is difficult to find explicitly from literature.

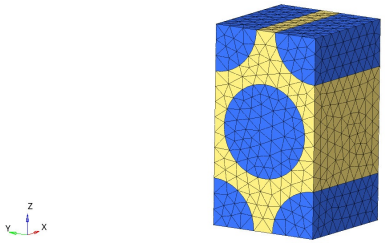

Figure 3.5. Mesh of the generated parametric unit cell (RVE) with two phases (fibre and matrix). [Source: Multiscale Designer]

In the Linear Material Characterization step a foward homogenization technique is selected. The properties for the two different phases are defined. The matrix is considered as an isotropic phase and the properties are taken from the manufacturer data sheet [74], as stated in Table 3.3. The fibre is considered as tranverse isotropic and the properties (see Table 3.2) are taken both from the manufacturing data sheet, as well as from literature [75]. For both phases, the compressive Young's Modulus is assumed to be the same as in tensile because the data in compression is not usually available and the assumption is feasible in practice.

In addition to the micro material properties, a quasi-isotropic laminate is defined as a lay-up in the Linear Material Characterization, as shown in Fig. 3.6. The lay-up consists of 4 plies and it is symmetric, which makes a total of 8 plies.

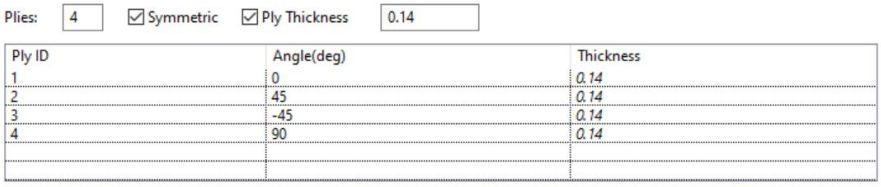
Plies: 4 Symmetric Ply Thickness 0.14

Ply ID	Angle(deg)	Thickness
1	0	0.14
2	45	0.14
3	-45	0.14
4	90	0.14

Figure 3.6. Quasi-isotropic lay-up definition in MD Linear Material Characterization step. [Source: Multiscale Designer]

The result obtained from running the Linear Material Characterization is the macro homogenized material properties and the homogenized material matrix. These are provided for only one UD ply (RVE_fm material model) and for the associated laminate lay-up (RVE_fmLAM material model) previously defined (8-plies quasi-isotropic).

Finally, MD also allows to specify one or several micro-phases to remain elastic throughout the non-linear analysis. This is useful when the material behaviour can be assumed to have a very small plastic part. Typically, this occurs in materials that are very brittle. Thus, the final failure and damage onset can be adjusted rather close to each other. For instance, this assumption could be made in the current work, as the final failure of the CFRP material used is the end point of the linear region.

Additionally, in order to run the Non-linear Material Characterization step, MD requires to specify one or more of the built-in Macro Simulation Models (based on displacement control) available in the MD library. The list of simulation tests available are: Unnotched Tension/Compression

(UNT/C), Load/Unload, three-point Bending, four-point Bending, Open Hole Tension/Compression (OHT/C), Rail Shear and Dogbone. Although the computation of the Non-Linear Characterization requires to choose one of the previous simulations, the non-linear material model obtained is independent of the simulation test chosen and, it can be used as material model for any other non-standarized/non-conventional simulation.

The Non-Linear Material Characterization introduces two main challenges. The first one is the difficulty in determining the experimental values for all damage model constants required for each phase. The material values for the damage models, especially for the interphase, are not even available in literature since they cannot be measured with the current technology. The second challenge is that in the end, the result (material model) provided by Altair MD is a combination of many fitted material parameter values rather than valid material properties. Moreover, the fitting method lying on the backend program is not explained in the MD user manual [59]. The practical idea of Altair MD is to add many damage parameters and models, which makes it convenient to run inverse characterization simulations for any test, as the experimental determination of the macro properties is possible with the current technology. However, for the forward homogenization this is not such a convenient approach due to the difficulty in determining the values of all (non-linear) micro properties that need to be defined prior to running the MD simulation.

3.3 Multiscale Routines for Impact Simulations

The current section is divided into two parts. In the first part the modelling of the indentation simulation will be covered, whereas the second part will be dedicated to the modelling of the impact simulation. The indentation is a static test, whereas the impact corresponds to a dynamic test. For the indentation case, the implicit solver OptiStruct will be used, whilst for the impact case the explicit solver RADIOSS will be employed.

3.3.1 Indentation Simulation - OptiStruct

The indentation simulation is a model consisting of a spherical indenter and a circular laminate specimen. This geometry is a simplified model of the real experiment, as it only accounts for the testing area (specimen

and indenter). The dimensions of the real laminate's area are 58.1 $\times$ 58.1 mm. However, the diameter of the hole in the specimen steel support - defining the test area - is 38.1 mm, which is the diameter used for the circular specimen in the model. The thickness of the specimen is 1.12 mm, which corresponds to a ply thickness of 0.14 mm. The indenter is a sphere with a diameter of 12.7 mm. The real experiment consists of 6 load steps, where a quasi-static force is applied in the downward direction by placing the indenter in the center of the specimen. In the subsequent loadings, the force is increased in steps (0, 27.4, 47, 66.6, 86.3, 105.9 N). The same load steps are employed in the simulation and a non-linear static analysis is run for each load step. The non-linear analysis option is taken because of software related reasons, which will be later on commented. For static simulations an implicit solver is used - OptiStruct.

Both the modelling and pre-processing of the indentation are done in HyperMesh from Altair. The specimen's laminate definition can be done in different ways, which will be later compared in Section 4. The first way (shell elements) is to define the specimen as a laminate composed of shell elements using the 'Laminate tool' from Hypermesh. In this case, the material model is set to each unidirectional ply and the corresponding ply orientations are established for the laminate. The second way (solid elements) is to define the specimen as a laminate composed of a 8-layers mesh of solid elements. Each ply of the laminate is modelled by an (layer) element. The orientation of the plies is done by setting the material coordinate system of all the solid elements composing a specific layer, in the desired orientation of each ply. The solid rigid condition is set to the indenter in order to ensure that it behaves as the rigid body in the simulation. In addition, the indenter is considered as the master body, whereas the specimen is the slave for the indenter-specimen contact condition in the load application region.

The specimen is constrained in all 3-translation DoFs by applying single point constraints (SPC) BCs at each of the nodes of the circular edge in the geometric mid-plane of the laminate (element reference plane). The loads are applied as forces with application point in the center of the indenter (sphere's center of mass). A total of 5 different force levels are simulated ranging from 24.7 N up to 105.9 N, as stated in Section 3.5.

The indenter mesh is modelled with quadratic shell elements (CQUAD4) in all simulations. The element types used for the specimen meshes are either first-order shell elements (CQUAD4) and second-order shell elements (CQUAD8), or first-order solid elements (CHEXA 8-node) and second-order solid elements (CHEXA 27-node). Both first- and second-element orders are analyzed one by one and their effect on the results will be compared in Section 4. The specimen in the model only contains one element per ply thickness, i.e. 8 solid elements along the thickness of the laminate. The specimen mesh follows a radial pattern, where the elements' size gets gradually smaller from the edges of the specimen towards the center. The mesh is divided in three main circular regions and the transitions between them are smooth. The specimen central region, where indenter-specimen contact happens, presents a uniform quadractic elements distribution. Fig. 3.7 a) shows the mesh used in the indentation model.

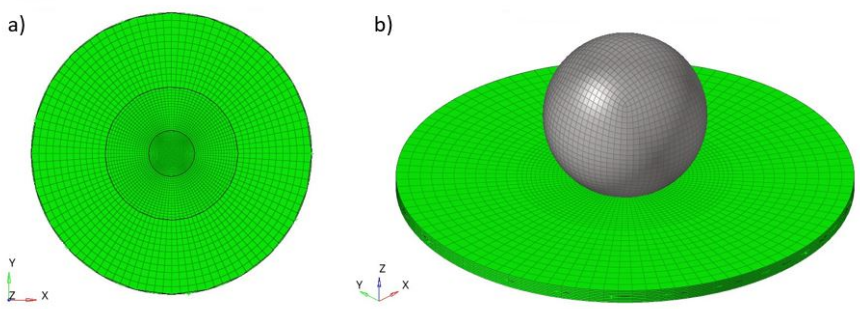

Figure 3.7. Indentation and impact specimen's mesh (a) and FE-model layout (b). [Imaged in HyperMesh]

Fig. 3.7 b) shows the indentation simulation model layout. This specific model corresponds to the case where the laminate is defined by shell elements. However, the appearance in the user interface at bare eye is exactly the same as in the case where solid elements are used. All elements in the model are referenced to the same global coordinate system. This is done to ensure that all elements' local coordinate system, material orientations and element normals are oriented in the same direction.

The Hypermesh version used in the simulations is v2019.1, which includes some particularities to be noted. Moreover, some software limitations have been found in the current version. To start with, although the load case is linear in this case, the analysis type needs to be set up as 'Nonlinear Static' to avoid problems with the contact conditions. By default the thickness of the shell elements is considered in contacts. This will linearize

the closed contacts and if there is a minimun overlapping, the connected area is likely not to be what it should be expected. This problem can be fixed by using a non-linear subcase and zero padding in the contact. To do so, the analysis type is set to 'Non-linear Static', a load collector with card image NLPARM is added (10 number of non-linear increments is specified here) and it is referenced from the analysis subcase. In addition, in the contact property with card image PCONT, the default padding on shell elements is turned off by setting GPAD options to NONE. A coefficient of static friction is set to 0.3 in the PCONT card image. The card image CNTSTB is also needed to get forces balanced until the frictional contact is established. The factor S0 is set to 0.01, which controls how much stabilization is used and it needs to be as low as possible. After the simulation run is completed, the self-generated '*_s1_e.nlm' file needs to be checked to verifiy that the contact stabilization energy is much lower than the strain energy (at least one order of magnitude lower). For CNTSTB, an iterative process needs to be performed. It is suggested to start with S0=0.1 or lower. The stabilization energy needs to be checked after each run until it does not converge. Then, one must go back to the last working value for which convergence is reached. For the case, when second-order elements are used (CQUAD8 and CHEXA 27-node), the discrete flag GAPOFFS needs to be set to YES on the GAPPRM card, in order to avoid problems with the contacts discretization, as covered in section 2.2.4.

It was also found that v2019.1 has convergence problems when a 'small displacements analysis' is selected, whereas v2020.1 seems to improve the convergence. Therefore it is needed to switch to a 'large displacement analysis' when using v2019.1. This is done by referencing the card image NLPARM under NLPARM(LGDISP) option in the analysis subcase. Besides, v2019 convergence is improved if the indenter is constrained in x-y plane, as the S0 contact stabilization factor can get even lower stabilization energy. According to Altair Customer Support, the reason for the difference between v2019.1 and v2020.1 is that the CNTSTB load collector is not available in v2019.1 load case for small displacements. Altair recommends to use v2020.1 since it provides with a better control of the model stabilization. Otherwise, the selection of large displacement run is required. For the shell elements model in v2020.1, the LGDISPL analysis is not needed. However, for the solid elements model convergence is still not reached unless a LGDISPL analysis is selected.

3.3.2 Impact Simulation - RADIOSS

The impact simulation model employs the same geometry as the indentation model, described in the previous section 3.3.1. Both the impactor and specimen have the same dimensions and characteristics as in the indentation simulation. Notice that the indenter is referred as impactor in the impact simulation. The real experiment consists of 6 load cases as explained in Section 3.5 and shown in Table 3.6, where the impactor is dropped from different heights corresponding to different energy levels and achieving different impact velocities. The impact simulation is performed for the 5 J energy level case. The solver used is RADIOSS, which is the explicit solver from Altair.

Both the modelling and pre-processing of the impact are done in HyperMesh from Altair. The specimen laminate definition is done only for first-order shell elements (SHELL4N) and first-order solid elements (BRICK, also known as HEXA8N). The impactor is also made of steel and the solid rigid condition is set to ensure that it behaves as a rigid body in the simulation. The impactor is again considered as the master body, whereas the specimen keeps being the slave. In this case, the contact condition is stablished by means of the card image TYPE7 for the shell slements model and TYPE25 for the solid elements model. One of the main differences with respect to the implicit simulation is the allocation of the impactor's mass in the explicit simulation. A mass of 2771.9 g is assigned to the rigid body (RBODY card image).

The specimen is constrained in all three translation DoFs by applying fixed BCs (card image BCS _Collector) at each of the nodes of the circular edge in the geometric mid-plane of the laminate. Unlike for the indentation, the load is not applied in the form of a force in the impactor's center of mass, but as an initial velocity of the impactor center of mass (card image INIVEL _Collector). The initial velocity assigned is -1.899 m/s (or mm/ms) in z-axis direction, which corresponds to a drop height of 183.9 mm (energy level 5 J). The drop height is irrelevant in a RADIOSS simulation, as the initial velocity BC is the one defining the impact condition. Therefore, it is not needed to simulate the entire impactor drop trajectory from a height of 183.9 mm until reaching the center of the specimen. It is enough to place the impactor at a small height above the specimen in the model. A gap of

0.2 mm is left between both bodies to avoid elements penetrations.

The mesh style for the impactor and the specimen is the same as the one used for the indentation, as shown in Fig. 3.7 a) and the impact simulation model layout looks identical to the one in Fig. 3.7 b). However, second-order shell elements are not supported in RADIOSS. Only first-order shell elements (SHELL4N) are available in RADIOSS for 3D analysis. Additionally, the equivalent to first-order solid elements (HEXA8N) in RADIOSS are termed as BRICK elements.

The main differences of the modelling in RADIOSS compared to OptiStruct relies on different card images to be used and their complexity. The card images depend on the RADIOSS material law used to described the composite material, in this case the LAW25 is selected. LAW25 is the most commonly used composite material in RADIOSS. It can be used with shell and solid elements. The two formulations available in LAW25 are the Tsai-Wu and CRASURV formulations. To start with, in the shell elements model, the laminate needs to be defined using the card image STACK and selecting the 'Ply Laminate' type. The plies are defined using the card image P19_PLY, setting a layer thickness of 0.14 mm, 3 integration point through the ply thickness and allocating the ply material model by referencing the card M25_COMPSH. The ply material model used in the specimen is input through the card image M25_COMPSH. Apart from the density and the typical 9 engineering constants, other parameters corresponding to the Tsai-Wu Formulation need to be input (non-zero). Such values are stated in Table 4.2 from Chapter 4. On the other hand, the impactor material model (Steel) is set using the card image M1_ELAST.

Concerning the properties, four different property cards are required in the RADIOSS simulation using shell elements. The PCOMPP card needs to be used for the composite laminate definition. The P10_SH_COMP card is to be selected to define the composite's shells properties (number of layers and shell thickness). Alike, P1_SHELL is needed to define the properties of the impactor's shells, where a thickness of 0.1 mm is selected. Finally, card P17_STACK is required to stablish the properties of the laminate. The shell thickness, components of reference vector, skew system, orthotropic system formulation and laminate layout selection, are among the parameters to be defined in P17_STACK card.

If solid elements are used instead, some differences in the modelling appear. To start with, BRICK elements are used instead of SHELL4N. Each ply of the laminate is transformed into a separate component composed of solid elements. This can be done relatively quickly with the 'Composite Shell to Solid Conversion' tool available only in OptiStruct. First, the conversion is run in Hypermesh OptiStruct and, then the Hypermesh profile is changed back to RADIOSS. The material law M25_COMPSH remains the same, but the property of each ply needs to be changed to P6_SOL_ORTH. In P6_SOL_ORTH, $ISOLID$ is set to '14: HA8 locking-free 8-node solid element' and $Ismstr$ is set to 2. Within the same card, the reference coordinate system for the ply material orientation is selected in $Skew_ID$, I_p is set to '0: Use skew_ID' and $Iorth$ is left to '0: Orthonormal co-rotational element coordinate' . Unlike in the shell model, PCOMPP, P19_PLY and P17_STACK are no longer used.

All elements from the RADIOSS models are referenced to the same global coordinate system. This is done to ensure that the local coordinate systems, material orientations and normals of all the elements are oriented in the same direction.

Table 3.1. Control Cards list used for the execution of RADIOSS solver. Notice that some card are specific of shells or solid elements, while others are general.

ENG_RUN	ENG_STOP
ENG_TFILE	ENG_MON
ENG_ANIM_DT	ENG_DT_NODA
ENG_ANIM_SHELL_TENS_STRAIN	ENG_PRINT
ENG_ANIM_SHELL_TENS_STRESS	ENG_VERS
ENG_ANIM_SHELL_EPSP	ENG_ANIM_BRICK
ENG_ANIM_BRICK_TENS_STRAIN	ENG_ANIM_NODA
ENG_ANIM_BRICK_TENS_STRESS	ENG_ANIM_ELEM
ENG_ANIM_BRICK_TENS_EPSP	ENG_ANIM_VECT

The solver in RADIOSS is executed in two steps: the Starter and the Engine. The Starter reads a $Runname\_0000.rad$ file that contains the model definition. The Starter diagnosis possible errors in the models and outputs a binary restart file. The Engine executes the actual computation. It waits for the binary file produced by the Starter and a $Runname\_run\#.rad$ input file in Block Format. The Engine Input describes the case control. The Engine produces output files for animation, plotting (time history) and restart. The engine settings are configured by means of Control Cards. For the correct solver execution, the control cards stated in Table 3.1 are used.

3.4 Material Properties

The CFRP panel studied in the current work is a quasi-isotropic laminate with the lay-up $[0/45/\text{-}45/90]_{\text{SE}}$ and composed by eight As4/3501-6 UD pre-preg plies, which are manufactured by HexPly®. Each ply is formed by carbon/graphite As4 fibres and 3501-6 epoxy matrix. Each pre-preg ply is purely unidirectional (UD) and no weaving is present therein. The lamination scheme followed is [0/45/-45/90] and the pattern is symmetric (even). The fundamentals of a quasi-isotropic laminate have been already discussed and presented in section 2.1.

The mechanical properties of the carbon fibre, epoxy matrix and CFRP UD pre-preg ply employed are taken from both the manufacturing information, as well as from literature. These are stated in the following Tables 3.2, 3.3 and 3.4. Their corresponding reference sources are indicated in each table.

Table 3.2. Mechanical properties values for As4 carbon fibres (transversely isotropic). [Source: [76] and [75]]

Property	**Value**
E_1 [GPa]	231
E_2 [GPa]	14
E_3 [GPa]	14
ν_{12} [-]	0.2
ν_{13} [-]	0.2
ν_{23} [-]	0.3
G_{12} [GPa]	14
G_{13} [GPa]	14
G_{23} [GPa]	5
ρ [g/cm^3]	1.79

Table 3.3. Mechanical properties values for 3501-6 epoxy matrix (isotropic). [Source: [76] and [74]]

Property	**Value**
E [GPa]	4.24
ν [-]	0.37
G [GPa]	1.6
ρ [g/cm^3]	1.265

$$CPT[mm] = \frac{FAW[g/m^2]}{1000 \cdot \rho_f[g/cm^3] \cdot V_f[\%]} \tag{3.3}$$

Table 3.5 contains different material parameters at the micro-level, which are given in the data sheets ([74] & [75]) provided by the manufacturer (HEXCEL) of the HexPly® 3501-6/150/AS4 UD-Prepreg used in the experi-

Table 3.4. Mechanical properties values for one As4/3501-6 UD pre-preg ply. [Source: [77]]

Property	**Value**
E_1 [GPa]	140
E_2 [GPa]	10
E_3 [GPa]	10
ν_{12} [-]	0.3
ν_{13} [-]	0.3
ν_{23} [-]	0.2
G_{12} [GPa]	6
G_{13} [GPa]	5
G_{23} [GPa]	3
V_f [%]	62

Table 3.5. Material parameters for the HexPly® 3501-6/150/AS4 UD-Prepreg. [Source: HEXCEL [74] & [75]]

Parameter Name	**Units**	**Value**
Cured Ply Thickness (CPT)	[mm]	0.14
Fibre Density (ρ_f)	[g/cm^3]	1.79
Fibre Areal Weight (FAW)	[g/m^2]	150
Filament Diameter (d)	[mm]	0.0071
Fibre Radius (r)	[mm]	0.0036
Interphase Thickness (t)	[mm]	0.0002
Int Thick / Fibre Radius (t/r)	[-]	0.056
Resin Ratio Volume (V_r)	[%]	32.45
Fibre Ratio Volume (V_f)	[%]	62
Miscellaneous Ratio Volume (V_{misc})	[%]	5.55

ment. The Cured Ply Thickness (CPT) is calculated according to Equation 3.3. The material parameters in Table 3.5 are of interest in the material model development from the microstructural constituents level, which will be discussed in section 3.2.

3.5 Indentation and Impact Testing Description

An impact experiment on a CFRP specimen was carried out at the Laboratory of Materials Science of TAU using a drop-weight impact tower Type 5 (Rosand), as shown in Fig. 3.8. The specimen employed is rectangular with dimensions of 0.0581 m $\times$ 0.0581 m. The test area is circular with a diameter of ϕ = 38.1 mm. The indenter/impactor has a radius of 10 mm. The displacements on the back side of the CFRP specimen were measured using high-speed cameras (Photron) and a digital image correlation (DIC) was applied with the software DAVIS (LaVision).

Firstly, a static testing (indentation test) was performed by placing the

impactor with a controlled mass on top of the sample surface. In subsequent loadings, the weight was increased in steps (0, 27.4, 47, 66.6, 86.3, 105.9 N).

Secondly, impact testing on a similar CFRP specimen was performed using the same drop weight tower as for the indentation test. The mass of the impactor was 2.7719 kg, which was dropped at different heights corresponding to different energy levels (1, 2, 3, 4, 5, 10 J). Thus different contact velocities were achieved, as shown in Table 3.6.

The test fixture, the impactor head as well as the measurements system were the same in both indentation and impact tests.

Figure 3.8. Drop-weight impact tower Type 5 (Rosand) at the Laboratory of Materials Science of TAU. [Source: Tampere University (TAU)]

Table 3.6. Impact test energy levels, drop heights and estimated impactor velocities at contact.

Energy (J)	Drop Height (m)	Contact Velocity (m/s)
1	0.037	0.849
2	0.074	1.201
3	0.11	1.471
4	0.147	1.699
5	0.184	1.899
10	0.368	2.686

4. Results

4.1 Material modelling and element types considered

In this chapter, the results of the FE simulations corresponding to the indentation and impact tests are presented. The modelling of the material response is done in the linear-elastic regimen. Different material models are generated in MD. These material models with their own input settings can be divided into 4 different groups.

- RVE_fm: Fibre and matrix properties are input at the RVE level, without an interphase. This is the material model for **1 ply** of the laminate calculated by means of the MD approach.
- RVE_fmLAM: Fibre and matrix properties are input at the RVE level, without an interphase. This is the material model for the **laminate** (quasi-isotropic) calculated by means of the MD approach.
- expLAM: A manual material model (engineering constants) based on the laminate's experimental constants. Naturally, the same lay-up (quasi-isotropic) as for RVE_fmLAM is used.
- RVE_inter: The material model with a separate interphase defined in the RVE using the MD approach. Fibre and matrix properties are input at the RVE level with an interphase. This is the material model for the laminate (quasi-isotropic) calculated by means of the MD approach.

The material models in the indentation test are computed over the linear-elastic regimen (see Section 3.2). Their material constants are listed in Table 4.1. Alike, the same material models are computed in the linear-elastic regimen for the impact case. In this second case, the material constants need to include additional parameters belonging to the Tsai-Wu

formulation, as shown in Table 4.2.

Table 4.1. Material constants of RVE_fm (material model for a single ply), RVE_fmLAM (material model for a laminate $[0/45/\text{-}45/90]_{SE}$) and expLAM (i.e. experimental data for an UD ply of the laminate) material models.

Property	**RVE_fm**	**RVE_fmLAM**	**expLAM**
E_{11} [GPa]	140	53.06	140
E_{22} [GPa]	8.73	53.06	10
E_{33} [GPa]	8.73	10.33	10
ν_{12} [-]	0.26	0.31	0.3
ν_{23} [-]	0.44	0.3	0.52
ν_{31} [-]	0.02	0.06	0.02
ρ $[g/mm^3]$	0.001579	0.001579	0.00158
G_{12} [GPa]	4.42	20.31	6
G_{23} [GPa]	3.04	3.61	3
G_{31} [GPa]	4.42	3.61	5

The modelling cases computed using the RVE_fm material model (Tables 4.1 and 4.2) and analyzed in this work are classified as follows:

- FM1: Indentation simulation where each ply is modelled with RVE_fm, one shell element per ply thickness and using first-order elements.
- FM2: Indentation simulation where each ply is modelled with RVE_fm, one shell element per ply thickness and using second-order element elements.
- FM3: Impact simulation where each ply is modelled with RVE_fm, one shell element per ply thickness and using first-order elements.
- FM5: Indentation simulation where each ply is modelled with RVE_fm, one solid element per ply thickness and using first-order elements.
- FM6: Indentation simulation where each ply is modelled with RVE_fm, one solid element per ply thickness and using second-order element elements.
- FM7: Impact simulation where each ply is modelled with RVE_fm, one solid element per ply thickness and using first-order elements.

Table 4.2. Material constants of RVE_fm (material model for a single ply), RVE_fmLAM (material model for a laminate $[0/45/\text{-}45/90]_{SE}$) and expLAM (i.e. experimental data for an UD ply of the laminate) material models for RADIOSS material LAW25 using the Tsai-Wu formulation.

Property	**RVE_fm**	**RVE_fmLAM**	**expLAM**
ρ [g/mm^3]	0.001579	0.001579	0.00158
I_{form}	Standard	Standard	Standard
E_{11} [GPa]	140	53.06	140
E_{22} [GPa]	8.73	53.06	10
E_{33} [GPa]	8.73	10.32	10
ν_{12} [-]	0.26	0.31	0.3
ν_{23} [-]	0.44	0.3	0.52
ν_{31} [-]	0.02	0.06	0.02
G_{12} [GPa]	4.42	20.31	6
G_{23} [GPa]	3.04	3.61	3
G_{31} [GPa]	4.42	3.61	5
ε_{f1} [-]	1.2e+30	1.2e+30	1.2e+30
ε_{f2} [-]	1.2e+30	1.2e+30	1.2e+30
ε_{t1} [-]	1e+30	1e+30	1e+30
ε_{m1} [-]	1.1e+30	1.1e+30	1.1e+30
ε_{t2} [-]	1e+30	1e+30	1e+30
ε_{m2} [-]	1.1e+30	1.1e+30	1.1e+30
d_{max} [-]	0	0	0
W_p^{max} [mJ/mm^3]	1e+30	1e+30	1e+30
W_p^{ref} [mJ/mm^3]	1	1	1
I_{off} [-]	1	1	1
$Ratio$ [-]	1	1	1
b [-]	0	0	0
n [-]	1	1	1
f_{max} [GPa]	1e+27	1e+27	1e+27
σ_{1y}^t [GPa]	1e+27	1e+27	1e+27
σ_{2y}^t [GPa]	1e+27	1e+27	1e+27
σ_{1y}^c [GPa]	1e+27	1e+27	1e+27
σ_{2y}^c [GPa]	1e+27	1e+27	1e+27
α [-]	1		
σ_{12y}^c [GPa]	1e+27	1e+27	1e+27
σ_{12y}^t [GPa]	1e+27	1e+27	1e+27
c [-]	0	0	0
ε_0 [1/ms]	1	1	1
ICC [-]	1	1	1
γ_{ini} [-]	1e+30	1e+30	1e+30
γ_{max} [-]	1.1e+30	1.1e+30	1.1e+30
d_{3max} [-]	1	1	1
F_{smooth} [-]	0	0	0
F_{cut} [Hz]	1e+30	1e+30	1e+30

4.2 Force-displacement curves for indentation

Fig. 4.2 shows the comparison in the linear regime of force-displacement curves between the shell elements simulation (FM1), the solid elements simulation (FM5) and the experimental data (indentation). The displacement values have been taken from central node of the specimen, where the indenter-laminate contact occurs. The force measured is the reaction force caused by the indenter. In all three cases the curve is linear and the difference between them is not significant. The (regression) coefficient of determination (R^2) between the experimental data and simulations is 0.99. Therefore, the simulation and experimental curves match, which indicates that the responses obtained could be rigorously compared.

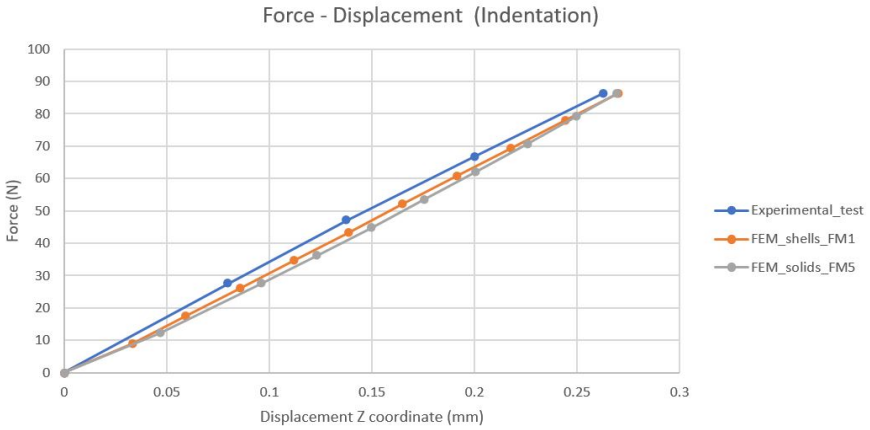

Figure 4.1. Force-displacement curves for indentation experimental test, shell elements simulation (FM1) and solid elements simulation (FM5). R^2 = 0.99

4.3 Deformation profile (cross-section) over the CFRP specimen during indentation

This comparison is mainly focused on the local transfer of bending and shear (in xz and yz plane), which are mainly reflected by the z-displacement in the DIC data.

The z-displacements field results of the simulation cases stated in Section 4.1 allow to study the effect of both the element type and element order in the indentation (static) case. The z-displacements nodal values are taken along two orthogonal lines passing through the center of the specimen (x- and y- axis directions). The nodes selected correspond to the bottom part of the bottom ply in the laminate. All simulation and experimental values are taken/measured from the same location.

The indentation models results follow the same nomenclature as earlier introduced (see Section 4.1): FM1, FM2, FM5 and FM6.

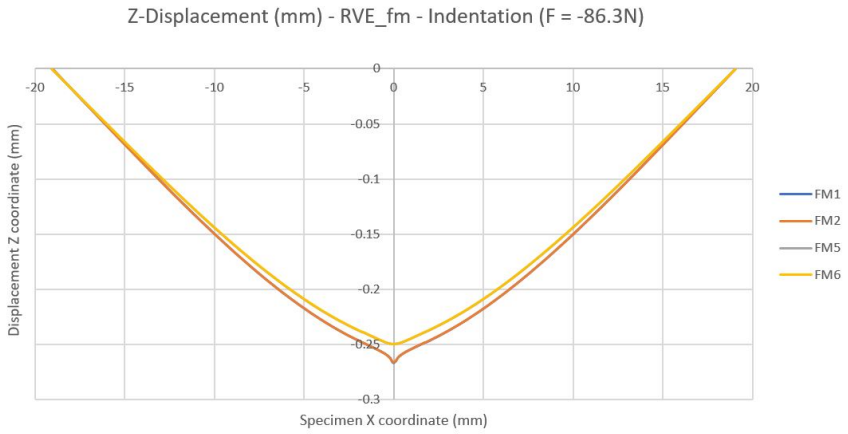

Figure 4.2. Deformation profile (Z-displacements) along the orthogonal horizontal line (specimen x-axis) for the indentation models using RVE_fm material model.

The displacement curves from Fig. 4.2 prove that the element order does not have a relevant impact in the accuracy of the results for this specific indentation simulation case. The curve FM1, which uses first-order elements overlaps with curve FM2 (with second-order elements). This is why the blue color is not visible, as the orange curve is right upon it. The same happens with curves FM2 and FM6, where the yellow curve is completely covering the grey one. FM2 employs first-order elements and it is overlapping with FM6, which uses second-order elements. If these differences are measured quantitatively, the error between FM1/FM2 and FM5/FM6 is in both cases between 0% and 0.1%, which confirms the behaviour observed in the curves.

Regarding to the type of element used in the models, the displacement curve shows that the element type chosen has a significant effect on the results, especially at the loading point by the indenter (Fig. 4.2). This effect is especially visible in the central region of the specimen, where the contact zone between the indenter and the specimen is located. In the range [-10, 10] mm along the x-coordinate, curves FM1 and FM2 start to differ from curves FM5 and FM6. The gap between curves increases, as the central point (x = 0 mm) of the specimen is reached. FM1 and FM2 curves correspond to models using the shell elements, whereas FM5 and FM6 curves employ the solid elements. The difference betwen the curves starts to be around 4% at the edges of the range [-5, 5] mm. Near the central

point of the specimen, the solid elements provide with a smoother solution, whereas the shell elements show a small tilt at the centre point. This is due the inherent problem that shells do not have out-of-plane response and, therefore they cannot simulate the loading exactly at the center properly. Shells work only after there is enough bending deformation in elements and finally membrane loading in the entire laminate model for impact. However, the shell elements are usually preferred for the modelling of composite laminates since they work well at a general level and, they are less computationally expensive. The computational time-saving is due to the reduction in spatial dimension of finite elements and, consequently the equations to be solved.

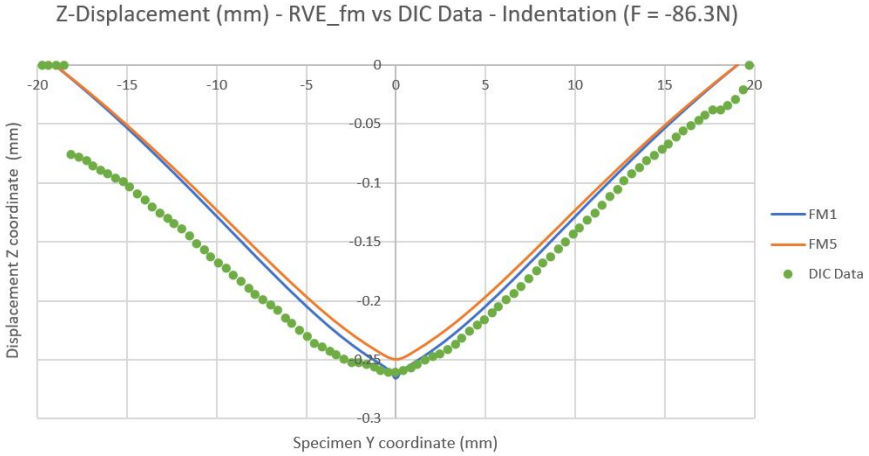

Figure 4.3. Comparison between RVE_fm indentation models and DIC displacement data obtained experimentally (R^2 = 0.98). The deformation profile is taken along the orthogonal y-axis of the specimen.

Fig. 4.3 shows the comparison between the experimentally measured results (indentation DIC data) and FE-results of curves FM1 and FM5. The experimental results have been measured by means of DIC along the orthogonal y-axis of the specimen. The reason for selecting this profile is that the DIC data along the x-axis presented a higher regression error (R^2 = 0.97, when a four-order polynomial is used for the fitting). The regression error is due to the processing of the data, which is obtained from an image in the DIC procedure. The DIC data profile along the y-axis has a slightly smaller regression error (R^2 = 0.98). It can be seen that the DIC data curve seems to follow the same shape as the FM1 and FM5 results. This is particulary similar on the right-hand side of the profile, i.e. range [0, 20] mm. In the central region the differences between the DIC data and FEM curves are of around 4% higher for the experimental values. This is normal as FE typically tends to provide a stiffer behaviour. The deviation of the DIC curve from FM1 and FM5 on the range range [-20, 0] mm is due

to DIC data processing inaccuracies, non-central impact, and asymmetry in the laminate in reality.

The homogenized material model generated in MD after inputting the fibre and matrix properties at the RVE level (without interphase) is named as RVE_fmLAM (Table 4.1). This material model is defined for the entire laminate (quasi-isotropic), i.e. it includes the lay-up homogenization. The effect of the lay-up computation (multi-scale homogenization) in MD can be studied from the comparison between the two most different RVE_fm cases (FM1 and FM5) and, the same cases using RVE_fmLAM (see Fig. 4.4). The indentation modelling cases computed using the RVE_fmLAM material model are referred as FM1_fmLAM and FM5_fmLAM.

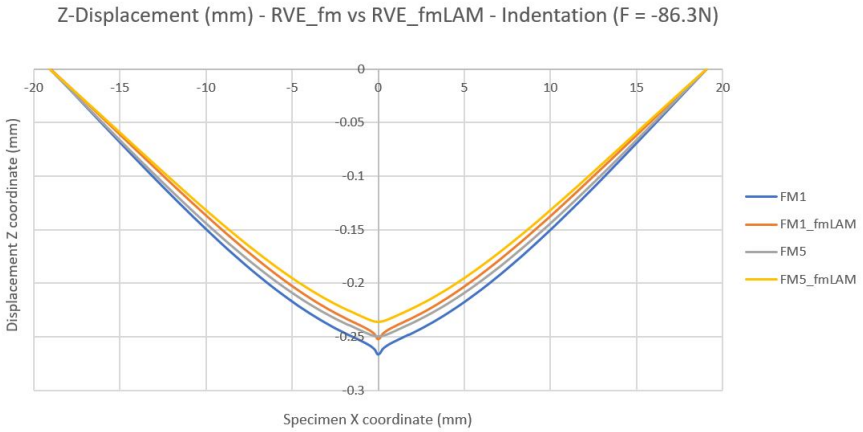

Figure 4.4. Deformation profile comparison between RVE_fm (for single ply) indentation models and the same models using the homogenized material model RVE_fmLAM (for the laminate).

As shown in Fig. 4.4, the MD laminate material model (RVE_fmLAM) affects the modelling results, providing a stiffer solution. In the central region [-10, 10] mm a higher-stiffness solution is obtained. The displacement values differences in this region vary from 5% to 8%, between the homogenized model solution for the whole laminate (RVE_fmLAM) and the homogenized solution for a model that incorporates a material model for single ply (RVE_fm), i.e. plies modelled separately in the specimen. The deviations between FM1-FM1_fmLAM and FM5-FM5_fmLAM remain the same, i.e. FM1 undergoes higher displacements than FM5 because of using the shell elements instead of the solid elements, as discussed earlier. However, the RVE_fmLAM material model has the same effect in both cases. Therefore, the MD laminate material model homogenization (of lay-up) does not seem to be as accurate as when modelling the composite properties ply-by-ply (RVE_fm).

The modelling cases FM1 and FM5 are now computed using a laminate defined by the experimental material properties from the literature (expLAM for single ply). These are compared to the results using the homogenized material model (RVE_fmLAM). The expLAM material model (Table 4.1) is also input for the entire laminate and it corresponds to the same lay-up (quasi-isotropic) with the experimental material constants. The comparison of the displacements field is shown in Fig. 4.5.

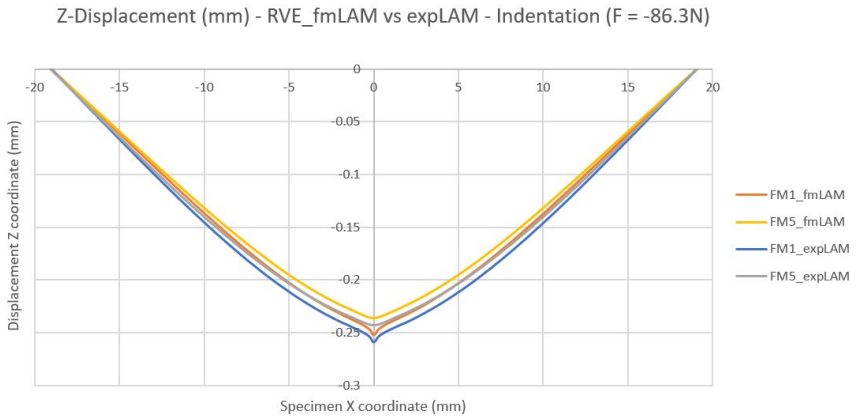

Figure 4.5. Deformation profile comparison between RVE_fm indentation models and the same models using experimental laminate properties (expLAM).

The expLAM material model provides with a less stiff solution than the laminate homogenized material model (RVE_fmLAM). Indeed, it shows results closer to the RVE_fm models from Fig. 4.4. However, the differences observed in Fig. 4.5 between expLAM and RVE_fmLAM lie under 4% in the central region [-10, 10] mm. Thefore, the experimental properties used in expLAM seem to well-characterize the quasi-isotropic laminate used in this work.

The strains field in the xy plane obtained from RVE_fmLAM results is compared to the DIC-based in-plane strain data. The ε_{xx} and ε_{yy} values are taken from the bottom part of the bottom ply in both the FE-model and experiments (indentation). The strain fields represent the in-plane spatial distribution of deformation. Fig. 4.6 and Fig. 4.8 show the shape and asymmetry of the deformation over the entire specimen, its bottom ply in details, xy plane.

Fig. 4.6 shows the whole ε_{xx} field from the bottom ply of the specimen (Ply#1 in FEM). On the left hand-side it can be seen the FE-result corresponding to the FM1_fmLAM simulation. The image on the right-hand

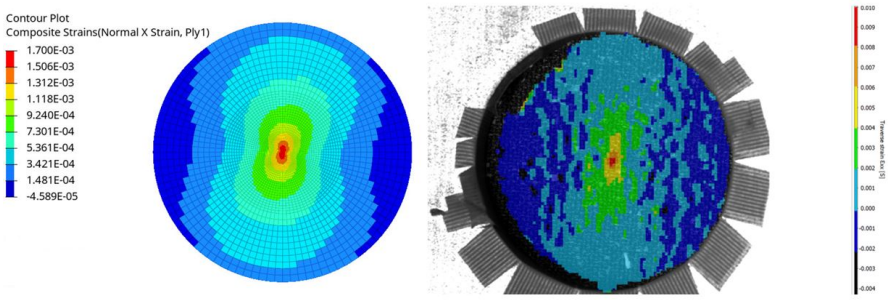

Figure 4.6. In-plane spatial distribution of deformation (ε_{xx}) contours comparison between RVE_fmLAM indentation model and DIC data. The images shown correspond to the bottom ply of the specimen.

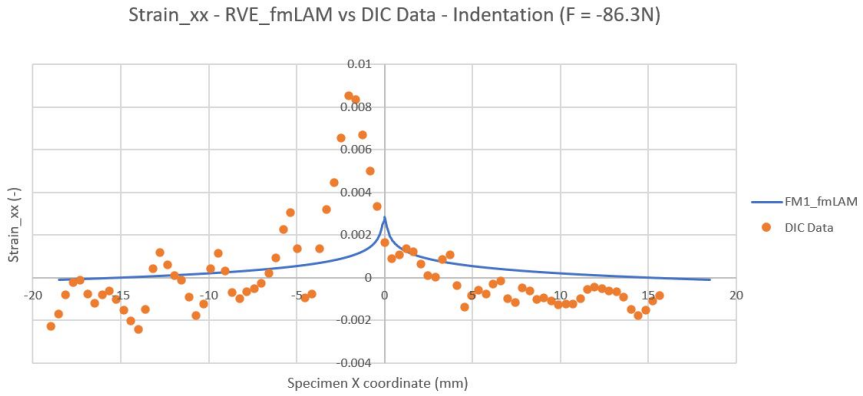

Figure 4.7. ε_{xx} comparison between RVE_fmLAM indentation model and the DIC strain data (R^2 = 0.45).

side corresponds to the DIC data and its field representation. On the other hand, Fig. 4.7 shows the comparison of ε_{xx} along the x-axis direction of the specimen. Both curves increase towards the center of the specimen, however the differences are important. From the edges of the specimen until the beginning of the central region [-5, 5] mm, the DIC data curve shows a lot of fluctuations in the values (R^2 = 0.45) . This is most likely due to inaccuracies in the experimental measuring or, caused by the fact that the entire deflection range in Fig. 4.3 is less than 250 microns, whereas the laminate surface has (thickness) variations in the order of 50-100 microns, which may imply to local stiffness changes too. This would also be affecting the DIC strain results measured. Also, it is typical that groups or bundles of filaments on the ply surface behave slightly differently - leading to slight deformation undulations on the free surface. On the other hand, the solution from the FE-model presents a smoother and more constant increase from the edges towards the center. In the region [-5, 5] mm the differences triples, particularly at the maximun displacement point. It is to remark that both ε_{xx} and ε_{yy} (see also, Fig. 4.9) for the DIC data show their highest strain peak at x = -2 mm, whereas the FE-solution has it at x

= 0 mm. This indication shows that the real impact did not occur exactly in the central point of the laminate (test area).

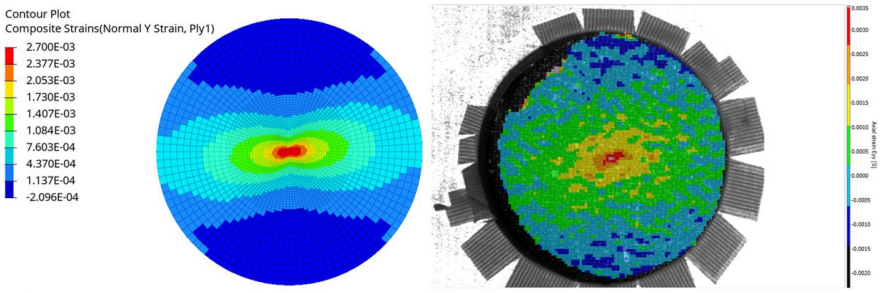

Figure 4.8. In-plane spatial distribution of deformation (ε_{yy}) contours comparison between RVE_fmLAM indentation model and DIC data. The images shown correspond to the bottom ply of the specimen.

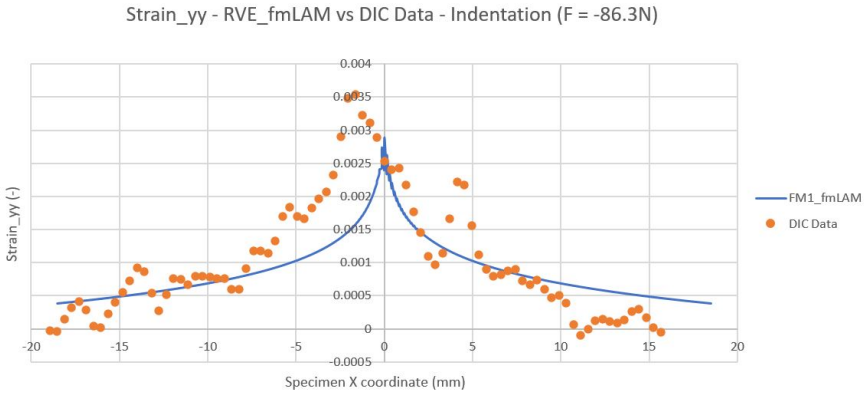

Figure 4.9. ε_{yy} comparison between RVE_fmLAM indentation model and the DIC strain data (R^2 = 0.76).

Fig. 4.8 shows the whole ε_{yy} field from the bottom ply (Ply#1 in FEM) of the specimen. On the left-hand side it can be seen the FE-result corresponding to FM1_fmLAM simulation. The image on the right-hand side corresponds to the DIC data. Fig. 4.9 shows the comparison of ε_{yy} along the x-axis direction of the specimen. In this case, the model and the DIC strains are closer to each other. Fluctuations are still present in the DIC data curve (R^2 = 0.76), although their amplitudes are smaller than for ε_{xx} as could be expected based on the unidirectional fibres in the (bottom) ply. The ε_{yy} increases towards the center of the specimen and the difference between the maximun peaks of both curves is around 5%.

The strains on the surface mostly reflect the in-plane load transfer at this point of loading (minor bending). The exact in-plane loads are dependent on the BCs, which is not highly accurate modelled since the BCs are set slightly differently than in the experimental test (indentation). In the

real test, the specimen is restricted by two 'external rings' on top and bottom of the specimen, which may unavoidably allow slight movement of the specimen edges in the xy plane (frictional sliding). Conversely, in the FE-model the BCs are applied in the circular edge of the specimen, which fully restricts any slight movement in xy plane. The design of BCs used in this work clearly restricts the nodes of the circular edges, which seems to be making the model stiffer. This would explain the somewhat low strain values obtained.

4.4 Interphase effect on RVE linear regime for indentation

MD allows to define a third phase at the RVE level, the fibre-matrix interphase. This has not been considered in the previous material models analysed, as stated earlier (see Section 4.1). In order to study the effect of the interphase in the macro-scale behaviour of the composite, an additional material model is used RVE_inter, as mentioned in Section 4.1. This material model generated using MD approach includes the definition of the interphase. The new 'Honeycomb' RVE employed (Fig. 4.10), contains a 6.89% volume of interphase (red phase in Fig. 4.10). The matrix volume is reduced to a 33.25%, whereas the fibre volume remains the same, 59.86%. The number of elements used in the mesh of the three-phase parametric unit cell increases up to 77310. The element type used is still tetrahedral (C3D10). The RVE input parameters are exactly the same as for the RVE without interphase (see Section 3.2). However, in this case an additional parameter needs to be defined, the Interphase Thickness / Fibre Radius ratio (t/r). All parameter values used in the RVE definition are stated in Table 3.5.

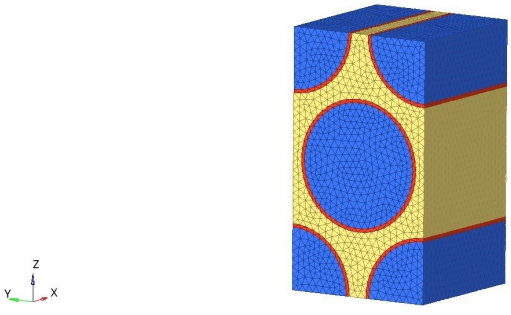

Figure 4.10. Mesh of the generated parametric unit cell (RVE) with three phases (fibre, matrix and interphase). [Created in Multiscale Designer]

In the Linear Material Characterizatiom step of MD, the fibre and matrix are defined exactly the same as in the RVE without interphase. The

interphase is considered as an homogeneous, isotropic and linear elastic phase, based on a work in the current literature [78]. The interphase properties are defined using the same properties as the matrix (see Table 3.3), but varying the Young's Modulus. Two models are created: one with a 80% of the matrix Young's modulus (3.39 GPa) and a second one with a 60% of the matrix Young's mudulus (2.54 GPa). These RVE_inter material models are compared to the RVE_fmLAM (without interphase) in the FM5 indentation simulation. The deformation profiles obtained are shown in Fig. 4.11.

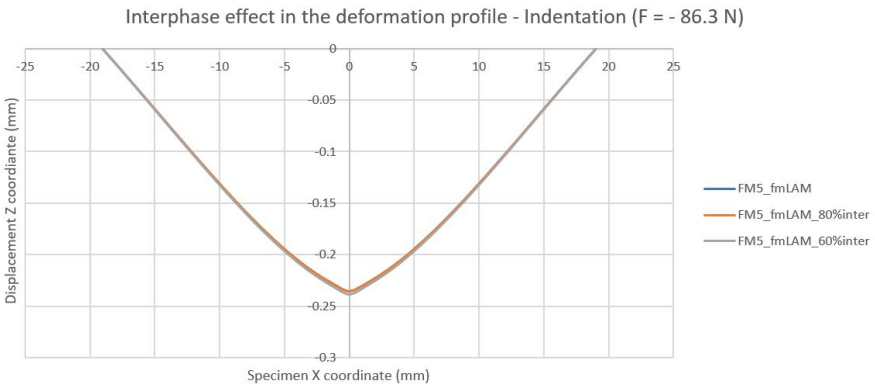

Figure 4.11. Deformation profile comparison for the FM5 indentation model, when using a material model with (RVE_fmLAM) and without (RVE_inter) interphase definition. Two RVE_inter models are employed (80% and 60% of matrix Young's modulus).

The deformation profiles obtained are almost identical. FM5_fmLAM and FM5_fmLAM_80%inter curves are clearly overlapping. That is why, only the orange curve can be seen in Fig. 4.11. On the other hand, when comparing the FM5_fmLAM to the FM5_fmLAM_60%inter (grey curve), a slight difference of 1.1% higher deformation for the FM5_fmLAM_60%inter is found. This behaviour is expected, as the material model with only 60% of Young's Modulus should reduce the stiffness of the laminate, thus it would undergo a higher deformation. In any case, the RVE interphase definition has not a significant effect on the macro-scale deformation behaviour for this indentation case. The underlying reason is that the interphase stiffness variations do not cause a significant change of the overall material model constants after the multi-scale homogenization has been computed. Most likely, this is due to the relative small volume (6.89%) occupied by the interphase in the RVE, when compared to the fibre or matrix volumes. As it is the least predominant phase in the RVE, its impact on the homogenization is at a minimun. This can be seen in Table 4.3, where a slight reduction of Young's and shear moduli is achieved, as the interphase stiffness is reduced. However, the difference between the RVE_fmLAM and

FM5_fmLAM_80%inter is 0.4%, whereas in the FM5_fmLAM_60%inter it only increases up to 0.6% (compared to the model without interphase). Therefore, such small reductions are expected not to cause important variations in the overall laminate stiffness. The same happens with the rest of elastic constants shown in Table 4.3.

Table 4.3. Laminate material elastic constants obtained through the multi-scale homogenization process, both without and with interphase.

Property	**RVE_fmLAM**	**fmLAM_80%inter**	**fmLAM_60%inter**
E_{11} [GPa]	53.06	52.84	52.53
E_{22} [GPa]	53.06	52.84	52.53
E_{33} [GPa]	10.33	10.09	9.75
ν_{12} [-]	0.31	0.31	0.31
ν_{23} [-]	0.3	0.31	0.31
ν_{31} [-]	0.06	0.06	0.06
G_{12} [GPa]	20.31	20.22	20.07
G_{23} [GPa]	3.61	3.5	3.34
G_{31} [GPa]	3.61	3.5	3.34

It can be concluded that not considering the interphase in the previous section's MD material models was a feasible decision for this study, as the interphase properties variation does not affect the overall results. Besides, computational time savings are achieved since modelling the interphase increases the mesh density by a factor of 10.

4.5 Force-displacement curves for impact case

As with the indentation, the results comparison is focused on the local transfer of bending and shear (in xz and yz plane), which are mainly reflected by the z-displacement in the DIC data. The impact case brings the inertia (low in the current study case). Because of this, first the reaction force-time curves for the impactor are studied and later the z-displacement distributions.

Fig. 4.12 shows the comparison in the linear regime of force-displacement curves in the time range [0, 0.8] ms between the shell elements simulation (FM3), the solid elements simulation (FM7) and the experimental data (impact test). The specific time range [0, 0.8] ms has been taken to ensure the linear regime, as the material models used in the FE-simulations are completely linear. In addition, they do not account for any damage or degradation effects, whereas the real specimen's composite suffers damage initiation from already early stages of the impact test. The displacement values have been taken from the central node of the specimen, where

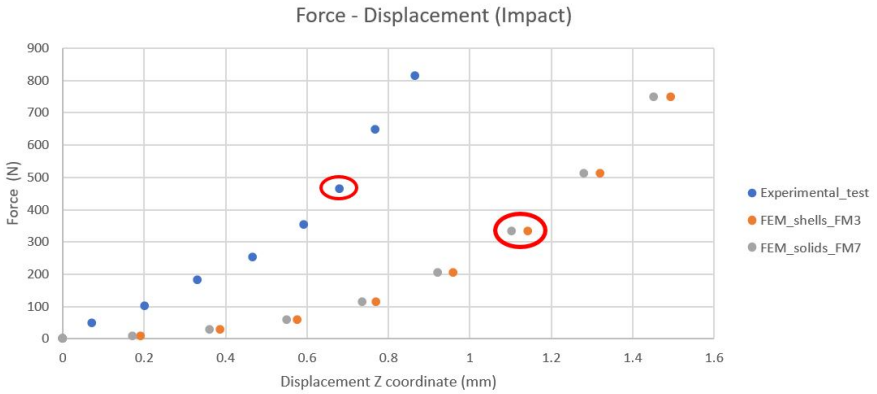

Figure 4.12. Force-displacement curves for impact experimental test, shell elements simulation (FM3) and solid elements simulation (FM7). Marked in red those data points corresponding to T=0.6 ms. R^2 = 0.84...0.92

the impactor-laminate contact occurs. The force measured is the reaction force caused by the impactor. The data points marked with a red circle in Fig. 4.12 correspond to the time-step T=0.6 ms. This will be the time-step at which the deformation profiles will be studied in the next Section 4.6. In all the three cases the curve tends to be essentially linear up to T=0.6 ms, however the regression error varies depending on the case. Both the shell and solid elements simulation curves present an R^2 = 0.84, whereas the experimental curve has an R^2 = 0.92. The R^2 values are calculated based on ideal straight (linear) line. For the same value of force the FE-simulations provide with higher deflection than the experiments (impact test), which means that the laminate of the experiment is stiffer than the one modelled in the simulations, or the force is not collected similarly from FEM and experiments (impact test). The opposite trend would have been expected since FE-results usually tend to be stiffer than reality. On the other hand, the solid elements simulation is still stiffer than the shells elements simulation. Such behaviour from solid elements would be expected, as they seem to capture better the bending loads than shells, as proven in the indentation results (see Section 4.3). Therefore, by looking at the force-deformation curves one would expect that the deformation profiles over the specimen cross-section during impact will be greater for the FE-models than for the DIC data, in this work. Finally, it can be concluded that the impact FE-model does not exactly represent the way force data is measured in reality (in the experiment the load cell/washer is located inside the impactor).

4.6 Deformation profile (cross-section) over the CFRP specimen during impact

The deformation profiles obtained from FM3 and FM7 impact simulations at the time-step T=0.6 ms (as marked in read in Fig. Fig. 4.12) are compared to the DIC data in Fig. 4.13. FEM data points present a R^2 = 0.99 based on a six-order polynomial fitting, whereas DIC data points have an R^2 = 0.98 based on the same order polynomial regression. The comparison shows that the shell elements model (FM3) provides with the stiffest reponse. The displacements obtained in the shells model is around 18% higher than those deformations in the DIC data. This may be due to the fact that shells are bad predicting the out-of-plane type of loading and they cannot carry well loads before membrane load grows enough or elements bend enough. The solid elements model (FM7) still shows a stiffer behaviour than the DIC data, as already expected from Section 4.5. However, the FM7 shows a closer response to that of the DIC Data. In this case, the differences at the center of the specimen reduce down to a 12%. It can be also observed from Fig. 4.13 that the behaviour predicted by the shells and solid elements near the edges of the specimen matches well with the real specimen behaviour. The deflection profile shows that at the edge of specimen for both the shell and solid, tangents are normal to the fictituous wall/specimen support, which matches with the experimental situation.

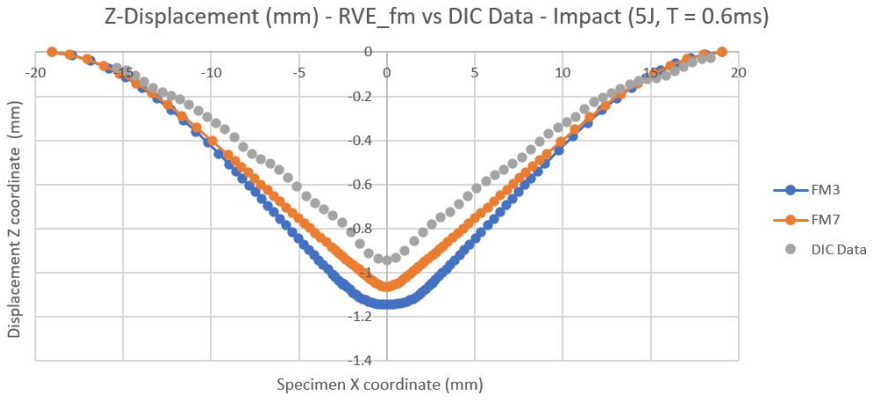

Figure 4.13. Comparison between RVE_fm impact models and DIC displacement data obtained experimentally. The deformation profile is taken along the orthogonal x-axis of the specimen. R^2 = 0.98...0.99

The effect of the MD lay-up computation (multi-scale homogenization) in the impact simulation can be studied from the comparison between the RVE_fm cases (FM3 and FM7) and the same cases using RVE_fmLAM (see Fig 4.14). The differences between the MD material model for single

ply and the MD material model for the whole laminate do not seem to be significant in any of the impact simulation cases. The FM3 (in blue) and FM3_fmLAM curves (in orange) overlap, as well as they do the FM7 (in grey) and FM7_fmLAM curves (in yellow). Therefore, the type of MD material model lay-up computation does not affect the results for this impact simulation case, as observed in Fig. 4.14. Inertial effects, material degradation and element type play a more relevant role in the macro-behaviour of the (real) impact simulation.

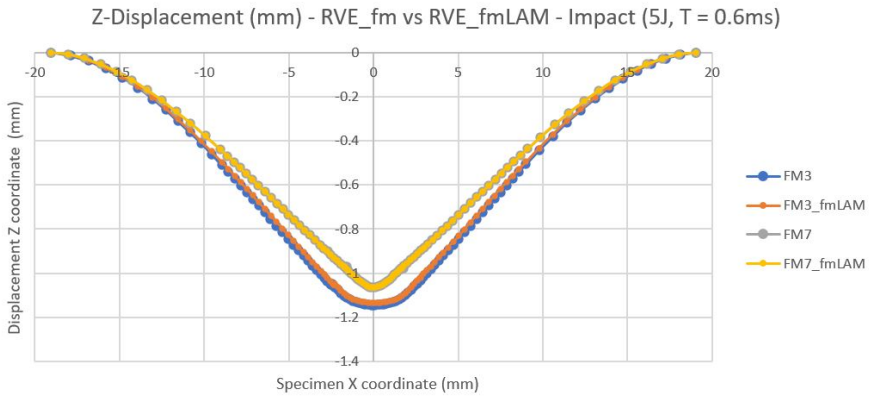

Figure 4.14. Deformation profile comparison between RVE_fm (for 1 ply) impact models and the same models using the homogenized material model RVE_fmLAM (for the laminate).

The modelling cases FM3 and FM7 are computed using a laminate defined by the experimental material properties (expLAM for single ply), see Table 4.2. These are compared to the results using the homogenized material model for the whole laminate (RVE_fmLAM). The expLAM material properties (Table 4.2) belong to a UD-ply, although a quasi-isotropic laminate is modelled by orienting the UD-plies accordingly. The comparison of the displacements field is shown in Fig. 4.15.

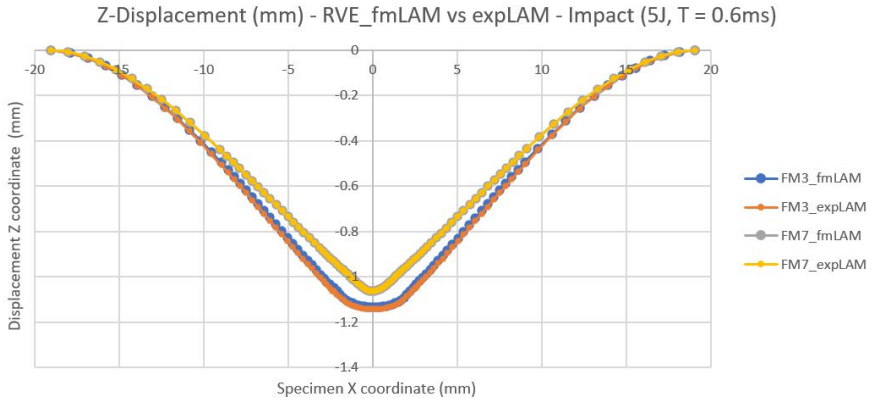

Figure 4.15. Deformation profile comparison between RVE_fm impact models and the same models using experimental laminate properties (expLAM).

As it also happened with the comparison between RVE_fm and RVE_fmLAM

(Fig. 4.14), the expLAM material model does not generate any differences in the deformation profile (Fig. 4.15). The slight varition of the material constants with respect to the RVE_fmLAM is not significant enough to cause major changes in the macro-scale behaviour of the FE-model.

Hence, the different MD material models used have been proven not to affect the results of the impact simulation. The impact simulation behaviour seems to be more influenced by factors such as the element type, the BCs employed, the material degradation effects and the lack of material damage in the current modelling.

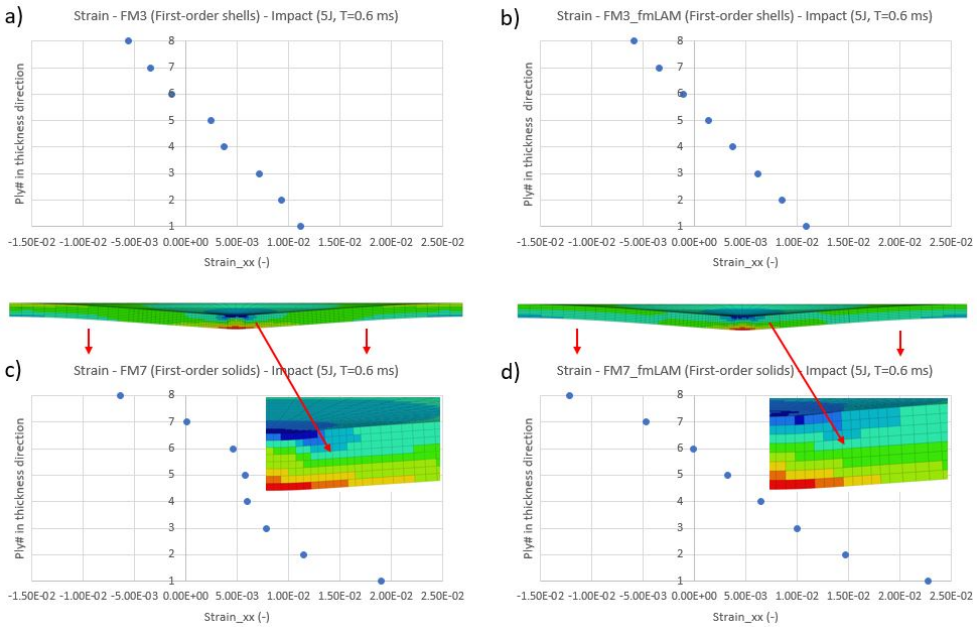

Figure 4.16. Strain ε_{xx} distributions in thickness direction of the specimen's zx plane for the impact simulations. The data points are measured for each ply at a distance of 2 mm from the specimen's central axis (x = 0 mm) and at T = 0.6 ms load.

Fig. 4.16 a) shows the strain distribution in the shell elements model (FM3) for single ply material model (RVE_fm). Fig. 4.16 b) corresponds also to shell elements (FM3), but with the homogenized laminate model (RVE_fmLAM). Fig. 4.16 c) corresponds to the solid elements model (FM7) for single ply material model (RVE_fm). Fig. 4.16 d) also belongs to solid elements (FM7), but with the homogenized laminate model (RVE_fmLAM). From the strain distributions it can be seen that there is both membrane stress and bending stress since zero-stress is not located in the middle of the laminate. For the RVE_fmLAM material model the strain distributions are a bit better since they are "continuous". The distributions corresponding to RVE_fm have some added stiffness in the middle, as the middle data points have similar value to each other.

5. Discussion

In the simulation cases of this thesis for an aerospace grade CFRP laminate, the element order has been found not to affect the accuracy of the simulation results. Therefore first-order elements are enough to model the laminate, as they reduce the number of nodes and, consequently the computational time. On the other hand, the element type has been proven to have a significant effect on the modelling results. The solid elements provided with smoother solutions than shell elements. Shell elements cannot properly predict the out-of-plane response exactly at the point of impact/indentation, as they do not work well until there is enough bending deformation or, there is membrane loading in the entire laminate. The FE-models using solid elements provided a stiffer response than the experimental data in the indentation, whereas shells were shown to be closer to experiments (indentation).

The multi-scale homogenization performed for single ply has proven to behave differently than that performed for the entire laminate, in the indentation case. When the homogenization was performed to the whole laminate, the material became overall stiffer. Thus, the laminate deformation profile obtained was smaller than when defining the material ply-by-ply. The homogenized material model for the laminate produced values between 5% to 8% stiffer than those of the ply-by-ply definition model. The expLAM material model, which used the experimental laminate properties, provided with a solution close to the laminate homogenization model (RVE_fm). Overall, the experimental properties used in expLAM characterized the quasi-isotropic laminate well.

Regarding the strain field the trend is essential and the FE-strain field results obtained follow the same trend as the DIC data curves. Besides,

the behavior near the impactor point has been found to be inaccurate.

The effect of the interphase in the macro-scale results of the indentation is not significant over the linear-elastic regime, for interphase volumes of 6.89%. Hence, for the purpose of this study case it is not necessary to model the interphase at the RVE, despite of MD offering that possibility. However, this may be of interest in study cases where the interphase effect plays a major role on the macroscopic results, such as damage processes and visco-elastic dissipation.

The impact-simulating FE-model did not exactly represent the way force data was measured in reality (in the drop-weight experiment). The force data mismatch between the experiments (impact test) and simulations in the impact case must be caused by the wrong collection of point force data in the FE-model. This is so, because for deformations the specimen model behaves as the real one, i.e. the stiffness of the laminate is correct. In the FE-models the point data force is taken from the impactor-specimen contact, whereas in the real impactor the load cell/washer is inside the impactor. Its data depends partly on the elasticity of the impactor and the stress wave proceeding through the impactor head (to the load cell/washer). Thus, in reality part of the impactor energy is stored above the data collection point and part below. Besides, the impact case results have shown that the differences in the MD material models used do not have a relevant effect. It can be withdrawn that factors such as the element type, the BCs employed, the material degradation and the lack of a material damage models in the current modelling can have a greater influence in the impact simulation results - especially for the further phases of impact events.

Non-linear damage models should be considered in future studies to 'improve' the results of the impact simulation. For this purpose, the Non-linear Material Characterization step should be computed in MD. Thus, the homogenized material model would include both a linear and non-linear part, which could better characterize the real behaviour of the laminate during the impact. Damage models available in MD, which could be proposed for the multi-scale modelling are: a Bilinear Damage Evolution for the fibre phase and a Rate-independent plasticity model for the matrix. The strain-rate dependency is low at 5J energy level impact case, whereby a strain rate-dependent model should not be required to properly predict

the laminate behaviour on the scale of the entire laminate. Additionally, the Isotropic Damage and Plasticity damage model available in MD may be tried, which models both the brittle and ductile behaviour by including damage (brittle behaviour) and plasticity (ductile behaviour) causing a non-linear (inelastic) behaviour of the material.

Including non-linear material models would bring challenges in terms of determining the damage model parameters, which are usually not available in literature for each a specific material and they are difficult to measure experimentally. For that, the inverse characterization tool offered in MD by Altair would be worth to try. This would provide with the non-linear model parameters needed by inputing macro-scale experimental values, which are to be measured with an standarized test on the specific composite in the lab. If a good material modelling is accomplished, going into the failure analysis and damage propagation study would be the following step to this work. The Altair package seems to include powerful tools for a in-depth failure analysis of composite laminates.

Finally, in this work a periodic fibre distribution in the microstructure has been assumed. Yet, MD offers the possibility to account for a random fibre distribution in the RVE by means of the non-deterministic approach. This stochastic approach, which is based on the Monte Carlo method, provides with a Probability Distribution Function (PDF) and Cumulative Density Function (CDF) plot of each property of the Unit Cell and each defined laminate that is generated in the multi-scale process.

6. Conclusions

Nowadays, multi-scale modelling has proven to be a reliable approach to generate composite material models, which predict appropriately the behaviour of the real composite at a macro-scale level simulation. In this thesis, this has been especially clear for the case of the indentation. The homogenized material model for single ply describes better the composite behaviour than using a homogenized material for the complete laminate. This is due to the fact that when homogenizing the entire laminate, the information of the stiffness constants is somehow simplified during the process. The homogenization process generally tends to increase the overall stiffness of the macro-scale model. This process unifies the stiffness values throughout the laminate, but in return some precision is lost in each ply. As a result, the anisotropic nature of the composite is partly lost, compared to the homogenized material only per single ply. On the other hand, the homogenized laminate would allow to reduce the computational cost of macro-scale FE-model since the different plies are not required to be modelled separately (the whole laminate can be model as a one bulk). Furthermore, MD has proven to be a useful tool to create material models based on the properties of the composite micro-constituents. Although the interphase in this study was not found to play a major role in the macro-scale results of the specific study case, MD allows to define the fibre and matrix properties already at the RVE level. Finally, the MD models have turned out not to affect the macro-scale results in the impact case in any disadvantageous way, mainly because of using linear models (among other things), but they were an efficient way of modelling a modern composite material.

Bibliography

[1] T. Niezgoda and A. Derewońkoa. Multiscale composite FEM modeling. *Procedia Engineering*, 1(2009):209–212, 2009.

[2] Z.W. Xu, Y.H. Chen, W.J. Cantwell, and Z.W. Guan. Multiscale modelling of scaling effects in the impact response of plain woven composites. *Composites Part B: Engineering*, 188(107885), 2020.

[3] D. Ivančević and I. Smojver. Explicit multiscale modelling of impact damage on laminated composites. – Part I: Validation of the micromechanical model. *Composite Structures*, 145(1):248–258, 2016.

[4] D. Ivančević and I. Smojver. Explicit multiscale modelling of impact damage on laminated composites – Part II: Multiscale analyses. *Composite Structures*, 145(1):259–268, 2016.

[5] Tuomas Pärnänen. *Low-velocity impact damage in fibre metal laminates - a study of the impact resistance and metal-composite debonding*. PhD dissertation, Aalto University, 2016.

[6] Jarno Jokinen. *Numerical crack nucleation and propagation analyses of bonded joints*. PhD dissertation, Aalto University, 2019.

[7] R. Dsouza, J. Jokinen, P. Antunes E. Sarlin, and M. Kanerva. Future microbond testing - Finite element simulation of optical fibers for strains. Melbourne, Australia, December 2019. ICCM22. Twenty-second International Conference on Composite Materials.

[8] M. Kanerva, S. Korkiakoski, K. Lahtonen, J. Jokinen, E. Sarlin, S. Palola, A. Iyer, P. Laurikainen, X.W. Liud, M. Raappana, S. Tervakangas, and M. Valden. DLC-treated aramid-fibre composites: Tailoring nanoscale-coating for macroscale performance. *Composites Science and Technologys*, 171:62–69, 2019.

[9] R. Dsouza, P. Antunes, M. Kakkonen J. Jokinen, E. Sarlin, P. Kallio, and M. Kanerva. 3D interfacial debonding during microbond testing: Advantages of local strain recording. *Composites Science and Technologys*, 195(108163), 2020.

[10] Pekka Laurikainen, Sandra Pötz, Jarno Jokinen, Mathias von Essen, Mari Lindgren, Pasi Kallio, Mikko Kanerva, Gernot Oreski, and Essi Sarlin. High throughput mechanical micro-scale characterization of composites and the utilization of the results in finite element analysis. Athens, Greece, June

2018. ICCM22, Proceedings of the 18th European Conference on Composite Materials (ECCM).

[11] M. Kanerva, J. Jokinen, E. Sarlin, T. Pärnänen, M. Lindgren, M. Järventausta, and J. Vuorinen. Lower stiffness of gfrp after sulfuric acid-solution aging is due to degradation of fibre-matrix interfaces? *Composite Structures*, 212:524–534, 2019.

[12] F.C Campbell. *Structural Composite Materials*, page 1. A S M International, Materials Park, Ohio, first edition, 2010.

[13] Valery V. Vasiliev and Evgeny V. Morozov. *Advanced Mechanics of Composite Materials and Structural Elements*, pages 745–796. Elsevier, third edition, 2013.

[14] J. Bai. *Advanced Fibre-Reinforced Polymer (FRP) Composites for Structural Applications*. Woodhead Publishing, Helsinki, 2013.

[15] Meysam Toozandehjani, Nuruldiyanah Kamarudin, Zahra Dashtizadeh, E. Yee Lim, Ashen Gomes, and Chandima Gomes. Conventional and Advanced Composites in Aerospace Industry: Technologies Revisited. *American Journal of Aerospace Engineering*, 5(1):9–15, 2018.

[16] Saarela Olli, Airasmaa Ilkka, Kokko Juha, Skrifvars Mikael, and Komppa Veikko. *Komposiittirakenteet*. Muoviyhdistys ry., first edition, 2007.

[17] Jacob Aboudi, S.M. Arnold, and Brett A. Bednarcyk. *Micromechanics of composite materials: A generalized multiscale analysis approach*, pages 3–4,94–95. Elsevier, Amsterdam, first edition, 2013.

[18] F.C Campbell. *Manufacturing Processes for Advanced Composites*, pages 3–4,17–20. Elsevier, New York, first edition, 2004.

[19] Juho Posio. Interlaminar shear strength testing of non-unidirectionally reinforced composites. Master's thesis, Aalto University, Espoo, Finland, 4 2016. Aeronautical Engineering.

[20] M.H. Hassan, A.R. Othman, and S. Kamaruddin. A review on the manufacturing defects of complex-shaped laminate in aircraft composite structures. *Int J Adv Manuf Technol*, 91:4081–4094, 2017.

[21] Advani Suresh G. and Hsiao Kuang-Ting. *Manufacturing Techniques for Polymer Matrix Composites (PMCs)*, pages 245–253, 270–277. Woodhead Publishing, first edition, 2012.

[22] C.A. Howe, R.J. Paton, and A.A. Goodwin, editors. *A comparison between voids in RTM and Prepreg carbon/epoxy laminates*. Composites Processing and Microstructure, July 1997.

[23] D. Hull and T.W. Clyne. *An introduction to composite materials*, pages 36–37,65–66. Cambridge University Press, Great Britain, first edition, 1981.

[24] William Watt, Alan Howard Cottrell, and Anthony Kelly. Production and properties of high modulus carbon fibres. *Proceedings of Royal Society of London*, A(319):5–15, 1970.

[25] Rafic Younes, Ali Hallal, Farouk Fardoun, and Fadi Hajj Chehade. *Composites and Their Properties: Comparative Review Study on Elastic Properties Modeling for Unidirectional Composite Materials*, pages 391–408. InTech, first edition, 2012.

[26] Mark Hughes. Lecture notes on Long-fibre composites and laminates, CHEM-E2200: Polymer blends and composites, Aalto University, September 2019.

[27] Eugenio Giner, Vicente Franco, and Ana Vercher. Estimation of the reinforcement factor ξ for calculating E_2 with the Halpin-Tsai equations using the finete element method. Seville, Spain, June 2014. ECCM-16, Proceedings of the 16th European Conference on Composite Materials (ECCM).

[28] J.C. Halpin Affdl and J.L. Kardos. The halpin-tasi equations: A review. *Polymer Engineering & Science*, 16(5):344–352, 1976.

[29] Ovidio Colmenero. Simulation of electrical characteristics of ceramic matrix composites. Master's thesis, Deutsches Zentrum für Luft- und Raumfahrt e. V., Stuttgart, Germany, 7 2017. Bachelor Thesis in Aerospace Engineering.

[30] F.Kun. *Creep and Fatigue in Polymer Matrix Composites*, pages 327–349. Woodhead Publishing Series in Composites Science and Engineering, first edition, 2011.

[31] Masaru Zakoa, Yasutomo Uetsujib, and Tetsusei Kurashikia. Finite element analysis of damaged woven fabric composite materials. *Composites Science and Technology*, 63:507–516, 2003.

[32] S.Palola, E.Sarlin, S.Kolahgar Azari, V.Koutsos, and J.Vuorinen. Microwave induced hierarchical nanostructures on aramid fibers and their influence on adhesion properties in a rubber matrix. *Applied Surface Science*, 410:145–153, 2017.

[33] Georg Bechtold and Lin Yeb. Influence of fibre distribution on the transverse flow permeability in fibre bundles. *Composites Science and Technology*, 63:2069–2079, 2003.

[34] John Summerscales and Paul M. Russell. Observations on the fibre distribution and fibre strain in a woven fabric reinforcement. *Advanced Composite Letters*, 3(3):135–139, 2004.

[35] J.N Reddy. *Mechanics of Laminated Composite Plates and Shells – Theory and Analysis*, pages 83–84. CRC Press, second edition, 2004.

[36] Wim Van Paepegem and Joris Degrieck. Modelling strategies for fatigue damage behaviour of fibre-reinforced polymer composites. *European Journal of Mechanical and Enviromental Engineering*, 46(4):217–227, 2001.

[37] Verma Rahul, Shukla Alokita, Kandasamy Jayakrishna, V.R. Kar, M. Rajesh, S. Thirumalini, and M. Manikandan. *Structural Health Monitoring of Biocomposites, Fibre-Reinforced Composites and Hybrid Composites*, pages 33–52. Woodhead Publishing Series in Composites Science and Engineering, first edition, 2019.

[38] A. Jumahat, C. Soutis, F.R. Jones, and A. Hodzic. Fracture mechanisms and failure analysis of carbon fibre/toughened epoxy composites subjected to compressive loading. *Composite Structures*, 92(2):295–305, 2010.

[39] Lixin Wang, Yuhong Cui, Qinghua Qin, Hui Wang, and Jianshan Wang. Helical fiber pull-out in biological materials. *Acta Mechanica Solida Sinica*, 29(3):245–256, 2016.

[40] Yu Bai and Till Vallée and Thomas Keller. Delamination of pultruded glass fiber-reinforced polymer composites subjected to axial compression. *Composite Structures*, 91(1):66–73, 2009.

[41] A. Riccio. *Delamination Behaviour of Composites*, pages 28–64. Woodhead Publishing Series in Composites Science and Engineering, Chapter 2 - Delamination in the context of composite structural design, first edition, 2008.

[42] H. Mao and S. Mahadevan. Fatigue damage modelling of composite materials. *Composite Structures*, 85(4):405–410, 2002.

[43] M.R. Nurul Fazita, H.P.S. Abdul Khalil, A. Nor Amira Izzati, and Samsul Rizal. *Failure Analysis in Biocomposites, Fibre-Reinforced Composites and Hybrid Composites*, pages 51–78. Woodhead Publishing Series in Composites Science and Engineering, Chapter 3, first edition, 2019.

[44] S. Barré and T. Chotard and M.L. Benzeggah. Comparative study of strain rate effects on mechanical properties of flass fibre-reinforced thermoset matrix composites. *Composites Part A*, 27(12):1169–1181, 1996.

[45] Luiz Fernando Martins Leite and Bruno Martins Leite and Vitor Luiz Reis and Nubia Nale Alves da Silveira and Maurício Vicente Donadon. Strain rate effects on the intralaminar fracture toughness of composite laminates subjected to tensile load. *Composite Structures*, 201:455–467, 2018.

[46] S. Barré and T. Chotard and M.L. Benzeggah. Comparative study of strain rate effects on mechanical properties of flass fibre-reinforced thermoset matrix composites. *Composites Part A*, 27(12):1169–1181, 1996.

[47] Bruno Martins Leite and Luiz Fernando Martins Leite and Vitor Luiz Reis and Maurício Vicente Donadon and Nubia Nale Alves da Silveira. Strain rate effects on the intralaminar fracture toughness of composite laminates subjected to compressive load. *Composite Structures*, 186:94–105, 2018.

[48] John Scheirs. *Compositional and Failure Analysis of Polymers: A Practical Approach*, pages 471–472. John Wiley & Sons, Chapter 4, first edition, 2000.

[49] Konrad Dadej, Barbara Surowska, and Jarosław Bieniaś, editors. *Numerical/phenomenological model for fatigue life prediction of hybrid laminates*. AIP Publishing, September 2017.

[50] T.W. Clyne and D. Hull. *An introduction to composite materials*, pages 186–187. Cambridge University Press, Great Britain, third edition, 2019.

[51] LLorca, J. and González and C., Molina-Aldareguía, J.M. and Lópes, C.S. Multiscale Modeling of Composites: Toward Virtual Testing . . . and Beyond. *JOM*, 65:215–225, 2013.

[52] Varvara G. Kouznetsova. *Computational homogenization for the multi-scale analysis of multi-phase materials*. PhD dissertation, Technische Universiteit Eindhoven, 2002.

[53] W.J. Drugan and J.R. Willis. A micromechanics-based nonlocal constitutive equation and estimates of representative volumen element size for elastic composites. *J. Mech. Phy. Solids*, 44(4):497–524, 1996.

[54] R. Hill. Elastic properties of reinforced solids: some theoretical principles. *J. Mech. Phy. Solids*, 11:357–494, 1963.

[55] Paulo Cesar Plaisant Junior, Flávio Luiz de Silva Bussamra, and Francisco Kioshi Arakaki. Finite element procedure for stress amplification factor recovering in a representative volume of composite materials. *Journal of Aerospace Technology and Management*, 3(3):239–250, 2011.

[56] D. Trias, J. Costa, J.A. Mayugo, and J.E. Hurtado. Random models versus periodic models for fibre reinforced composites. *Computational Materials Science*, 38:316–324, 2006.

[57] A.R. Melro, P.P. Camanho, and S.T. Pinho. Generation of random distribution of fibres in long-fibre reinforced composites. *Composites Science and Technology*, 68:2092–2102, 2008.

[58] Wenzhi Wang, Yonghui Dai, Chao Zhang, Xiaosheng Gao, and Meiying Zhao. Micromechanical modeling of fiber-reinforced composites with statistically equivalent random fiber distribution. *Materials*, 9(8):624, 2016.

[59] Altair Engineering. *Altair Multiscale Designer 2019.2 User Manual*. Altair Engineering Inc.

[60] J.D. Eshelby. The determination of the field of an ellipsoidal inclusion and related problems. *Proc. R. Soc. Lond A*, 241:376–396, 1957.

[61] R. Hill. A self-consistent mechanics of composite materials. *J. Mech. Phys. Solids*, 13(4):213–222, 1965.

[62] Z. Hashin and S. Shtrikman. A variational approach to the theory of the elastic behaviour of multiphase materials. *J. Mech. Phys. Solids*, 11:127–140, 1963.

[63] Jacob Fish and Qing Yu and Kamlun Shek. Computational damage mechanics for composite materials based on mathematical homogenisation. *Int. J. Numer. Meth. Engrg.*, 45:1657–1679, 1999.

[64] P.M. Suquet. *Local and global aspects in the mathematical theory of plasticity. In Sawczuk, A. and Bianchi, G., editors, Plasticity today: modelling, methods and applications*, pages 1657–1679. Elsevier Applied Science Publishers, Chapter 4, first edition, 1985.

[65] R.J.M. Smit and W.A.M. Brekelmans and H.E.H. Meijer. Prediction of the mechanical behaviour of non-linear heterogeneous systems by multi-level finite element modeling. *Comput. Methods Appl. Mech. Engrg*, 155(1-2):181–192, 1998.

[66] David H. Allen and Roberto F. Soares. *Multiscale Modeling of the Evolution of Damage in Heterogeneous Viscoelastic Solids. In Y.W. Kwon, D.H. Allen and R.R. Talreja. Multiscale Modelling and Simulation of Composite Materials and Structures*, pages 495–527. Springer, Chapter 11, first edition, 2008.

[67] Essam Totry, Carlos González, and Javier LLorca. Prediction of the failure locus of C/PEEK composites under transverse compression and longitudinal shear through computational micromechanics. *Composites Science and Technology*, 68(4):3128–3136, 2008.

[68] Chenchen Liu and Celia Reina. Discrete averaging relations for micro to macro transition. *J. Appl. Mech.*, 83(8):081006–1–10, 2016.

[69] Nam-Ho Kim. Finite Element Analysis of Contact Problem, Chapter 5: EGM 6352 Advanced Finite Element Methods, Spring 2017.

[70] Gunter Warmbier. Optistruct contact - formulations, interface properties, utilities and output. Confidential User Slides, 2020.

[71] Zheng Yuan and Jacob Fish. Multiple scale eigendeformation-based reduced order homogenization. *Comput. Methods Appl. Mech. Engrg.*, 198:2016–2038, 2009.

[72] Altair Engineering. Multiscale designer v2019.2 - topic 2 - overview. Confidential User Slides, 2020.

[73] Zheng Yuan and Jacob Fish. Toward realization of computational homogenization in practice. *Int. J. Numerical Methods in Engineering*, 73:361–380, 2008.

[74] HEXCEL. *HexPly® 3501-6. Product Data Sheet*. Hexcel Corporation.

[75] HEXCEL. *HexTow® AS4. Product Data Sheet*. Hexcel Corporation.

[76] Karin Gipple. A Comparison of the Compression Response of Thick (6.35 mm) and Thin (1.60 mm) Dry and Moisture Saturated AS4/3501-6 Laminates. Technical report, David Taylor Research Center, 10 1990.

[77] V. Skyttä, O. Saarela, and M. Wallin. Progressive Failure of Composites Laminates; Analysis vs Experiments. Alexandroupolis, Greece, July 2006. ECF-16. 16th European Conference of Fracture.

[78] Qing Wang and Fu-Pen Chiang. Experimental characterization of interphase mechanical properties of composites. *Composites Part B*, 27:123–128, 1996.

A. Appendix

The different appendixes included in this section correspond to the multi-scale simulations performed during the author's learning process of both Multiscale Designer (MD) and OptiStruct (OS). The execution of these 'simple' study cases allowed to better understand how MD and OS work, as well as to acquire the modelling skills required for the real case indentation and impact simulations.

A.1 2D Plane Stress Model

A 2D-strip model was created to study the plane stress condition along the longitudinal cross-section of a composite specimen under tensile loading, in order to understand the in-plane load transfer. The model could be representative of a rectangular specimen or the central region in dog bone specimen.

The model was 2-dimensional, where x corresponds to the longitudinal direction (along which the tensile load is applied) and y was the coordinate in the thickness direction. The z component, which corresponds to the specimen width direction was 0. The plane stress condition implies that σ_z = 0. The strip dimensions were 100 mm long and 0.375 mm thick.

The laminate lay-up chosen for this model consisted of three plies throughout the thickness. Each ply was 0.125 mm thick. The lamination scheme was [0/90/0]. The material model was the same for each ply, although it presented different orientation according to the lamination scheme (when imagined in exact 3D).

In terms of modelling, the three plies were separately created and joined

Table 1.1. Material Constants used for the 2D Plane Stress Model.

Property	Ply 0	Ply 90	Homogenized Laminate
E_1 [GPa]	143.83	8.82	98.99
E_2 [GPa]	8.82	8.82	9.91
ν_{12} [-]	0.25	0.25	0.04
G_{12} [GPa]	4.45	2.66	3.64
G_{13} [GPa]	4.45	4.45	3.07
G_{23} [GPa]	2.66	4.45	4.45

with each other through TIE contact conditions in OptiStruct (OS). The idea was to model the laminate manually without using any 'laminate tool' included in Altair software and to check that the model behaves as a real composite.

The mesh consisted of shell elements distributed in parallel layers throughout the plies and laminate thickness. Each ply contained five layers of shell elements in the thickness direction. The specimen was fixed on the left hand-edge, restricting displacements in both x and z directions. On the right-hand edge, a load equivalent to a 1% strain was applied in the x direction. A linear static FE analysis was selected. Figure 1.1 shows a detailed view of the left-hand part of the model layout, as well as the mesh used.

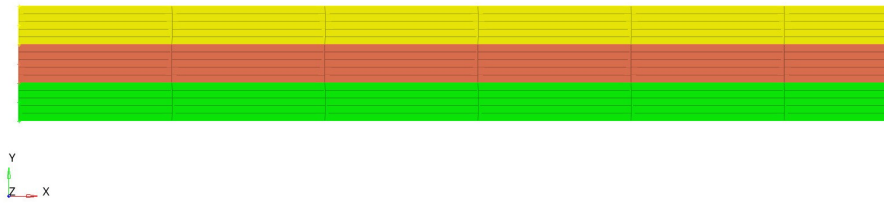

Figure 1.1. Detailed view of the left-hand part of the 2D-Strip Plane Stress Model layout.

Two simulations were performed with different material models. In the first case, a different material model was assigned to each ply depending on its orientation. From Table 1.1 the material constants for Ply 0 and Ply 90 were assigned to the model, following the lamination scheme [0/90/0]. In the second simulation, an homogenized material model generated in MD was used for the material definition of all the plies. The homogenized material constants used are stated in Table 1.1.

The results obtained in the stress field were compared to each other, see Table 1.2. For the stress in the x direction the difference between the

models is around 30%, whereas for the stress in the y direction is about 12%. In addition, the same problem was solved in Altair ESAComp™, which applies the Classical Lamination Plate Theory (CLPT) for the computations. The stress results provided by ESAComp™ (see Table 1.2) were similar to the ones obtained through the first simulation (plies definition) in the x direction and they differ in approximately the same magnitude with the results from the homogenized material model. In the y direction the ESAComp™ value is about 6% higher than the plies simulation, hence the difference to the homogenized model decreases around 6% too.

Table 1.2. Results from the 2D-strip model simulations in Optistruct and ESAComp™.

Magnitude	**Plies Sim.**	**Homogenized Mat. Sim.**	**ESAComp™**
$\sigma_{x_{max}}$ [MPa]	1439	990.1	1443.82
$\sigma_{y_{max}}$ [MPa]	88.29	99.11	94.12

A.2 3pt-Bending Model

The simulation of a three-point bending standard test was used to check the effect of the composite laminate definition on the OptiStruct results, as well as a first-approach to modelling an out-of-plane load case. For this, two models with the same geometry, material model, mesh type and boundary conditions were compared. The difference between the models lies in the way the quasi-isotropic laminate was defined. In addition the three-point bending test served as first out-of-plane modelling case, being the 'bridge' between the 2D plane stress model and the 3D indentation model.

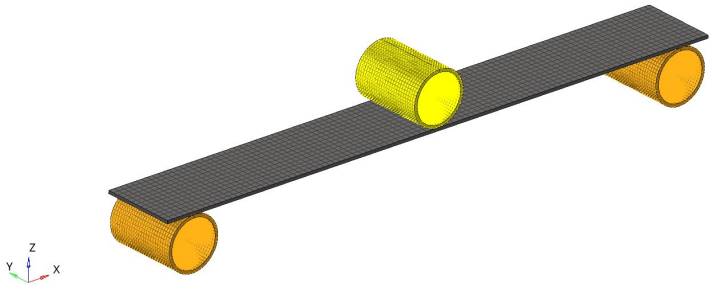

Figure 1.2. 3D model geometry of the Three-point Bending test simulated in OptiStruct.

In the first model, the laminate was defined as a 8-ply quasi-isotropic laminate with solid linear elements (CHEXA - hex8). In this case, there was not separation between plies since all the plies belong to the same

mesh. In the second model, the laminate was defined by using 8 separated plies of solid linear elements (CHEXA - hex 8) and, using TIE contact conditions between the plies in order to connect them. Each ply was meshed independently. The mesh size in both models is 2.

The laminate specimen dimensions were 200 x 25 x 1 mm and the distance between supports was 180 mm. The supports were cylinders of 18 mm diameter and they are 10 mm away from the edges of the specimen. Both supports were set as fixed restricting their movement in all 6-DoF. The 3D model geometry used in the simulation is shown in Fig.1.2. The load was a deformation and it was applied as a -3 mm displacement by the upper cylinder in the center of the specimen. A linear static analysis was run.

The material model used in the specimen for both simulations was an homogenized material model created in Multiscale Designer based on a CFRP with an isotropic standard modulus epoxy matrix and transisotropic high-modulus carbon fibres. The homogenized material model constants are given in Table 1.3. The solid rigid condition was set to both the supports and the upper cylinder in order to make them act as rigid bodies in contact with the CFRP specimen.

Table 1.3. CFRP homogenized material model generated in Multiscale Designer and used in the Three-point Bending simulations.

Property	**Value**
E_1 [GPa]	52.49
E_2 [GPa]	52.49
E_3 [GPa]	11.73
ν_{12} [-]	0.31
ν_{13} [-]	0.26
ν_{23} [-]	0.06
G_{12} [GPa]	19.98
G_{13} [GPa]	3.87
G_{23} [GPa]	3.87

The simulation was proven to work properly since both the displacement and stress fields were consistent with the expected behaviour of a 3-point bending test undergoing a 3 mm deformation, see Fig.1.3 (left). The results obtained for both models are similar, which confirm that the same behaviour is obtained regardless of the definition of the laminate (with or without separation of plies). The difference in the Von Mises stress field

results was insignificant as seen in the comparison from Fig.1.3 (right). In addition, the stress field through the laminate thickness is properly captured as shown in Fig. 1.4. As expected in any plate under bending, the stress distribution through the thickness was symmetric with respect to the neutral axis, having the maximun stresses on the outer plies and the stress being zero in the neutral axis. The upper plies undergo compressive stress, whereas the lower plies are subjected to tensile stress.

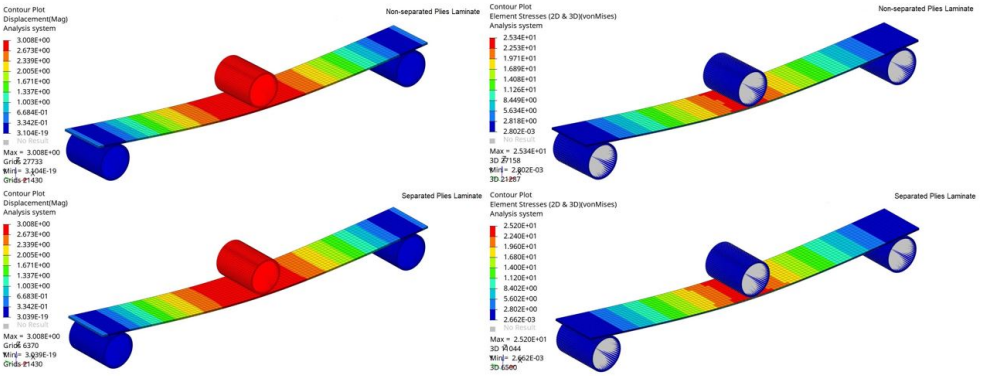

Figure 1.3. Displacements field (left) and Von Mises stress field (right) comparison between the two models.

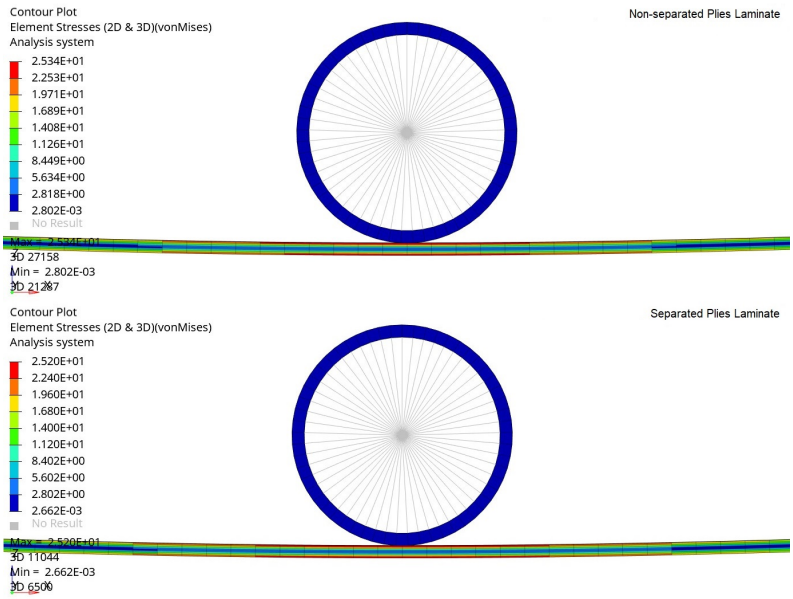

Figure 1.4. Stress field comparison through the laminate thickness between the two models.

The knowledge and conclusions learnt from this three-point bending model, will be used in the indentation and impact models reported in the main body of the thesis. For example, the 3D solid elements laminate will be defined without using any TIE contact conditions between the plies in the indentation and impact models, as it has been proven that defininig the plies with a continuous mesh is enough and simplier.